



저작자표시-비영리-변경금지 2.0 대한민국

이용자는 아래의 조건을 따르는 경우에 한하여 자유롭게

- 이 저작물을 복제, 배포, 전송, 전시, 공연 및 방송할 수 있습니다.

다음과 같은 조건을 따라야 합니다:



저작자표시. 귀하는 원저작자를 표시하여야 합니다.



비영리. 귀하는 이 저작물을 영리 목적으로 이용할 수 없습니다.



변경금지. 귀하는 이 저작물을 개작, 변형 또는 가공할 수 없습니다.

- 귀하는, 이 저작물의 재이용이나 배포의 경우, 이 저작물에 적용된 이용허락조건을 명확하게 나타내어야 합니다.
- 저작권자로부터 별도의 허가를 받으면 이러한 조건들은 적용되지 않습니다.

저작권법에 따른 이용자의 권리는 위의 내용에 의하여 영향을 받지 않습니다.

이것은 [이용허락규약\(Legal Code\)](#)을 이해하기 쉽게 요약한 것입니다.

[Disclaimer](#)

공학박사학위논문

레이저 유도 플라즈마 및 초음파
기술을 활용한 열유체 진단기법 연구

Thermo-Fluid Diagnostic Methods using Laser-
Induced Plasma and Ultrasound Wave

2015년 8월

서울대학교 대학원

기계항공공학부

이 석 환

Abstract

Thermo-Fluid Diagnostic Methods using Laser-Induced Plasma and Ultrasound Wave

Seok Hwan Lee

Mechanical and Aerospace Engineering

The Graduate School

Seoul National University

We investigated the LIBS (laser-induced breakdown spectroscopy) characteristics in various phase conditions including single-phase (gas) and two-phase (liquid gas, solid gas) for thermo-fluid applications. For single-phase (gas) analysis, two-dimensional mapping of the LIBS signals from chemical species information was performed in propane flames with in situ diagnostics. Key combustion information, such as density, fuel concentration, and fuel/air equivalence ratio were provided by the LIBS measurement. For the two-phase spray flame, the simultaneous laser ignition and spectroscopy enabled rapidly determining the local equivalence ratio and condensed fuel concentration during the reaction. In parallel with the laser ignition, the equivalence ratio and droplet characteristics, such as concentration, size, and distribution of spray combustion, were simultaneously obtained for a feedback control system. For the two-phase aerosol analysis, LIBS detected solid

carbon particulates in a flow system that was designed to replicate aircraft exhaust flow conditions. The detected signals from the emissions stream at velocities of up to 70 m/s showed that in-situ characterization of carbon particulates in the high-speed exhaust were proven feasible. The results obtained through this research will allow for more practical diagnostics in various applications such as biology, combustion and the environment.

In addition, basic research was conducted for the thermo-fluid diagnostics using LIUS (laser-induced ultrasound) waves. We demonstrated that the reduced-graphene-oxide-coated thin aluminum film (rGO-Al) and rGO-coated polydimethylsiloxane (rGO-PDMS) were effective optoacoustic transmitters for generating high-pressure and high-frequency ultrasound waves. Under pulsed laser excitation, rGO-Al and rGO-PDMS transmitters generated enhanced optoacoustic pressure that was 64 and 76 times stronger, respectively, than Al alone. Promising optoacoustic wave generation was made possible by optimizing the thermoelasticity of metal, the PDMS film and the thermal conductivity of rGO in the proposed transmitter for laser-induced ultrasound applications. LIBS and LIUS have great advantages as analytical techniques, namely, real-time rapid analysis and stand-off detection capability, which are all material phases for diagnosing thermo-fluid phenomena.

***Keywords:* Laser-Induced Breakdown Spectroscopy(LIBS), Plasma, thermo-fluid, combustion, Laser-Induced UltraSound(LIUS), Graphene**

Student Number: 2010-30195

LIST

ABSTRACT.....	i
LIST.....	iii
LIST OF FIGURES.....	vii
LIST OF TABLES.....	xvi
PREFACE.....	xvii

CHAPTER 1

INTRODUCTION.....	1
1.1 Motivation and purpose.....	1
1.2 Laser-material interaction.....	5
1.2.1 Laser.....	5
1.2.2 Various phenomena in laser-matter interactions.....	6
1.3 Laser-Induced Breakdown Spectroscopy (LIBS) for Thermo-Fluid Diagnostics.....	10
1.3.1 Introduction of LIBS.....	10
1.3.2 The theory of LIBS.....	11
1.3.3 Comparison of LIBS and conventional diagnostic methods for thermo-fluid applications.....	17
1.3.4 LIBS for thermo-fluid applications.....	23
1.4 Laser-Induced Ultrasound Wave for Thermo-Fluid Diagnostics.....	27

1.4.1 Introduction of LIUS.....	27
1.4.2 The theory of LIUS.....	30
CHAPTER 2	
EXPERIMENTAL SETUP.....	34
2.1 Experimental apparatus.....	34
2.1.1 Laser.....	34
2.1.2 Spectroscopy.....	35
2.1.3 Hydrophone.....	36
2.2 Shadow graph.....	37
2.3 Light scattering.....	38
CHAPTER 3	
DIAGNOSTIC OF GAS PHASE REACTING FLOW USING LIBS.....	39
3.1 Background and objective.....	39
3.2 Experimental condition.....	41
3.3 Results.....	45
3.4 Conclusion.....	52
CHAPTER 4	
DIAGNOSTIC OF TWO PHASE (LIQUID-GAS) REACTING FLOW USING LIBS.....	54

4.1 Background and objective.....	54
4.2 Experimental condition.....	60
4.3 Results.....	62
4.4 Conclusion.....	94

CHAPTER 5

DIAGNOSTIC OF TWO PHASE (SOLID-GAS) FLOW USING LIBS.....	96
5.1 Background and objective.....	96
5.2 Experimental condition.....	99
5.3 Data analysis.....	105
5.4 Results.....	107
5.4.1 LIBS spectra in particle stream	107
5.4.2 Visualization of particle and plasma.....	110
5.4.3 LIBS signal for delay time.....	113
5.4.4 LIBS signal for carbon concentration.....	117
5.4.5 Limit Of Detection (LOD).....	125
5.5 Conclusion.....	126

CHAPTER 6

DIAGNOSTIC OF LIQUID PHASE SAMPLE USING LIUS : PART 1 REDUCED GRAPHENE OXIDE COATED THIN ALUMINUM FILM ...	128
---	-----

6.1 Background and objective.....	128
6.2 Experimental condition.....	130
6.3 Results.....	132
6.4 Conclusion.....	140

CHAPTER 7

DIAGNOSTIC OF LIQUID PHASE SAMPLE USING LIUS : PART 2 REDUCED GRAPHENE OXIDE COATED POLYDIMETHYLSILOXANE (PDMS) FILM.....	141
7.1 Background and objective.....	141
7.2 Experimental condition.....	143
7.3 Results.....	145
7.4 Conclusion.....	154

CHAPTER 8

CONCLUSION.....	156
REFERENCES.....	158
ABSTRACT IN KOREAN.....	167
ACKNOWLEDGEMENTS IN KOREAN.....	169

LIST OF FIGURES

Fig. 1.1 Applications of lasers in materials processing. PLA/PLD: pulsed-laser ablation/deposition. LA: laser annealing. LC: laser cleaning. LIS: laser-induced isotope separation. MPA/MPI: multi-photon absorption/ionization. LSDW/LSCW: laser-supported detonation/combustion waves. LCVD: laser-induced CVD. LEC: laser-induced electrochemical plating/etching	7
Fig. 1.2 Phenomenology of laser-aerosol (Al_2O_3) with steady-state regimes as a function of intensity and particle radius	8
Fig. 1.3 LIBS emission spectra normalized by nitrogen line peak intensity with various reactant flow velocities in a methane premixed flame.....	11
Fig. 1.4 Image of plasma in air.....	12
Fig. 1.5 The transitions of electrons between energy levels in an atom.....	13
Fig. 1.6 (a) Image of a premixed propane flame and plasma and (b) LIBS spectra from plasma for different plasma positions	16
Fig. 1.7 H/N intensity ratios versus H/N in combustion products from methane and ethylene premixed flames	24
Fig. 1.8 (a) Schematic of a LIBS system used for a power generation boiler; (b) spectrum of metallic particles from the exhaust stream.....	25
Fig. 1.9 Typical configuration of optical generation of ultrasound using thermoelastic expansion	28
Fig. 1.10 Typical scheme for passive optical detection	28

Fig. 1.11 1-dimensional analysis of optoacoustic wave generation: (a) the time constant of heat propagation in the Al layer; (b) the time related to the acoustic wave propagation and attenuation by the laser pulse for Al film	33
Fig. 2.1 Surelite Nd:YAG laser.....	34
Fig. 2.2 Minilite Nd:YAG laser.....	35
Fig. 2.3 Mechelle spectroscopy	36
Fig. 2.4 Hydrophone: (a) membrane type; (HMB-0500) (b) needle type (HNR-1000).....	36
Fig. 2.5 Shadow graph setup.....	37
Fig. 2.6 Light scattering setup.....	38
Fig. 3.1 Experimental setup	43
Fig. 3.2 (a) Flame image of LPG 50 ccm, (b) spectrum of LPG flame at 2 mm above the burner from 200 mJ laser energy at 2 μ s delay time. Three peaks of CN (388.3 nm), C ₂ (516.6 nm) and H (656.2 nm) are identified	44
Fig. 3.3 LIBS signal according to delay time for different laser energy (a) H atomic peak (656 nm) and (b) CN molecular band (388 nm)	47
Fig. 3.4 Density mapping of LPG flame using LIBS base signal (a) measurement positions, (b) LIBS base signal mapping of LPG 50 ccm flame, (c) LIBS base signal mapping of LPG 50 ccm-EOH 10 ccm, (d) LIBS base signal mapping of LPG 50 ccm-AIR 10 ccm	48
Fig. 3.5 CN LIBS signal mapping for (a) LPG 50 ccm (b) LPG 50 ccm-EOH 10 ccm mixture (c) LPG 50 ccm-AIR 10 ccm mixture flame with 200 mJ laser	

energy and 2 μ s delay time.....	49
Fig. 3.6 H/O LIBS signal ratio mapping for (a) LPG 50 ccm (b) LPG 50 ccm- EOH 10 ccm mixture (c) LPG 50 ccm-AIR 10 ccm mixture flame with 200 mJ laser energy and 2 μ s delay time.....	51
Fig. 4.1 (a) Experimental setup, (b) scattering image of the droplet.....	62
Fig. 4.2 Threshold energy for breakdown in the spray according to droplet size in the droplet stream	63
Fig. 4.3 Plasma images at four different times (250 ns, 500 ns, 750 ns and 1000 ns) in air and gasoline droplet stream.....	66
Fig. 4.4 (a) Radial and vertical displacement of plasma (b) radial and vertical velocity of plasma in air and gasoline droplet stream.....	67
Fig. 4.5 Sequences of the temporal development of laser-induced air breakdown (left column) and gasoline spray ignitions (right columns)	70
Fig. 4.6 The mean intensity of high speed images for air breakdown and spray ignition	71
Fig. 4.7 Ensemble of the LIBS spectra according to the delay time in (a) air, (b) spray at early time ($\sim 1 \mu$ s) and (c) spray after 1 μ s.....	71
Fig. 4.8 The maximum intensities of the atomic signals (H and O) until 1 μ s delay time and the molecular signals (CN and C ₂) until 10 μ s in the spray ...	73
Fig. 4.9 Schematics of LIBS measurement in fuel droplets.....	76
Fig. 4.10 (a) C ₂ spectra, (b) H, O spectra at 10 mm height in spray for different base intensity schematics of LIBS measurement in fuel droplets ...	77

Fig. 4.11 Probability density function of (a) the base intensity, (b) C ₂ intensity, (c) H intensity and (d) O intensity.....	78
Fig. 4.12 (a) Probability density function of the droplet diameter for different height (a) 10 mm, (c) 15 mm and (e) 20 mm, probability density function of the C ₂ /base intensity ratio for different heights (b) 10 mm, (d) 15 mm and (f) 20 mm.....	82
Fig. 4.13 Shot-to-shot fluctuation of (a) H and O intensities and (b) H/O intensity ratio, (c) C ₂ intensity and (d) C ₂ /base intensity ratio.....	86
Fig. 4.14 Calibration curves (a) H/O ratio according to the equivalence ratio and (b) C ₂ /base intensity ratio according to the fuel droplet diameter (c) C ₂ /base intensity ratio according to the fuel droplet number density and (d) C ₂ /base intensity ratio according to the cube root of liquid fuel volume fraction.....	88
Fig. 4.15 (a) Equivalence ratios and (b) liquid fuel volume fraction along the radial direction for different heights (10 mm, 15 mm and 30 mm).....	93
Fig. 5.1 (a) Experimental setup, (b) visualization setup	101
Fig. 5.2 Spectrum of (a) air and (b) glucose particle of 787.11 μg/m ³ concentration. Spectrum of air has O I and N I peaks. Spectrum of glucose particle has C I, CN, H I, O I and N I peaks	108
Fig. 5.3 SEM (Scanning Electric Microscopy) image of glucose particle at (a) 2 m/s and 409.29 μg/m ³ , (b) 70 m/s and 62.01 μg/m ³	109
Fig. 5.4 Visualization images of plasma and particles for different	

concentration and velocity in low (a), (b), (c) and high (d) (e) (f) velocity flow conditions. Low velocity regime : (a) $62.01 \mu\text{g}/\text{m}^3$, 9.9 m/s, (b) $87.7 \mu\text{g}/\text{m}^3$, 7.0 m/s, (c) $409.29 \mu\text{g}/\text{m}^3$, 1.5 m/s and high velocity regime : (d) $62.01 \mu\text{g}/\text{m}^3$, 70 m/s, (e) $87.7 \mu\text{g}/\text{m}^3$, 47.8 m/s, (d) $409.29 \mu\text{g}/\text{m}^3$, 2 m/s.112

Fig. 5.5 Visualization images of plasma, particle and CN band signal from single LIBS detection for different concentrations obtained simultaneously. (a) $409.29 \mu\text{g}/\text{m}^3$, (b) $204.64 \mu\text{g}/\text{m}^3$, (c) $64.62 \mu\text{g}/\text{m}^3$, (d) $62.01 \mu\text{g}/\text{m}^3$ and (e) CN band signal from single LIBS detection for different concentrations113

Fig. 5.6 Glucose signals (CN, H, O and N) averaged 100 shots according to the delay time (a) Intensity of glucose signals (CN, H, O and N) according to delay time, (b) Magnification of lower intensity region of Fig. 5.6 (a), (c) Intensity of base line according to delay time, (d) Peak to base ratio of the glucose signal according to delay time.....115

Fig. 5.7 C and CN peaks averaged 100 shots according to the delay time with 200 mJ laser energy and $1 \mu\text{s}$ ICCD exposure time116

Fig. 5.8 Peak to base (P/B) ratio according to the glucose concentration, (a) Peak to base (P/B) ratio of O and N according to the glucose concentration, (b) Peak to base (P/B) ratio of C, CN and H according to the glucose concentration118

Fig. 5.9 Carbon and CN band peaks averaged 100 shots with varying low stream velocity (a) Carbon peak averaged 100 shots at 247.86 nm with varying low stream velocity, (b) CN band peak averaged 100 shots at 388.3

nm with varying low stream velocity.....	119
Fig. 5.10 Carbon and CN band peaks averaged 100 shots with varying high stream velocity (a) Carbon peak averaged 100 shots at 247.86 nm with varying high stream velocity, (b) CN band peak averaged 100 shots at 388.3 nm with varying high stream velocity.....	121
Fig. 5.11 Calibration curve showing response of 247.8 nm C emission to changing concentration of glucose aerosols for both high and low velocity.....	123
Fig. 5.12 Calibration curve showing linear response of 388.3 nm CN band emission to changing concentration of glucose aerosols for both high and low velocity.....	123
Fig. 5.13 Statistical calibration curve using $p(=FI)$ showing response of 247.8 nm C emission to changing concentration of glucose aerosols for both high and low velocity cases	124
Fig. 5.14 Statistical calibration curve using $p(=FI)$ showing response of 388.3 nm CN emission to changing concentration of glucose aerosols for both high and low velocity cases	124
Fig. 6.1 Sketch of the side view of rGO (20, 100, 200 nm) coated aluminum film (100 nm) on a glass substrate (500 μm).....	130
Fig. 6.2 Experimental setup.....	132
Fig. 6.3 Optoacoustic signals from each transmitter (Al-only, 20 nm rGO coated Al, 100 nm rGO coated Al, and 200 nm rGO coated Al) at 56 mJ/cm^2	

positioned 2.85 mm from the hydrophone	133
Fig. 6.4 Maximum pressure of optoacoustic wave from 100 nm rGO coated Al according to the distance between the transmitter and detector for varying laser fluencies.....	134
Fig. 6.5 Maximum pressure of optoacoustic wave from 20 nm, 100 nm, 200 nm rGO coated Al and Al only for varying fluences as measured 2.85 mm from the sample.....	135
Fig. 6.6 Visualization images of propagating optoacoustic (left running) wave from 4 different transmitters (Al-only, 20 nm rGO coated Al, 100 nm rGO coated Al, 100 nm rGO only) positioned on the right for 3 laser fluences (17.5 mJ/cm ² , 30.56 mJ/cm ² and 43.28 mJ/cm ²) taken at 4 μs after the laser shot directed from the left.....	138
Fig. 6.7 Frequency spectra for the optoacoustic waves from 20 nm, 100 nm rGO coated Al and Al only) for 56 mJ/cm ² measured at 2.85 mm away from the sample.....	139
Fig. 7.1 Sketch of the side view of rGO coated PDMS film on a glass substrate (500 μm).....	144
Fig. 7.2 Experimental setup.....	144
Fig. 7.3 Optoacoustic signals from each transmitter (Al-only, Cr-only, 100 nm rGO coated Al, PDMS only and 100 nm rGO coated PDMS) at 35.66 mJ/cm ² positioned 3 mm from the hydrophone.....	146
Fig. 7.4 1-dimensional analysis of optoacoustic wave generation (a) the time	

constant of heat propagation in the laser irradiated layers (b) the time related the acoustic wave propagation and attenuation by the laser pulse for different films (Al-only, PDMS only, rGO, and 100 nm rGO coated PDMS) at 35.66 mJ/cm².....149

Fig. 7.5 Maximum pressure of optoacoustic wave from Al only, Cr only, 100 nm rGO coated Al, PDMS only, 100 nm rGO coated PDMS for varying fluences as measured 3 mm from the sample150

Fig. 7.6 Visualization images of propagating optoacoustic (left running) wave from 3 different transmitters (Al only, PDMS only and 100 nm rGO coated PDMS) positioned for 3 laser fluences (25.37 mJ/cm² , 30.57 mJ/cm² and 35.66 mJ/cm²) taken at 3 μs after the laser shot directed from the left.....153

Fig. 7.7 Frequency spectra for the optoacoustic waves from Al only, 100 nm rGO coated Al, PDMS only and 100 nm rGO coated PDMS for 35.66 mJ/cm² measured at 3 mm away from the sample.....154

LIST OF TABLES

Table 1.1 Potential combustion diagnostic techniques.....	3
Table 1.2 Comparison of thermo-fluid diagnostic techniques including LIBS.....	20
Table 1.3 Comparison of droplet diagnostic techniques including LIBS.....	21
Table 1.4 Comparison of solid particle diagnostic techniques including LIBS.....	22
Table 5.1 Flow velocities for corresponding carbon concentrations.....	104
Table 5.2 Hitting rate of carbon particulates for different concentrations....	105
Table 5.3 Particle size for different velocity and concentration.....	110
Table 5.4 Limit of detection for different velocity and spectrum line (C 247.86 nm, CN 388.3 nm).....	126
Table 6.1 Coefficient of thermal expansion for different materials	137
Table 7.1 Coefficient of thermal expansion, thermal conductivity, absorptance, and thickness of film for different materials	147

Preface

This thesis is based on the following publications and manuscripts.

Chapter 3

S.H. Lee, T.H. Hahn, J.J. Yoh, "Towards a two-dimensional laser induced breakdown spectroscopy mapping of liquefied petroleum gas and electrolytic oxy-hydrogen flames," *Spectrochimica Acta B*, Vol. 88, pp 63-68, 2013

Chapter 4

S.H. Lee, H. Do, J.J. Yoh, "Optical ignition and breakdown for spectroscopy for spray flame aimed at fuel-air ratio and droplet characteristics feedback control," *Combustion and Flame*, in preparation

Chapter 5

S.H. Lee, J.J. Yoh, "Detection of carbon particulates from a high-speed stream reaching 70 meters/second," *Applied Spectroscopy*, Vol. 66, Issue 1, pp. 107-113, 2012

S.H. Lee, J.J. Yoh, "Spectroscopic detection of carbon particulates from a high speed jet stream with extended plasma visualization," *Spectrochimica Acta Part B*, Vol. 74, pp 144-150, 2012

Chapter 6

S.H. Lee, M. Park, J.J. Yoh, H. Song, E.Y. Jang, Y.H. Kim, S. Kang, Y. S. Yoon, "Reduced graphene oxide coated thin aluminum film as an optoacoustic transmitter for high pressure and high frequency ultrasound generation," *Applied Physics Letter*, Vol. 101, 241909, 2012

M. Park, S.H. Lee, J.J. Yoh, "Characterization of laser-induced ultrasound signal by reduced graphene oxide thickness and laser intensity," *Applied Physics B*, Vol. 113, pp 389-393, 2012

Chapter 7

S.H. Lee, Y. Lee, J. J. Yoh, "Reduced graphene oxide coated PDMS film as an optoacoustic transmitter for high pressure and high frequency ultrasound generation," *Applied Physics Letter*, Vol. 106, 081911, 2015

The chapters are reproduced with permission of the co-authors and the publishers.

CHAPTER 1

INTRODUCTION

1.1 Motivation and purpose

Laser-based techniques for thermo-fluid research have many advantages such as remote, nonintrusive, in situ, spatially and temporally precise measurements of important chemical parameters. Laser techniques offer a number of advantages over the physical probing methods that have traditionally been employed to investigate and characterize thermo-fluid phenomena[1]. As such, various laser diagnostic techniques such as Particle Image Velocimetry(PIV), Laser-Induced Fluorescence(LIF), and Coherent Anti-stokes Raman Spectroscopy(CARS), spontaneous Raman scattering have been developed for obtaining velocity, temperature, concentration of chemical species, and density. In practice, however, spontaneous Raman scattering signals are very weak and are thus susceptible to fluorescence/emission interference. Furthermore, the complexity of a pulsed Raman scattering measurement may limit its application to laboratory environments as opposed to test environments.

In this work, component analysis by laser-induced breakdown spectroscopy (LIBS) and laser-induced ultrasound (LIUS) waves are utilized as promising

means of advancing thermo-fluid diagnostics. The purpose of this study is to understand the fundamental characteristics of the laser-induced plasma and the laser-induced ultrasound waves and to detect multiple species and large molecules in various phases, including two-phase diagnostics of thermo-fluid phenomena using LIBS and LIUS.

Table 1.1 lists potential combustion diagnostic techniques that are suitable for in situ point measurements. The temperatures and concentrations of chemical species can be obtained using Rayleigh scattering, and we can obtain not only the particle sizes and distributions but also the low velocity fields (from the PIV measurements) through Mie scattering. In addition, inelastic scattering such as LIF and Raman scattering are used to measure the concentrations of chemical species such as OH, CH, and O₂ as well as temperature. However, laser-based techniques are not without their disadvantages. A major limitation is the requirement for optical access to the test volume, and no signal laser technique is capable of measuring all species and temperatures simultaneously. Various approaches may have to be combined to characterize the medium to the extent desired, and the laser spectroscopic techniques tend to be most applicable to small molecules. For large molecules, spectroscopy is often very complicated depending on symmetry class, and the spectral signatures may be sufficiently similar, for example with polycyclic aromatic hydrocarbons (PAHs), for which individual constituent identification is very difficult.

Table 1.1 Potential combustion diagnostic techniques [1]

Elastic scattering processes	Inelastic scattering processes	Absorption processes	Nonlinear optical processes
Rayleigh	Spontaneous Raman scattering	Resonant line of sight	Stimulated Raman gain/loss spectroscopy
Mie	Near-resonant Raman scattering Laser-induced fluorescence (LIF)	Differential absorption	Raman-induced Kerr effect Stimulated Raman scattering Hyper-Raman scattering Coherent anti-Stokes Raman scattering (CARS) Degenerate four-wave mixing Polarization spectroscopy higher-order Raman Higher-order Raman spectral excitation spectroscopy

In contrast, the advent of high-intensity laser sources has opened up new possibilities in diagnosing solid surfaces, solid particles, liquids and gases. The idea is that by vaporizing and exciting an absorbing material (in gaseous, liquid or solid form) with a laser pulse of appropriate intensity, one can use the resulting spectral emission to infer composition, relative and absolute concentrations of atomic and even molecular forms present in the specimen. Hence, the notion of laser-induced breakdown spectroscopy is given by this technique. LIBS is a nonintrusive, sensitive optical diagnostic technique for measuring the concentration of various atomic and molecular species in test media. LIBS has high potential for diagnosing thermo-fluid phenomena that overcomes the limitations of existing methods.

Additionally, ultrasound imaging plays a critical role in medical diagnosis. It relies on detecting mechanical properties within biological tissues, and it has been irreplaceable because of its real-time imaging capabilities. There are major types of ultrasound transducers, based on the methods used to generate and detect acoustic waves. The first is piezoelectric technology, the dominant technology since the birth of medical ultrasonics. The second is called capacitive micro-machined ultrasound transducers (CMUTs), a rapidly surging technique. The third transduction mechanism is optoacoustics which is an attractive option that potentially overcomes the major limitations of piezoelectric and CMUTs. The use of optoacoustic ultrasound imaging has high potential for diagnosing thermo-fluid phenomena because no optical

window is necessary; the process is entirely based on phase detection. Optoacoustic transducers can overcome the limitations of existing laser-based diagnostic tools for thermo-fluid phenomena.

Thus, it is necessary study more about laser-induced plasma and ultrasound waves for thermo-fluid diagnostics. These two techniques have practical advantages owing to their simple setup, all-phase detection, easy optical access, etc . The developed method that use LIBS and LIUS can be useful not only in cold gas applications but also in reacting systems such as propulsion and automotive engines.

1.2 Laser-material interaction

1.2.1 Laser

A laser (light amplification by stimulated emission of radiation) is a device that emits light that has the characteristics of directivity, monochromatism, and coherence. A laser beam propagates in a straight line, whereas ordinary light sources emit in all directions. Directivity qualitatively describes the property of laser radiation to remain concentrated at long distances. Lasers emit all photons with the same energy and thus, the same wavelength; they are said to be monochromatic. The light from a laser typically comes from one atomic transition with a single precise wavelength. Therefore, laser light has a single spectral color and is nearly the purest monochromatic light available. Additionally, lasers differ from other sources

of light because they emit light coherently. Spatial coherence allows for lasers to be focused to tight spots, enabling applications such as laser cutting and lithography. Spatial coherence also allows laser beams to stay narrow over long distances (collimation). Lasers can also have high temporal coherence, which allows them to have very narrow spectra.

1.2.2 Various phenomena in laser-matter interactions

Laser-material interactions involve complex processes of radiation, heating, melting, vaporization, ejection of atoms, ions and molecules, shock waves, plasma initiation and plasma expansion. They depend on a number of variables such as pulse duration, irradiance, and so forth. Figure 1.1 shows an overview of the various applications and parameter regimes employed in laser processing. The laser intensities and interaction times shown in Fig. 1.1 refer to different types of lasers. With long interaction times, most of the energy in laser irradiation is transferred into heat by the absorption of the photons by samples while the generated electrons have low ionization potential. At the same time, short interaction times cause laser ablation because of the high irradiance ($> 10^9 \text{ W/cm}^2$) of laser energy. At this high irradiance, the temperature of the sample surface rises substantially above the vaporization temperature. Once plasma is generated by high laser irradiance, plasma expands as a plume, which drives a shock wave towards the incoming laser beam.

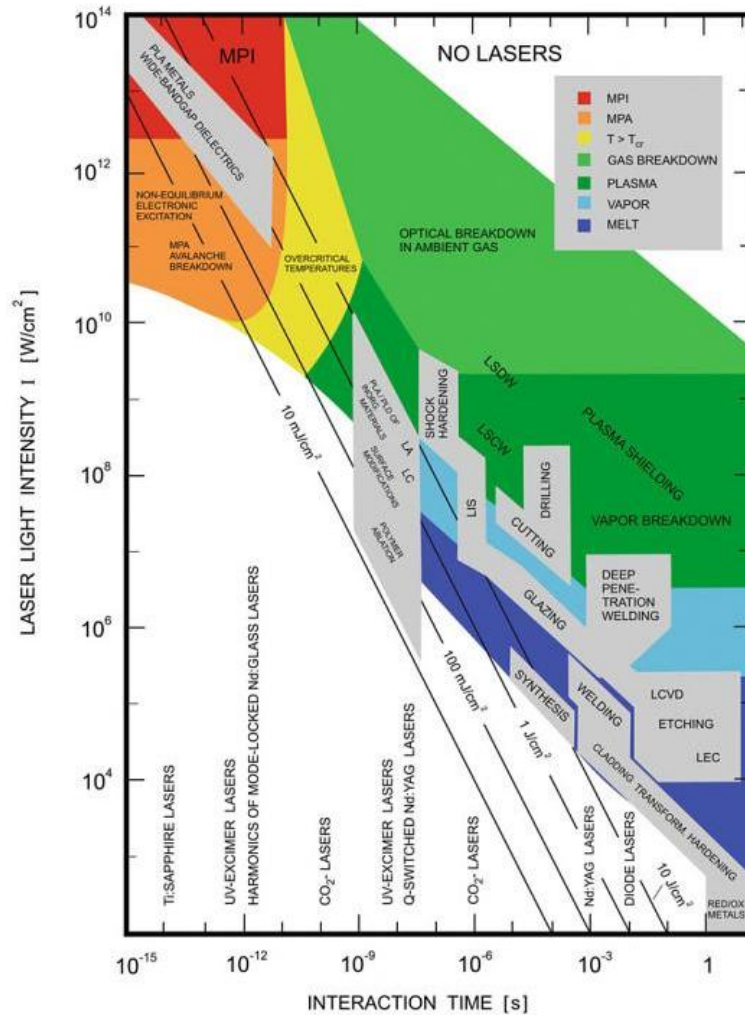


Fig. 1.1 Applications of lasers in materials processing. PLA/PLD: pulsed-laser ablation/deposition. LA: laser annealing. LC: laser cleaning. LIS: laser-induced isotope separation. MPA/MPI: multi-photon absorption/ionization. LSDW/LSCW: laser-supported detonation/combustion waves. LCVD: laser-induced CVD. LEC: laser-induced electrochemical plating/etching [2]

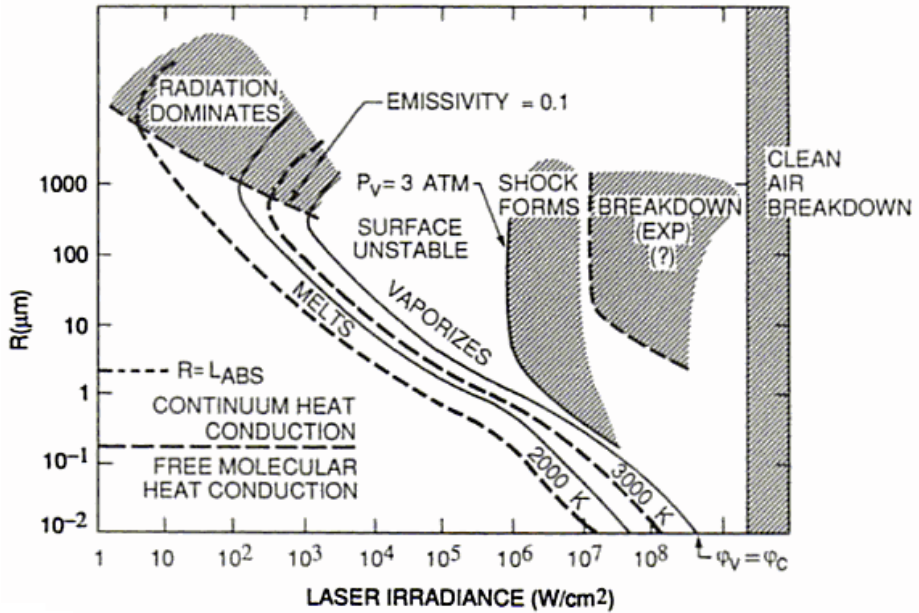


Fig. 1.2 Phenomenology of laser-aerosol (Al_2O_3) with steady-state regimes as a function of intensity and particle radius [3]

Figure 1.2 shows the phenomenology of laser-aerosol (Al_2O_3) with steady-state regimes as a function of laser intensity and particle radius. The phenomenology is determined by the energy conservation relationship

$$P_A = P_C + P_V + P_R \quad (1.1)$$

where P_A is the power absorbed from the laser beam and P_C , P_V , and P_R are the powers lost by conduction, vaporization, and radiation, respectively. At low irradiances, the aerosol heats up to a temperature T at which heat conduction losses balance the heating. In the free molecular regime ($R < 0.1 \mu\text{m}$), the heat conduction is very low because P_C is proportional to R^2 ,

whereas in the continuum regime, the conduction heat loss is proportional to the power absorption from the laser beam ($P_C \propto P_A$). The most frequently used diagnostic tools for thermo-fluid applications such as PIV, LIF and Raman scattering are in the free molecular and conduction regimes. At higher irradiances, vaporization losses (P_V) become dominant.

In the continuum regime, heat conduction becomes dominant; at higher irradiances, vaporization loss becomes dominant. The experimental breakdown thresholds are seen to occur in regimes in which particles vaporize strongly. With increasing irradiance, the start of melting, complete melting, start of vaporizing, and complete vaporization of a particle takes place in that order. The radiation losses can be avoided for particles with $R < 1$ mm.

In this work, the diagnosis of thermo-fluid phenomena is conducted in the heat conduction and vaporization regimes, not in the free molecular regime. There are few studies about diagnostics for thermo-fluid phenomena in this high irradiance regime. Diagnosing thermo-fluid phenomena in this high irradiance regime has high potential because of its many advantages, such as all-phase detection, stand-off and simple setup, etc.

1.3 Laser-Induced Breakdown Spectroscopy (LIBS) for Thermo-Fluid Diagnostics

1.3.1 Introduction of LIBS

LIBS is a type of atomic analyzer that uses the plasma generated by laser ablation. The emitted light from the plasma provides characteristic spectra for each element, and by identifying the spectra, the chemical composition of each sample can be rapidly determined, as shown in Fig. 1.3. LIBS has many advantages as a thermo-fluid diagnostic, tool such as its real-time processing and stand-off detection. In addition, all phases of material component analysis are possible. These overwhelming advantages over the previous detection techniques have led researchers to become more aware of thermo-fluid diagnostics using LIBS technology.

There have been a number of successful applications of LIBS to combustion analyses, which include determining the fuel equivalence ratios in off-gases and flames [4] and the composition measurements of hydrocarbons [5]. The chemical species in flames have also been evaluated by LIBS.

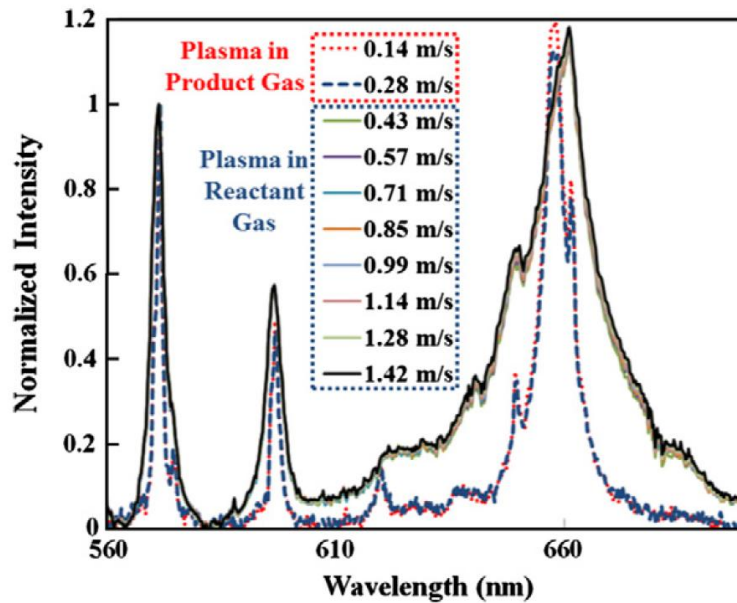


Fig. 1.3 LIBS emission spectra normalized by nitrogen line peak intensity with various reactant flow velocities in a methane premixed flame [6]

1.3.2 The theory of LIBS

A plasma is a local assembly of atoms, ions and free electrons that is overall electrically neutral and in which the charged species often act collectively. A laser is focused to form a plasma, which atomizes and excites samples. Figure 1.4 shows an image of laser-induced plasma in air. Any matter regardless of its physical state, be it solid, liquid or gas, can be evaporated by plasma owing to its high temperature (15,000-50,000 K [7]) and pressure (35 – 175 bar). Early in the process, laser-induced plasma emits intense light because of bremsstrahlung (collision between free electrons) and

recombination events. In the bremsstrahlung process, photons are emitted by electrons that are accelerated or decelerated in collisions. The electrons of the material in the plasma volume are excited to the upper energy state. Figure 1.5 shows the transition of electrons between energy levels in an atom. The electrons are excited by the plasma, and the light emission occurs at specific wavelengths. The emission intensity due to the electron transition of the atoms is relatively weaker than the early bremsstrahlung emissions. Therefore, the emissions from the electron transition can be captured after a delay (1-10 μs).



Fig. 1.4 Image of plasma in air

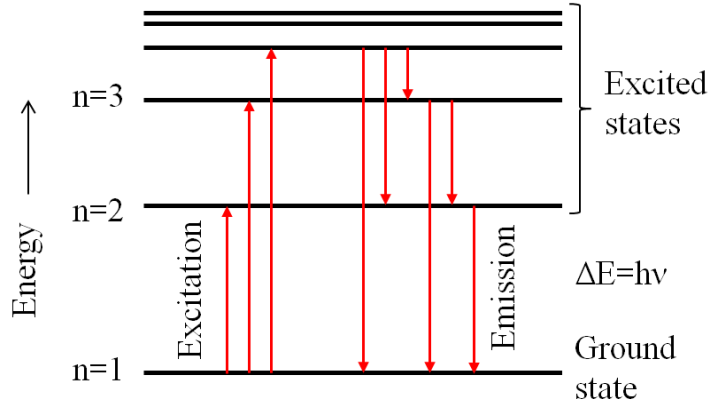


Fig. 1.5 The transitions of electrons between energy levels in an atom

The emissivity of the generated plasma plume is analyzed to obtain information on the concentrations of relevant species. When the formed plasma is in a state of local thermodynamic equilibrium, one can also obtain absolute values of the concentrations of the different species by measuring the emissivity of a transition. Thus, we can obtain absolute values of the concentrations of the different species by measuring the emissivity I_{mn} of a transition in Eq. 1.2

$$I_{mn} = \frac{h\nu_{mn}}{4\pi} A_{mn} N_m \quad (1.2)$$

where
$$N_m = \frac{N}{Q(T)} g_m e^{-\epsilon_m/kT}$$

where N_m is the density of the atoms or ions in the upper level m , A_{mn} is the Einstein transition probability of $m \rightarrow n$ transition, and N is the total density.

$Q(T)$, g_m and ϵ_m are, respectively, the atomic partition function, the statistical weight and the energy of the m^{th} level. The absolute measurement of I_{mn} is therefore equivalent to the value of N_m as well as that of N (the total species density) once the partition function of the different species and the temperature are known. In short, the emissivity is related to the density of the atoms, which can be used to diagnose thermo-fluid phenomena.

The growth of electron density is governed by the following equation

$$\frac{dn_e}{dt} = \nu_i n_e + W_m I^m n - \nu_a n_e - \nu_R n_e + \nabla(D\nabla n_e) \quad (1.3)$$

where W_m is the multi-photon ionization rate coefficient and ν_i , ν_a , ν_R are the impact ionization, attachment, and recombination rates, respectively, and D the diffusion coefficient for electrons. The multi-photon ionization rate is proportional to I^m , where m is the number of photons that have to be absorbed simultaneously in order to ionize the gas. Breakdown thresholds can be calculated by integrating Eq. 1.3. The breakdown thresholds depend on wavelength, pressure, and pulse length. At short wavelengths, or at low densities ($P < 10$ Torr in N_2) where collisional effects are small, breakdown is dominated by multi-photon ionization. The number of electrons generated per unit volume at the end of the pulse is

$$n_e = W_m n \int_{-\infty}^{+\infty} I^m(t) dt = W_m n \bar{I}^m \tau_p g(m) \quad (1.4)$$

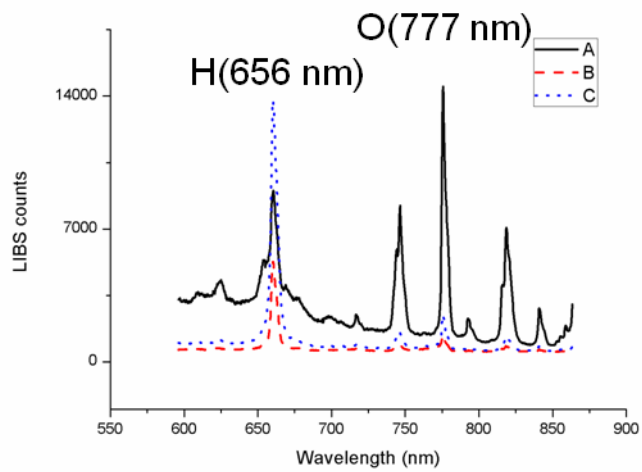
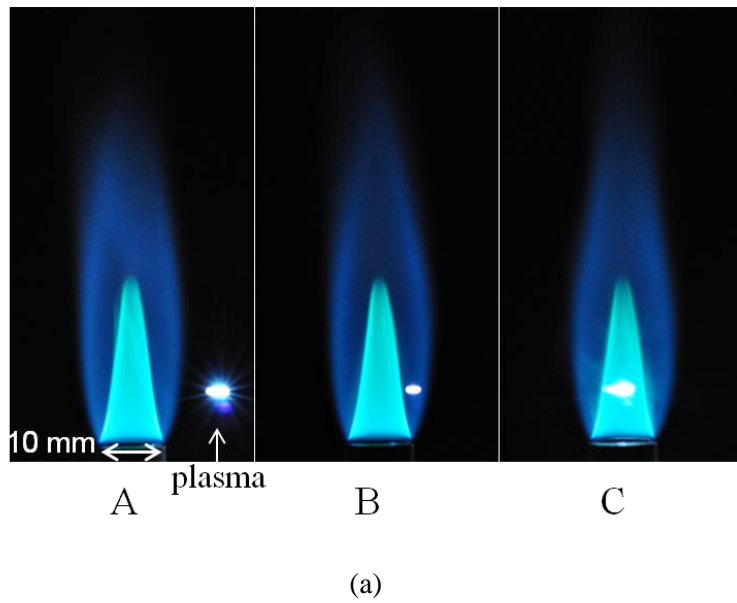
where, n , I , and τ_p are the gas density (or pressure p), irradiance and pulse duration, respectively. At high pressures ($p > 100$ Torr in N_2) and long wavelengths ($\lambda > 1 \mu\text{m}$), breakdown is usually associated with cascade ionization. The electron heating rate is proportional to gas density. All terms in the Boltzmann equation will then scale proportionately with n (or p). The scaling of the breakdown with pressure and pulse length is

$$\bar{I} \propto (p \times \tau_p)^{-1/m} \quad (1.5)$$

In short, the breakdown thresholds are functions of gas density and pulse length. The breakdown threshold is proportional to plasma intensity with the same laser irradiance. Thus, plasma intensity is related to gas density, which can be used to diagnose thermo-fluid phenomena.

$$\bar{I} \propto (p \times \tau_p)^{-1/m} \quad (1.6)$$

In short, the breakdown thresholds are functions of gas density and pulse length. The breakdown threshold is proportional to plasma intensity with the same laser irradiance. Thus, plasma intensity is related to gas density, which can be used to diagnose thermo-fluid phenomena.



(b)

Fig. 1.6 (a) Image of a premixed propane flame and plasma and (b) LIBS spectra from plasma for different plasma positions

Figure 1.6 (a) and (b) show images of a premixed propane flame, plasma and LIBS spectra from plasma in different plasma positions. The H intensity is higher at the center position of the flame because the fuel concentration is higher, whereas the O intensity is higher at the outside of the flame because of the existence of air. In addition, plasma intensity differs according to the position of the plasma in the flame; it is weak in the reaction zone where the density is low (high temperature), but it is high in the unburned zone and in the pure air zone, where density is high (low temperature). This relationship can be used to obtain the temperatures in thermo-fluid phenomena.

1.3.3 Comparison of LIBS and conventional diagnostic methods for thermo-fluid applications

Table 1.2 shows the comparison of LIBS and other laser-based methods for thermo-fluid diagnostics. Elastic scattering (such as Rayleigh scattering and Mie scattering) and inelastic scattering (such as laser-induced fluorescence and Raman scattering) are used for thermo-fluid diagnostics. Rayleigh and Mie scattering have no selectivity for chemical species because there is no loss or gain of energy by the radiation. However, LIF and Raman scattering have selectivity for the chemical species because of the changes in the energy of the radiation. LIBS also has selectivity for chemical species, and Raman scattering and LIBS can detect multiple species using a single laser pulse. Moreover, the signal intensities of Mie scattering and LIBS are strong,

whereas Raman scattering has very weak signal intensity. The setup of LIF is relatively complex in that it requires a tunable laser to generate light at specific wavelengths and an optical filter to remove the light that scatters from incident beams. The setup of Raman scattering is also complex in that it requires signal intensification and an optical filter to block the light that scatters from incident beams. However, the setup of LIBS is relatively simple, and LIBS has very high accuracy for measuring atomic chemical composition. LIBS can analyze any matter regardless of its physical state, be it solid, liquid or gas, whereas other methods can only conventionally detect gas-phase species. The disturbance of flow caused by the shockwaves from laser-induced plasma is, however, a limitation of LIBS for thermo-fluid diagnostics. The laser-induced plasma may affect the next measurement event in low speed flow because of the disturbance.

Table 1.3 shows the comparison of droplet diagnostic techniques including LIBS. There are many methods such as scattering, imaging, phase Doppler particle analyzers (PDPA) and optical patternators for diagnosing droplets. LIBS is being applied for the first time in our study to diagnose fuel droplets. PDPA and LIBS can be applied for only point measurement, and other methods can provide 2-dimensional contours. The setups for PDPA and optical patternators are relatively complex, but the setup for LIBS is very simple. The signal intensities of PDPA and optical patternators are weak, but other methods have strong signal intensity. Scattering and LIBS can be easily

optically accessible in the test area, and PDPA can measure velocity as well as droplet characteristics. Optical patternators and LIBS can measure fuel concentration as well as droplet characteristics.

Table 1.4 shows the comparison of solid particle diagnostic techniques including LIBS. Extraction, scattering, and laser-induced incandescence (LII) are used to diagnose solid particles. In the extracting method, the probe is located in the testing zone to extract solid particles, and the solid particles are sent to particle analyzers such as condensation particle counters, differential mobility analyzers and scanning mobility particle sizers. In addition, the particle information is obtained from Mie scattering and block body radiation in the scattering method and LII, respectively. The signal intensity of LII is weak, whereas other methods have strong signal intensity. Additionally, the chemical species information can be provided only from LIBS. As such, both the scattering method and LII can measure the size and distribution of particles, and LIBS can measure the chemical composition as well. However, LIBS can disturb flow because of the shockwaves from the laser-induced plasma.

Table 1.2 Comparison of thermo-fluid diagnostic techniques including LIBS

Technique	Rayleigh	Mie	LIF	Raman	LIBS
Chemical species	No	No	Yes	Yes	Yes
Multi species	No	No	No	Yes	Yes
Signal intensity	Weak	Strong	Weak	Very weak	Strong
System complexity	Low	Low	High	High	Low
Accuracy	Low	Low	High	High	Very high
Objective phase	Gas	Particle (droplet)	Gas	Gas	Gas, liquid, solid, aerosol
Measure	Density, temperature	Particle size, flow field	Chemical species, density, temperature	Chemical species, density, temperature	Atomic chemical composition, density, temperature
Flow disturbance	No	No	No	No	Yes (shock wave)

Table 1.3 Comparison of droplet diagnostic techniques including LIBS

Technique	Scattering	Imaging method	PDPA	Optical patternator	LIBS
Domain	Point and 2D	2D	Point	2D	Point
System complexity	Low	Low	High	High	Low
Signal intensity	Strong	Strong	Weak	Weak	Strong
Optical access	Easy	Difficult	Difficult	Difficult	Easy
Additional information	No	No	Velocity	Fuel concentration	Fuel concentration

Table 1.4 Comparison of solid particle diagnostic techniques including LIBS

Technique	Extraction	Scattering	LII	LIBS
Principle	Using probe, extract particle	Mie scattering	Black body radiation	Laser plasma
Signal intensity	N/A	Strong	Weak	Strong
Chemical species	Yes	No	No	Yes
Measure	Size, distribution, chemical composition	Size, distribution	Size, distribution	Size, distribution, chemical composition
Merits	High resolution	In-situ, real time	In-situ, real time	In-situ, real time, multi-species detection
Limits	Complex, impossible in situ and real time	Impossible detection of chemical composition	Impossible detection of chemical composition	Flow disturbance

1.3.4 LIBS for thermo-fluid applications

Figure 1.7 shows the H/N atomic intensity ratios with H/N in combustion products from methane and ethylene premixed flames [6]. All of the data points are on a single line, which implies that the correlation works for both ethylene and methane combustion products. In addition, the H/O LIBS intensity ratio is correlated with the equivalence ratio [8]. The equivalence ratio (Φ) is defined as the local fuel to oxidizer mass fraction divided by the stoichiometric fuel to oxidizer mass fraction for the particular mixture [9].

$$\phi = \frac{m_{fuel} / m_{air}}{(m_{fuel} / m_{air})_{st}} \quad (1.7)$$

The H/O atomic line intensity ratio can be simply related to the flame global equivalence ratio. Using this correlation, LIBS can be used to obtain quantitative local equivalence ratios in flame.

Moreover, there are many applications of aerosol analysis that use LIBS to detect industrial exhausts [10, 11] and biological aerosols [12] in flow. Figure 1.8 (a) and (b) show the schematic of the LIBS system used for a power generation boiler and the spectrum of metallic particles from the exhaust stream [11]. The existence of metals and other inorganics in the combustion products of boilers and industrial furnaces can have deleterious effects on furnace refractory materials and boiler convection pass heat transfer surfaces. LIBS can be used as a continuous-emission monitor of toxic-metal concentrations in exhaust streams. Applied in situ, LIBS offers a rapid

response relative to the other techniques and avoids some of the uncertainties associated with extractive probes.

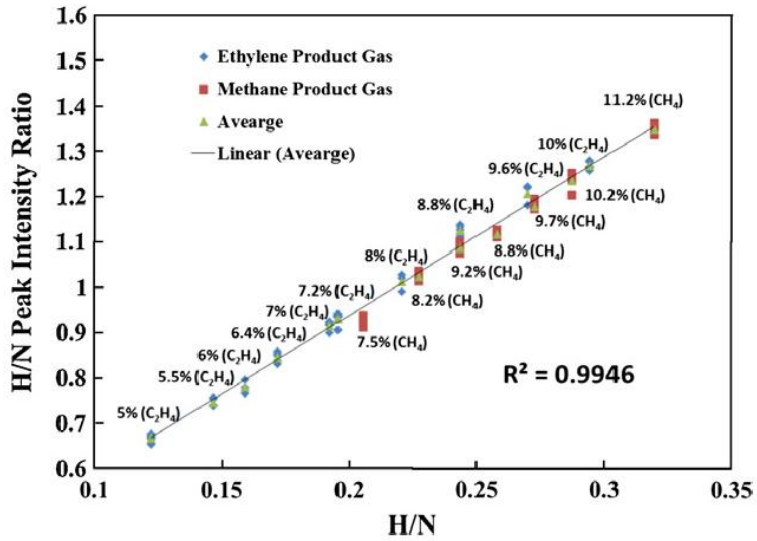
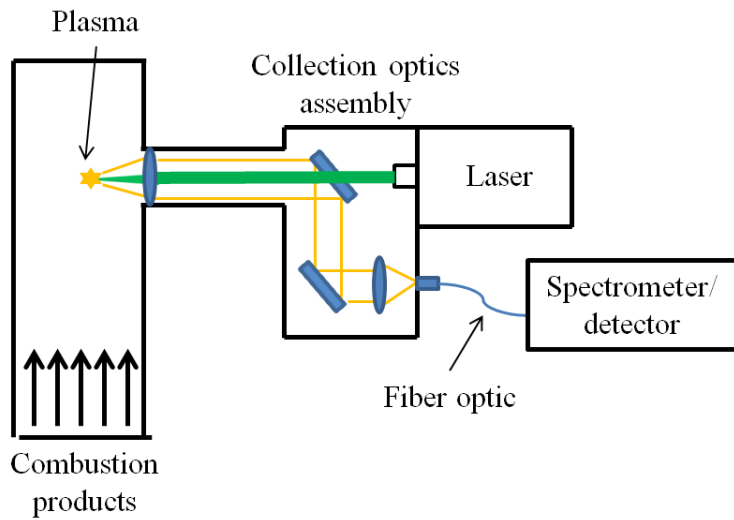
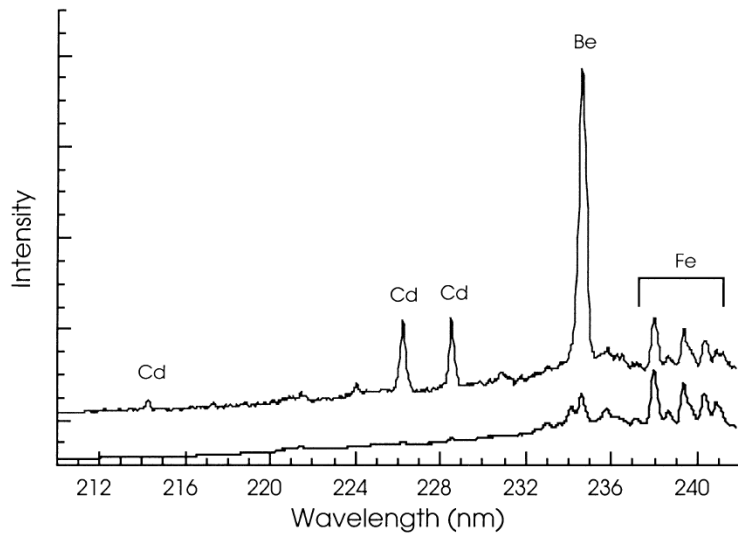


Fig 1.7 H/N intensity ratios versus H/N in combustion products from methane and ethylene premixed flames [6]



(a)



(b)

Fig. 1.8 (a) Schematic of a LIBS system used for a power generation boiler;
 (b) spectrum of metallic particles from the exhaust stream [11]

As shown in the two examples, LIBS can be applied for thermo-fluid diagnostics, and it has high potential for obtaining the important parameters such as temperature, density, and concentration of chemical species in thermo-fluid phenomena. Thus, many people have been developing methods for obtaining various chemical and physical parameters using LIBS. The temperature in reacting flow was obtained using laser-induced plasma by Kiefer et al. [13]. In addition, laser-induced breakdown was used to quantitatively measure gas properties (gas density and fuel concentration) [14], and the metallic nanoparticles from flame synthesis [15] and coal combustion [16] can be detected using LIBS.

In our study, we made an effort to discover the characteristics of laser-induced plasma to diagnose materials in various phases. Two-dimensional mapping of the propane flame allows for spatial dimensionality in a conventional LIBS point measurement. Information about the dissociated chemical species (gas phase) and soot (solid particle phase) that would have been unattainable via any other means is provided by the present system. In addition, we can conduct laser ignition and laser-induced breakdown spectroscopy of liquid-phase fuel droplets mixed with the air. The quantitative measurement of the liquid-phase fuel concentration can be obtained. The equivalence ratios and liquid fuel volume fractions are simultaneously obtained from the laser-induced plasma from the fuel spray. A fuel/air ratio feedback controller that uses a single laser source for both optical

spectroscopy breakdown and subsequent ignition of the two-phase spray could potentially be designed. Finally, the feasibility of LIBS for detecting solid particles from high-speed jet engine exhaust is examined. The particles and plasma are visualized in order to validate the LIBS signals of a high-speed jet flow. We describe how we use the LIBS signals to confirm our detection of carbon from a high-speed jet exhaust.

1.4 Laser-Induced Ultrasound Wave for Thermo-Fluid Diagnostics

1.4.1 Introduction of LIUS

Thermoelastic expansion is usually the most efficient mechanism for generating acoustic waves. Figure 1.9 shows a typical configuration of optical generation of ultrasound using thermoelastic expansion. A laser pulse is focused onto the film surface, and optical absorption rapidly causes a temperature increase in a localized volume in the film where thermal expansion launches an acoustic wave into the overlying sample. The generated acoustic wave can be used to diagnose thermo-fluid phenomena.

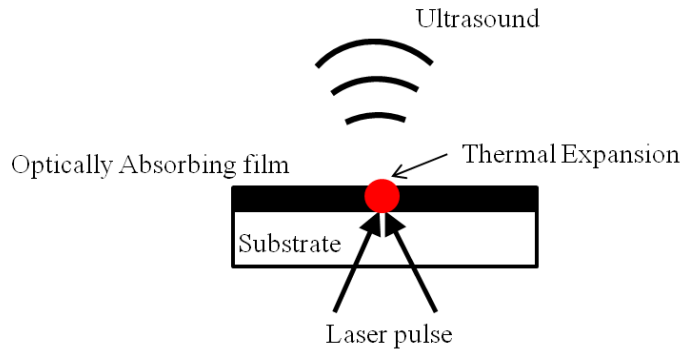


Fig. 1.9 Typical configuration of optical generation of ultrasound using thermoelastic expansion

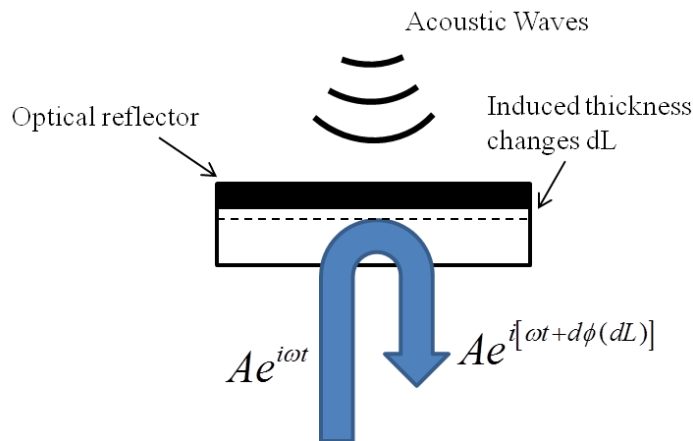


Fig. 1.10 Typical scheme for passive optical detection

The generated ultrasound wave is reflected from the objective, and the reflected acoustic wave is detected by optical detection. Optical detection of ultrasound has been studied for a number of decades. The most straightforward principle is called passive optical detection, as shown in Fig. 1.10—a laser source probes a transducing surface that consists of an optical

reflector, which can simply be a thin, highly reflective optical pellicle. Acoustic waves in the reflector surface phase modulate the probing laser beam in proportion to surface displacements. Thus, the detailed configuration of the objective can be constructed from the obtained acoustic wave signals. In this study, we focus on generating ultrasound waves.

Laser-generated ultrasound is a common tool for nondestructive testing. Laser-induced ultrasound generation effectively provides a high-frequency signal with a broad acoustic bandwidth. A material ejects specific acoustic waves according to its own optical absorbance and thermoelastic properties. By detecting and processing wave signals, surface images and underlying structures can be constructed with high resolution [17].

The stress production by laser impact is classified into four regimes: dielectric breakdown, electrostriction, vaporization, and the thermoelastic process [18]. These four regimes are developed by the laser's fluences on the material. A highly irradiant focused beam causes dielectric breakdowns and generates shockwaves. When the laser fluence is decreased, stress waves with lower intensity are produced with no damage to the material. These low-intensity stress waves are generated from the thermoelastic process.

To generate stronger waves, a number of coatings have been tested to reduce the reflectance on the metal [19]. Even a highly thermoelastic material needs sufficient heat to increase in pressure. The high optical reflectivity of

the metal interrupts the heat transfer from the laser beam to the metal. The irradiated energy of a Gaussian beam is given by Eq. 1.8,

$$Q = (1 - R) \times \mu I_0 e^{\mu z} \times \frac{1}{\sigma \sqrt{2\pi}} e^{-\frac{(t-m)^2}{2\sigma^2}} \quad (1.8)$$

where R is a reflection coefficient, μ is the absorption coefficient of a material, and I is the laser fluence. Several alternative optoacoustic transmitters are available for improving light absorbance.

In this work, reduced graphene oxide (rGO) is tested as an optoacoustic transmitter. Many other researchers have investigated the basic properties of graphene, considered a miracle material with superior electronic, thermal, optical, and mechanical properties [20]. To generate high-frequency waves of high intensity, the properties of the laser-generated ultrasound are tested with an RGO coating on an aluminum and polydimethylsiloxane (PDMS) thin film. The properties of the laser-generated acoustic wave are characterized by the intensity and pulse width of the pressure wave. The generated high-frequency ultrasound wave can be used for diagnostic of thermo-fluid phenomena in the future.

1.4.2 The theory of LIUS

The typical laser fluence in the thermoelastic regime is less than 10^7 W/cm² for a metal. In this regime, amplitudes of shear and surface waves increase linearly with increasing power density. Generation of ultrasound in the

thermoelastic regime occurs through thermal mechanisms. Elastic waves are generated by strains that arise from thermoelastic expansion on the plane of the surface. Physically, this can be thought of as rapid heating by the laser pulse of the thin film with subsequent rapid expansion. The generation of thermal and elastic waves caused by converting light into heat is described by the coupled thermal-diffusion and elastic-wave equations. Thermoelastic generation of acoustic waves is governed by two equations: the heat conduction equation and the wave equation. The heat conduction equation, which determines the temperature distribution, is shown in Eq. 1.9 [21]

$$k \frac{\partial^2 T}{\partial x^2} - \rho C_v \frac{\partial T}{\partial t} = -H \quad (1.9)$$

$$\text{where } H = \frac{\beta}{2} e^{-\beta x} (1-R) I_0(t)$$

where T is the temperature, k is the thermal-conductivity, C_v is the specific heat at constant volume, and β is the optical absorption coefficient. H is the heat source density, and R is the optical reflectance of the sample surface. $I_0(t)$ is the incident intensity of the light.

The wave equation for the scalar potential ϕ is given by Eq. 1.10 [22].

$$\nabla^2 \phi - \frac{1}{c^2} \frac{\partial^2 \phi}{\partial t^2} = \frac{3B}{\rho c^2} \alpha_L T \quad (1.10)$$

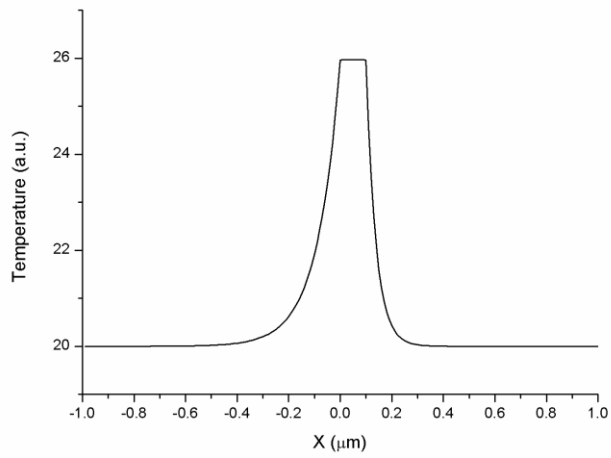
where c is the longitudinal wave speed in the medium, B is the bulk modulus, and α_L is the linear coefficient of the thermal expansion. The

pressure is related to the scalar potential by $p = -B\nabla^2\phi$. The pressure can be written as Eq. 1.11

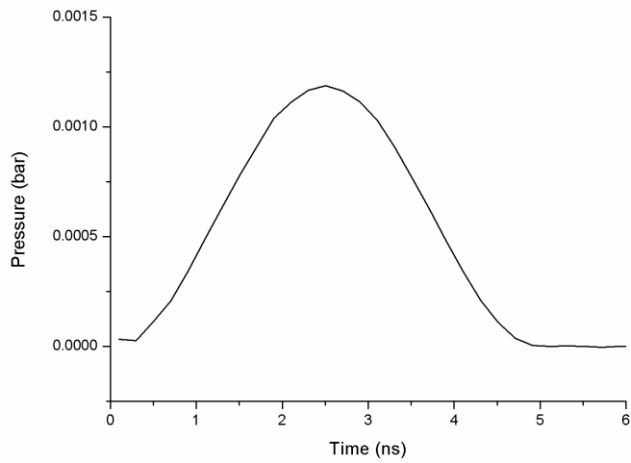
$$p = \frac{1}{4\pi} \frac{3B^2\alpha_L}{\rho c^2} \int dr \frac{\partial^2 T}{\partial t^2} \quad (1.11)$$

The intensity of ultrasound waves depends on temperature distribution, which is determined by laser intensity, optical and thermal properties such as absorptivity and thermal conductivity, and mechanical properties of the material such as its thermal expansion coefficient, bulk modulus, etc.

Figure 1.11 (a) shows the calculated temperature distribution along the cross plane of Al film in water at a thickness of 100 nm. A rapid temperature increase is observed on the surface of the Al film, but the temperature rapidly decreases because of the heat loss in the water. Figure 1.11 (b) shows the time related to the acoustic wave propagation and attenuation by the laser pulse for Al film, which is calculated from the temperature distribution in Fig. 1.11 (a). We can confirm that the ultrasound wave with high frequency is generated by the laser pulse. This unique feature can be used to diagnose thermo-fluid phenomena.



(a)



(b)

Fig. 1.11 1-dimensional analysis of optoacoustic wave generation: (a) the time constant of heat propagation in the Al layer; (b) the time related to the acoustic wave propagation and attenuation by the laser pulse for Al film

CHAPTER 2

EXPERIMENTAL SETUP

2.1 Experimental apparatus

2.1.1 Laser

A Surelite Nd:YAG laser (Continuum) was used to generate the plasma and acoustic waves (Fig. 2.1). Surelite lasers emit four wavelengths—1064 nm, 532 nm, 355 nm and 266 nm—using a harmonic generator and a dichroic mirror. Maximum energy at 1064 nm is 450 mJ at a 10 Hz repetition rate.



Fig. 2.1 Surelite Nd:YAG laser

A Minilite Nd:YAG laser (Continuum) was applied for the visualization of liquid droplets, particles and acoustic waves (Fig. 2.2). The wavelength was 532 nm with 25 mJ maximum pulse energy.



Fig. 2.2 Minilite Nd:YAG laser

2.1.2 Spectroscopy

To diagnose thermo-fluid phenomena, plasma is collimated on the entrance slit of the echelle grating spectroscopy (Andor Mechelle), coupled with the gated ICCD (Andor, iStar), which allows for simultaneous spectral recording in the range 200 to 975 nm with a spectral resolution ($\lambda/\Delta\lambda$) of 5000, namely, 0.1 nm resolution (Fig. 2.3).



Fig. 2.3 Mechelle spectroscopy

2.1.3 Hydrophone

Laser-induced ultrasound waves are detected by a hydrophone (onda. Inc). Two types of hydrophones are used to measure broadband frequency (membrane type 0.5-45 MHz, needle type 0.25-10 MHz), as shown in Fig. 2.4.



(a)



(b)

Fig. 2.4 Hydrophone: (a) membrane type; (HMB-0500) (b) needle type (HNR-1000)

2.2 Shadow graph

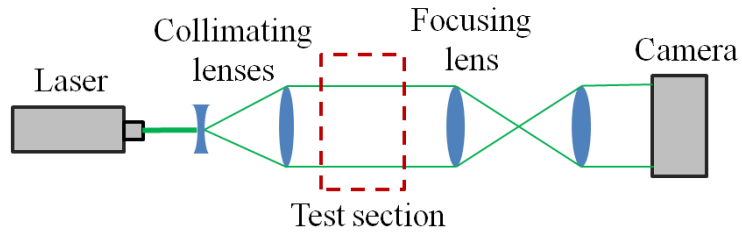


Fig. 2.5 Shadow graph setup

Figure 2.5 shows the shadow graph setup for visualizing the acoustic waves, which took place using another Nd:YAG laser (Minilite, Continuum Inc.) at 532 nm wavelength, 5 ns pulse duration, and 25 mJ per pulse of energy. The visualization laser was diverged through a concave lens with a focal length of 30 mm. The diverging beam was collimated by a convex lens with a 500 mm focal length. Passing through the test section, the collimated beam was focused by a convex lens with a 100 mm focal length. Finally, the laser beam is captured by a CCD camera (Nikon) for the visualization. If a density change is detected in the acoustic field of water, the laser beam strayed from its direction so as to allow shadow-graphic imaging.

2.3 Light scattering

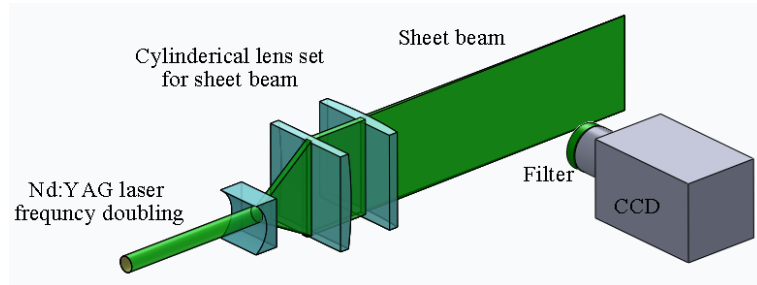


Fig. 2.6 Light scattering setup

Figure 2.6 shows the light scattering setup for visualizing solid particles and liquid droplets. We use a 532 nm Nd:YAG laser (minilite, Continuum Inc.), which has an energy of 25 mJ/pulse and a beam diameter of 3 mm. The laser is irradiated as a thin sheet through one cylindrical and two convex lenses, which have 30 mm and 50 mm focal lengths, respectively. The solid particles or liquid droplets emit the Mie scattering light, and the CCD camera captures the scattered light through an optical filter that can only pass scattered light.

CHAPTER 3

DIAGNOSTIC OF GAS PHASE REACTING FLOW USING LIBS [23]

3.1 Background and objective

Laser induced breakdown spectroscopy (LIBS) is based on the optical spectroscopy of laser-induced plasma generated by the breakdown of a target gas, liquid, or solid. There have been several successful applications of LIBS to combustion analyses, which include the identification of industrial exhausts [10, 11] the determination of fuel equivalence ratio in off-gas and flame [4, 24, 25], and composition measurements of hydrocarbons [5].

The chemical species in the flame have also been evaluated by LIBS. Eseller et al. used LIBS with an ungated detector for the LIBS-based diagnosis of methane and biodiesel flames [26]. They also used N, O, and H LIBS signals from a CH₄/air flame to determine the equivalence ratio. Mansour et al. evaluated a turbulent premixed flame using double pulse LIBS method [27]. Kiefer et al. evaluated methane and DME (dimethyl ether) flames using LIBS [28]. They provided the optimal laser energy to generate laser plasma, and the fuel/air equivalence ratio according to the flame radial position. Rai et al. measured the metallic particles in a hydrocarbon flame for

rocket engine health monitoring using LIBS [29]. Kotzagianni and Couris conducted combustion diagnostics using a femtosecond LIBS with varying delay time and laser energies [30]. Do and Carter confirmed that the short-gated LIBS signal of the H/N ratio can provide fuel concentration with good accuracy in an unsteady reacting flow [6]. Tripathi et al. demonstrated that LIBS-based calibrations perform better in equivalence ratio predictions for premixed atmospheric methane-air flames compared to chemiluminescence-based equivalence ratio measurements [31]. Michalakou et al. used LIBS to measure the equivalence ratios in methane-air, ethylene-air, and propane-air mixtures [32]. They demonstrated that the LIBS signal ratios of H(656.3 nm)/O(777 nm) and C(833.5 nm)/O(844.6 nm) from Bunsen burner laminar flames showed good correlations with the reference equivalence ratio.

Thus far, the application of LIBS to combustion diagnostics has focused on the measurement of chemical species in small local volumes or along a one-dimensional line. No regional information or multi-dimensional mapping of the chemical species by LIBS-based methodology has been attempted until now. For the illustration of such 2-D mapping of a flame via LIBS, we consider a gas mixture of hydrogen and hydrocarbon. Hydrogen is a potential fuel for generating clean energy without pollution, and researchers have continued to study its flame [33, 34]. However, severe flashback and unstable flame propagation in lean burning conditions limit its use in most practical combustors. Hydrogen also explodes easily because of its wide flammability

limits (4.65% ~ 93.9%), and thus requires special handling for safety. An approach to overcome these drawbacks is to use a mix of hydrogen and hydrocarbon fuels. The combustion mechanisms of hydrogen-hydrocarbon mixtures have been studied rather extensively in the past [35, 36]. Electrolytic OxyHydrogen (EOH) gas is a stoichiometric mixture of hydrogen and oxygen produced from water through electrolysis [37]. As water electrolysis is quite instantaneous, EOH can be produced on demand without the need for storage. Nonetheless, the combustion mechanism of the EOH-hydrocarbon mixture has not been studied in detail.

In this work, we consider a liquefied petroleum gas (LPG)-EOH flame for chemical analysis via LIBS. Two-dimensional mapping allows for spatial dimensionality in a conventional LIBS point measurement. Information about the dissociated chemical species (gas phase) and soot (solid particle phase) unattainable via any other means are provided by the present system. We present both atomic and molecular chemical contours of LPG, LPG-EOH mixture, and LPG-AIR mixture flames.

3.2 Experimental condition

Figure 3.1 shows the experimental set-up. A Brown Gas Generator (Best Korea, BB-2000) generates EOH gas, which is mixed with LPG gas through mass flow controllers (MFCs) to control the flow rates. The mixed fuel is fed into a burner through a co-axial nozzle with its inner hole (0.68-mm diameter)

and outer hole (3.1-mm diameter) separated by a 2-mm circular wall. The burner traverses along the x and y axes for resolved point measurements at varied grid positions to construct 2D images. The LIBS system is used to map out the contour of flame chemical information. The plasma is generated by a laser beam (Continuum Inc., Powerlite) with a wavelength of 532 nm through a convex lens that has a 120-mm focal length. Since the flame density differs according to the fuel, the laser energy that generates plasma is changed for different fuel mixtures. The laser energies selected for generating plasma are 200 mJ for LPG flowing at 50 ccm (cubic centimeter per min), the LPG 50 ccm–EOH 10 ccm mixture, and the LPG 50 ccm–AIR 10 ccm mixture flames, and 500 mJ for the EOH 500 ccm and the EOH 500 ccm–LPG 70 ccm mixture flames. These laser energies are the minimum values needed to generate laser plasma to provide a sufficient LIBS signal. The plasma light is collected by a quartz lens with a 100-mm focal length, which is perpendicular to the laser direction for LIBS analysis. The plasma light collected is sent to an echelle spectrometer (Andor Mechelle 5000) with 0.1-nm resolution, and an ICCD (Andor iStar 1024 × 1024) to record the signal. A 2- μ s delay time and 20- μ s TTL width are used for LIBS measurements. Several atomic and molecular band peaks are selected for mapping the chemical signals (C: 247.8 nm, CN band: 388.3 nm, C₂: 516.2 nm, H: 656.2 nm, O: 777.3 nm). Also, the laser is irradiated from the left side, and plasma light is collected at 90° to the laser direction. So, the LIBS signal on the left side of the flame is

higher than on the right side. Figure 3.2(a) shows an image of a flame of LPG flowing at 50 ccm. This hydrocarbon flame is optically divided into yellow, dark, and blue zones [33]. The dark zone is basically an indication of fuel pyrolysis and soot inception. This zone is followed by a yellow-luminous zone where soot burning is dominant, and a blue zone that represents the gas-phase oxidation region. The flame species contour is obtained by moving the burner in 0.5-mm steps in a grid with 20-mm height and 16-mm width. Figure 3.2(b) represents a LIBS spectrum at a single position in the flame (-1 mm, 0 mm). Multiple mappings of the entire grid can be performed to provide chemical species information about the chosen area. Each data point used corresponds to the averaged quantity obtained by taking 10 shots at each position.

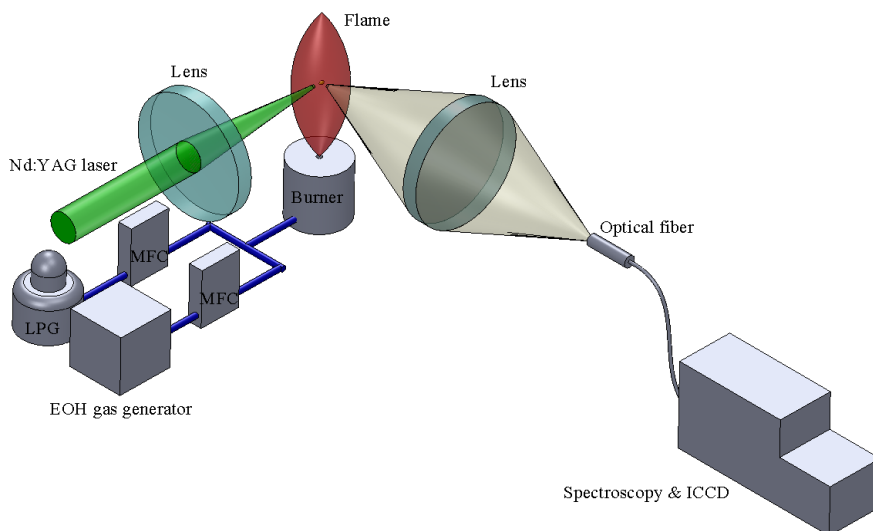
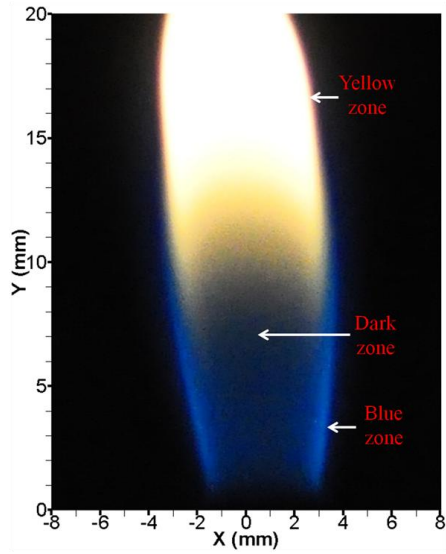
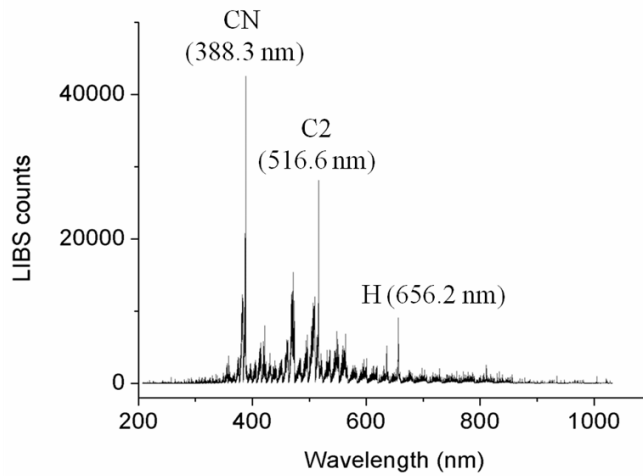


Fig. 3.1 Experimental setup



(a)



(b)

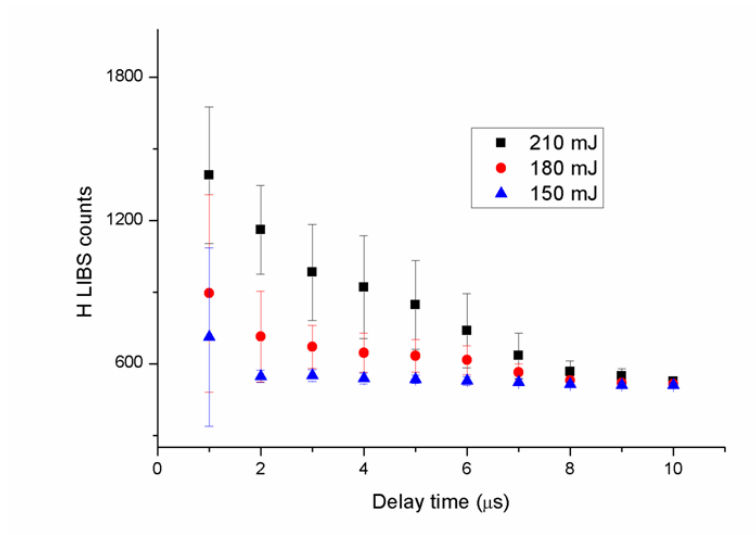
Fig. 3.2 (a) Flame image of LPG 50 ccm, (b) spectrum of LPG flame at 2 mm above the burner from 200 mJ laser energy at 2 μ s delay time. Three peaks of CN (388.3 nm), C₂ (516.6 nm) and H (656.2 nm) are identified.

3.3 Results

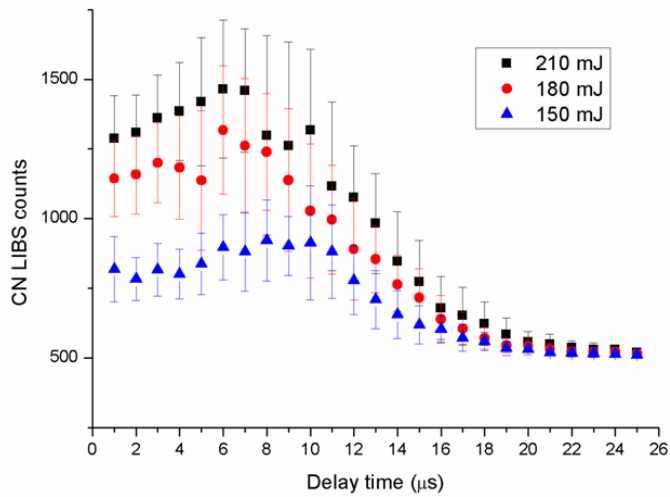
Figure 3.3 (a) and (b) respectively show the H atomic peak (656 nm) and CN molecular band (388 nm) according to the delay time for different laser energies (150 mJ, 180 mJ and 210 mJ) with a gate width of 5 μ s. The H atomic peak is decayed with increasing delay time. When the laser energy decreases, the H peak decay becomes faster. The CN band peak increases from the initial delay time to a delay time of about 6 μ s. The CN band peak is decayed from a delay time of about 6 μ s to a delay time of 25 μ s. Eseller et al. demonstrated that the atomic peaks of elements such as Ar, N, and O are dissipated at 2 μ s delay time [38]. However, in our results, the atomic and molecular peaks are dissipated at about 10 μ s and 25 μ s, respectively. This is because the experimental conditions regarding laser energy, ICCD exposure time, and ICCD gain are different [38]. In our experiment, we used the delay time of 2 μ s for obtaining both the atomic and molecular signals.

Figure 3.4 (a) shows the measurement grid for an LPG 50-ccm flame. Each measurement yields a spectrum similar to that in Fig. 3.2 (b). Figure 3.4 (b) shows the LIBS contour of the base signal for a flame of the LPG 50 ccmalone. The base is the averaged intensity of the entire LIBS spectra from 320 to 350 nm. Figure 3.4 (c) and (d) show the LIBS base signal mappings for mixture flames of LPG 50 ccm–EOH 10 ccm and LPG 50 ccm–AIR 10 ccm, respectively. The base signal depends on the plasma intensity, which is related to the density field of a flame, and provides the flame density information.

This interaction between the plasma intensity and density can be used for measuring flame temperature [13, 39]. The flame of LPG 50 ccm alone is shown to have high density in the fuel jetting region, and the mixture flames (LPG 50ccm– EOH 10ccm, LPG 50ccm–AIR 10ccm) have relatively lower density in the corresponding region due to the existence of oxygen in the fuel mixture. In the mixture cases, the primary oxygen and fuel burn from the inside outwards, so the density in the fuel jetting region becomes low. The burning region has a low density field, and the outside of the flame has a high density field due to the high concentration of air for all cases. Thus, when analyzing a flame with LIBS, signal-to-base ratios or peak-to-peak ratios must be used to avoid any unwanted signal changes due to the differences in density.



(a)



(b)

Fig. 3.3 LIBS signal according to delay time for different laser energy (a) H atomic peak (656 nm) and (b) CN molecular band (388 nm)

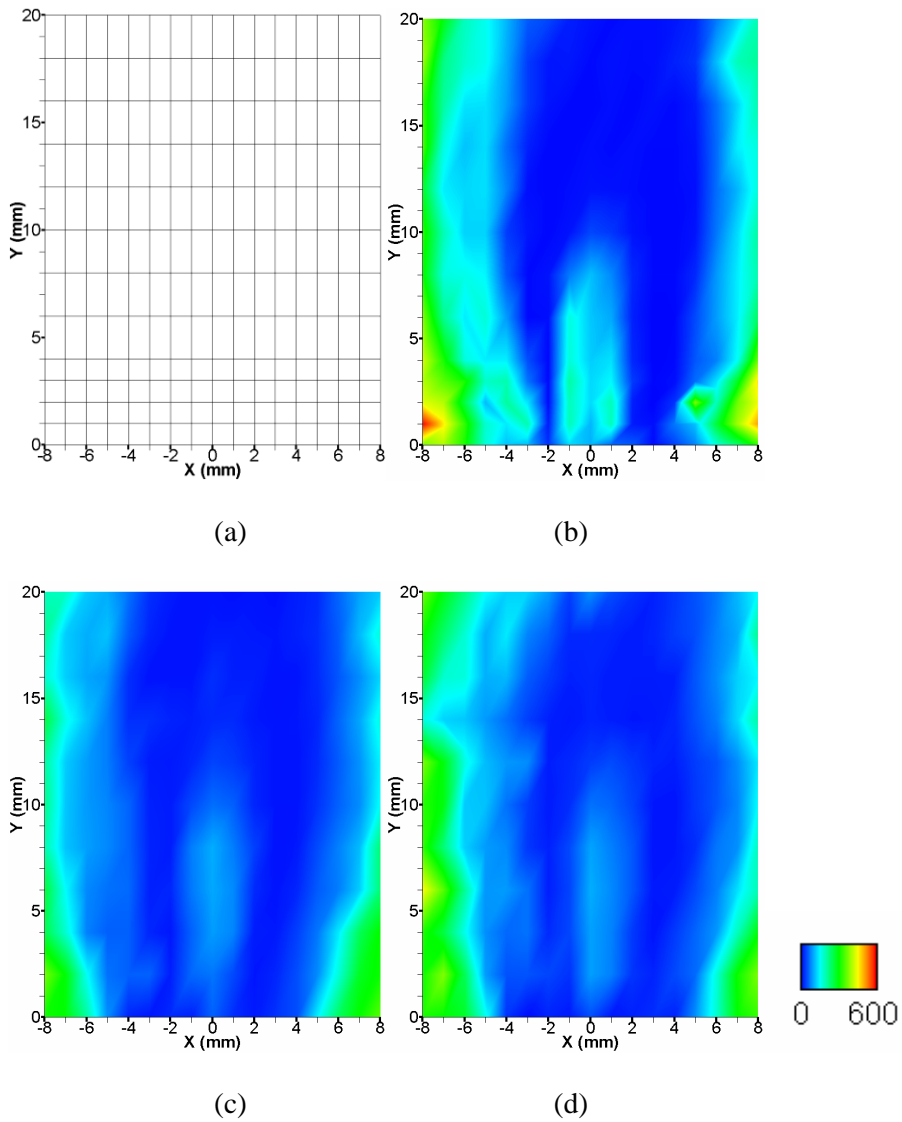


Fig. 3.4 Density mapping of LPG flame using LIBS base signal (a) measurement positions, (b) LIBS base signal mapping of LPG 50 ccm flame, (c) LIBS base signal mapping of LPG 50 ccm-EOH 10 ccm, (d) LIBS base signal mapping of LPG 50 ccm-AIR 10 ccm

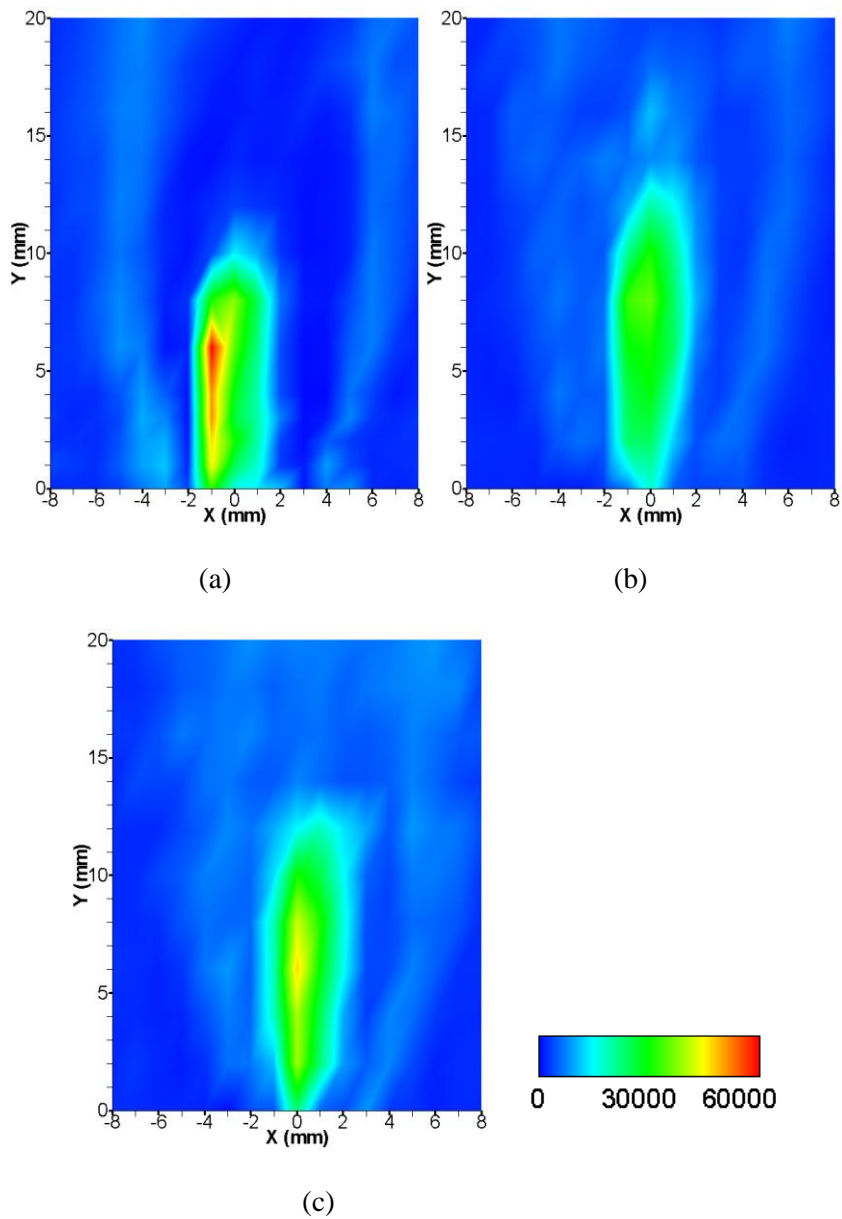


Fig. 3.5 CN LIBS signal mapping for (a) LPG 50 ccm (b) LPG 50 ccm-EOH 10 ccm mixture (c) LPG 50 ccm-AIR 10 ccm mixture flame with 200 mJ laser energy and 2 μ s delay time

Figure 3.5 (a), (b), and (c) show the CN LIBS mapping for LPG 50 ccm alone, the LPG 50 ccm–EOH 10 ccm mixture, and the LPG 50 ccm–AIR 10 ccm mixture, respectively. The CN band peak from the previous LIBS study is used for measuring the concentration of fuel [30, 40]. In our results, the CN band peak is high at the center position of the flame and low at the outside position, as shown in Fig. 3.5 (a). The fuel is diffused to outside of the flame, thus the observed tendency looks quite reasonable. LPG–EOH and LPG–AIR flames have higher temperature than the LPG flame since additional oxidizer is included in the mixture. So, the CN band peaks decrease in the LPG–EOH and LPG–AIR mixture flames due to the low plasma intensity, as shown in Fig. 3.5 (b) and (c). However, the qualitative tendency showing a high signal at the center position of flame and a low signal outside the flame is similar in all the LPG, LPG–EOH, LPG–AIR flames.

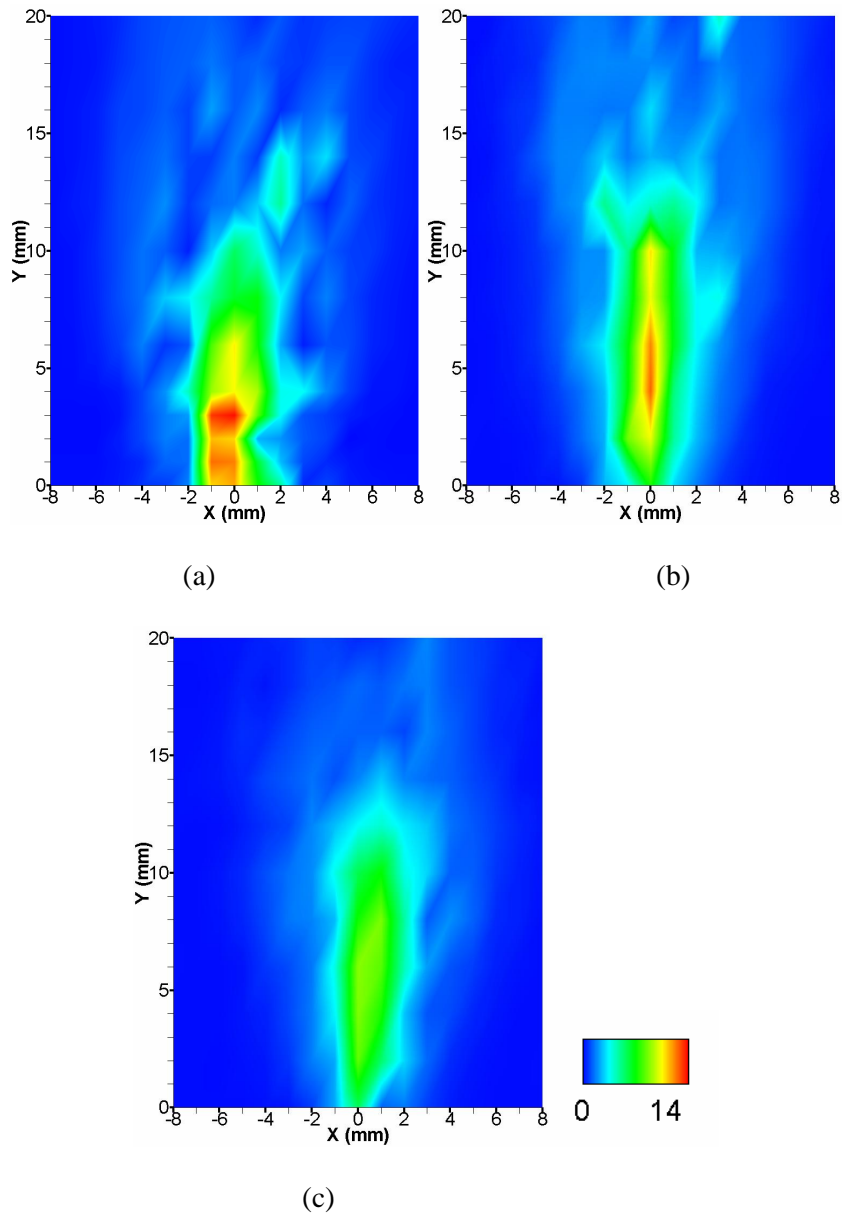


Fig. 3.6 H/O LIBS signal ratio mapping for (a) LPG 50 ccm (b) LPG 50 ccm-EOH 10 ccm mixture (c) LPG 50 ccm-AIR 10 ccm mixture flame with 200 mJ laser energy and 2 μ s delay time

Figure 3.6 (a), (b), and (c) show the H/O LIBS signal ratios for LPG 50 ccm, the LPG 50 ccm–EOH 10 ccm mixture, and the LPG 50 ccm–AIR 10 ccm mixture flames, respectively. The H/O LIBS ratio can be used for measuring the fuel/air equivalence ratio in the flame [28]. The H/O LIBS signal ratio has high intensity in the fuel jetting region, and gradually decreases along the radial direction in the figures. The results are consistent with those presented in a previous study by Kiefer et al. [28]. The H/O LIBS ratio for the LPG 50 ccm–EOH 10 ccm mixture in Fig. 3.6 (b) has lower intensity than that of the LPG 50-ccm flame due to the higher oxygen concentration shown in Fig. 3.5 (a). When EOH is added to the LPG flame, the fuel jetting region becomes longer due to the increased fuel jetting speed, as shown in Fig. 3.6 (b). Also, the high-intensity H/O ratio region is narrower when EOH gas is added, since the fuel burns throughout the flame due to the presence of oxygen in the flame. The H/O LIBS ratio for the LPG 50 ccm–AIR 10 ccm mixture in Fig. 3.6 (c) is lower than that for the LPG 50 ccm–EOH 10 ccm mixture. This is because there is no additional hydrogen, but oxygen from the air is added to the LPG 50 ccm–AIR 10 ccm flame.

3.4 Conclusion

We have presented a novel effort to generate two-dimensional maps of the chemical information of LPG, LPG–EOH mixture, and LPG–AIR mixture gas flames, using LIBS point-measurements at various positions. The LIBS base signal provides the density field of a flame via the relation between the density and the laser plasma intensity. The CN LIBS signal represents concentration of the LPG fuel. The H/O LIBS signal provides the fuel/air equivalence ratio in the flame. Thus, additional flame information unavailable via other means, such as density, atomic and molecular concentrations, and fuel/air equivalence ratio, is provided by the two-dimensional LIBS mapping technique presented in this work.

CHAPTER 4

DIAGNOSTIC OF TWO PHASE (LIQUID-GAS) REACTING FLOW USING LIBS

4.1 Background and objective

Spark-ignition (SI) engines based on direct injection (DI) promise significant advantages in terms of thermal efficiency and power output, and present a means of overcoming problems related to knocking, backfiring, and preignition. Although spark ignition is standard for automotive engines, there are disadvantages associated with the use of electrical spark plugs. The ignition location is restricted to the electrode gap and energy loss occurs since the plug is a heat sink and interacts with the flow field. Varying the ignition energy is restricted by the low repeatability. The ignition reliability of electric spark plugs eventually declines due to carbon fouling, which is the most common spark plug related failure.

Laser-induced breakdown in the fuel-air mixture has been studied for several decades with recent notable attempts to overcome the weaknesses of spark ignition [41-46]. Laser ignition as opposed to spark ignition has advantages such as i) no need of a spark plug, ii) precise triggering, iii) a flexible selection of fuel breakdown locations and immediacy, iv) wide range

of ignition energy (30 ~ 300 mJ), and v) good reproducibility.

Laser ignition in gas phase fuel has been studied by many researchers. A review of laser ignition research in gas fuel was published by Phuoc [47]. Research on laser ignition for two-phase flow is less common. Laser-induced spray ignition has been explored for reciprocating engines [48, 49] and aviation engines [50, 51]. Laser ignition has benefits for reciprocating engines and aviation gas turbines due to the ability to adjust the ignition position and to generate multiple ignition. Moreover, laser ignition can generate reliable ignition of lean mixtures, which has high potential for applications in lean premixed prevaporized combustion [50].

On the other hand, the ignition process in DI engines is time dependent and complex, since it is greatly influenced by many factors such as the local fuel equivalence ratio, gas density and condensed-fuel concentration. The local equivalence ratio near the ignition position at the time of ignition is particularly important for successful ignition due to a stratified fuel concentration near the ignition position. A variety of optical techniques have been used previously to measure the local equivalence ratio, including infrared (IR) absorption, planar laser-induced fluorescence (PLIF) [52], and Raman scattering [52]. Spontaneous Raman scattering and coherent anti-Stokes Raman spectroscopy can provide species concentration and gas temperature/density. However, the Raman signal is very weak and is thus susceptible to fluorescence/emission interferences. Furthermore, the

complexity of pulsed Raman scattering measurement may limit its application in laboratory environments. Alternatively, LIBS has high potential in combustion applications due to its high emission intensity and minimal system complexity. Ferioli et al. [4] used LIBS on engine exhaust gas to illustrate the ability of this technique to measure the equivalence ratio of SI engines. LIBS was successfully applied to understand the mixture dynamics inside a turbulent premixed combustor with strong pressure oscillations in ref. [53]. Do et al. measured fuel concentration and gas density simultaneously in a supersonic wind tunnel using LIBS [14]. In [23], a two-dimensional LIBS was proposed as a meaningful diagnostic tool for flame analysis. However, most research on LIBS is conducted in gas phase reacting flow.

So, the idea behind our study is a combination of laser ignition and spectroscopy for feedback control of fuel injection. Simultaneous laser ignition and spectroscopy can be used to rapidly determine the local equivalence ratio and condensed fuel concentration before the fuel is consumed. Monitoring of these instantaneously varying flow properties would be desirable particularly for the incipient vehicle acceleration period when the combustor flow enthalpy is insufficient to initiate and sustain stable combustion reactions, thus requiring a systematic feedback control strategy. A novel feedback control strategy for flame ignition and stabilization simultaneous with insitu combustion flow diagnostics is developed in the present study.

Measuring fuel properties (such as equivalence ratio and liquid phase fuel volume fraction) at possible ignition and/or flame residence locations in a SI engine is key for executing a feedback control strategy since the properties can potentially suggest optimal ignition/stabilization locations under harsh combustor conditions. Focused laser energy can also be used as a tool for successful ignition and to aid flame enhancement at preferred locations. There are few studies on feed back control systems. Roy et al. used spark-induced breakdown spectroscopy (SIBS) to measure the local fuel-air concentration in the spark gap at the time of ignition under stratified-charge conditions [54]. Phuoc [55] used a laser-induced spark to measure the ignition and fuel-to-air ratio of CH₄-air and H₂-air combustible mixtures simultaneously. However, studies involving laser ignition and spectroscopy are limited to gas phase reacting flows. The characteristics of laser-induced breakdown and spectrum in two phase flow are totally different from those in the gas phase [51]. Understanding of the interaction between laser-induced breakdown and fuel spray is needed for laser ignition and quantitative measurement of fuel concentration. The questions below will be investigated.

- How do fuel droplets affect the formation and subsequent development of the breakdown?
- How does the breakdown develop into a flame kernel in the spray?
- What is the difference between the electron transition in the gas and

the fuel droplets from laser-induced breakdown?

- How does the spectrum change according to the fuel droplet characteristics such as size, distribution and number density?

We focused on the transition from laser-induced breakdown to flame kernel. In parallel with the laser ignition process, the characteristics of atomic and molecular signals from the spectrum were investigated for quantitative measurement of the fuel concentration and droplet characteristics. The following investigations were performed:

- Shadowgraph imaging was used to analyze the generation of plasma and the propagation of shockwaves in air and fuel spray.
- High-speed imaging was used to visualize the transient morphology of laser-induced air breakdown and spray ignitions.
- Spectroscopy was used to obtain the atomic and molecular signal from laser-induced breakdown in air and fuel spray.
- The probability density function was used for analysis of the atomic and molecular signals from laser-induced breakdown of the fuel droplet, which can provide the relation between the droplet characteristics and the LIBS signals.
- The calibration curve of the LIBS signal was obtained for quantitative measurement of the equivalence ratio and the

characteristics of the fuel droplet in parallel with laser ignition.

Simultaneous laser ignition with spectroscopy is a scheme that enables rapid determination of the local equivalence ratio and the condensed fuel concentration during a reaction. This is a desirable scheme since such real time information onboard an SI engine for instance can be constantly monitored and fed back to the control loop to improve the mixing process and minimize emission of unwanted species and combustion instability, preventing the degradation of vehicle performance.

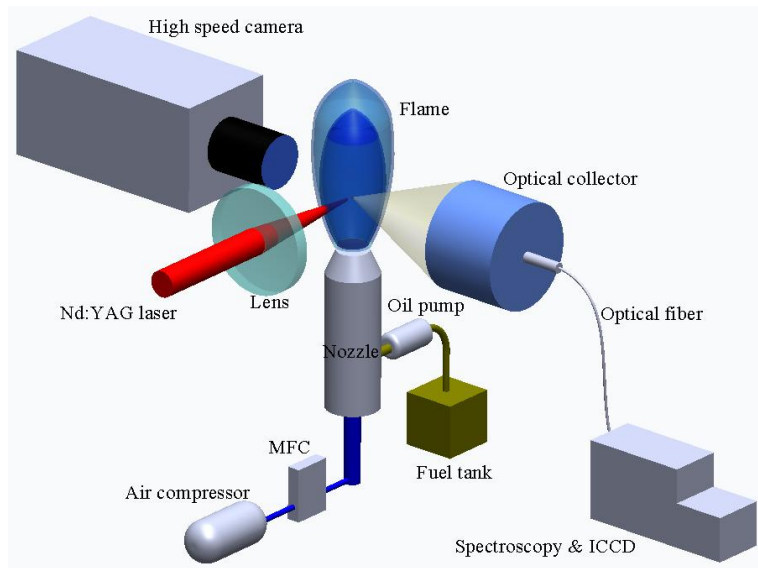
In addition, the compact design of the system allows for a small sized single pulsed laser to be used for both pulsed ignition and breakdown spectroscopy. Laser technology has advanced significantly: compact diode-pumped solid-state (DPSS) laser or compact fiber laser, and broadband spectroscopy can meet such compact and low-power requirements for realtime diagnostics of the scram combustor. Minimization of the system size is possible for potential onboard feedback control. In essence, the use of one small laser for both ignition and realtime diagnostics represents the key strength of the proposed scheme.

4.2 Experimental condition

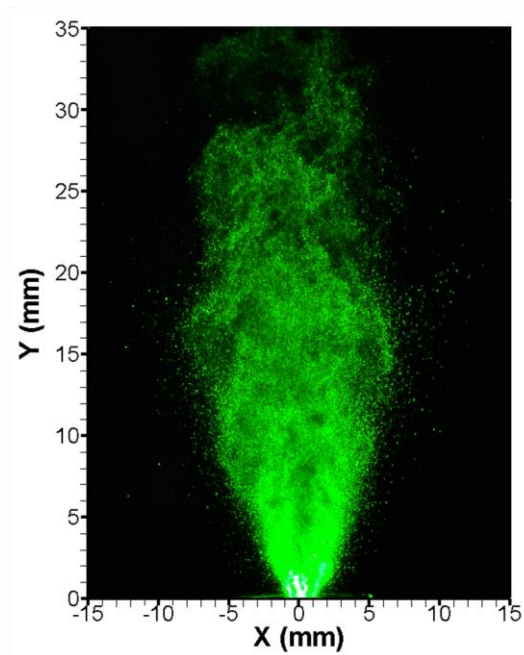
Figure 4.1(a) shows the experimental setup for the laser ignition and laser-induced breakdown spectroscopy while 4.1 (b) shows a scattering image of the spray. A spray of gasoline droplets were mixed with air at the nozzle tip. The spray nozzle was a Delavan SN 30609-2 air-assisted siphon nozzle. The fuel was directed to the nozzle through a pipe inside the flow channel. A second pipe supplied the nozzle with an atomization air flow, which impacted the fuel jet just before the nozzle exit. The droplet diameter distribution was between 20 and 50 μm at the nozzle exit. The fuel was a commercial gasoline obtained from the local gas station. The fuel flow rate was fixed to 10 ml/min by the oil pump. Compressed air was injected into the nozzle through a MFC (Mass Flow Controller). The air flow rate was 10 l/min and the equivalence ratio at the nozzle exit was 8.9.

For laser ignition and diagnostics, a Nd:YAG laser (continuum, Surelite I) at a wavelength of 1064 nm and 5 ns pulse duration was used. The beam was focused through a 100 mm convex lens with 100 mJ laser energy to generate the plasma. For visualization of the plasma and flame kernel, a high speed camera (Phantom v711) was arranged perpendicular to the laser beam path and used to observe the breakdown from a sideways perspective as shown in Fig. 4.1 (a). It provided broadband luminosity images at a sustained repetition rate of 390 kHz, an exposure time of 2 μs and a resolution of 128 x 64 pixels. The field of view was determined to be 20.9 x 10.5 mm with a calibration

target. The plasma light was collected by a quartz lens with a 100 mm focal length, which was perpendicular to the direction of the laser used for the laser-induced plasma spectroscopy. The collected plasma light was sent to an echelle spectrometer (Andor Mechelle 5000) with 0.1 nm resolution and an ICCD camera (Andor iStar) to record the signal. The delay time and ICCD exposure time were 1 μ s and 50 μ s, respectively. Several peaks (H : 656 nm, O : 777 nm, C₂ : 516 nm) were selected for analysis of the spray. The shadowgraph method was used to obtain the droplet size and distribution with high magnification. The droplet size and number density were obtained by processing the shadowgraph images. The plasma volume was also evaluated by the same shadowgraph technique.



(a)



(b)

Fig. 4.1 (a) Experimental setup, (b) scattering image of the droplet

4.3 Results

First, the laser induced plasma was generated in a uniform droplet stream with varied parameters such as laser energy and droplet size in a special test setup. Uniform droplets were generated by a nebulizer and sent to the Bunsen type burner. An ultrasonic nebulizer was used to atomize the liquid fuel injected from a vibrating ceramic plate at 1.65 MHz frequency and a rate of 3 mL/min by a syringe pump. Tiny gasoline droplets were generated by the nebulizer and sent to the air drying channel. The size of the droplets changed in the drying channel with control of the air flow rate. The Reynolds number varied from 500 to 2500 and the velocity varied from 0.5 m/s to 4 m/s. Figure 4.2 shows the threshold energy for breakdown according to the droplet size in the droplet stream. The threshold laser energy decayed with increasing droplet size. This is because more laser energy was absorbed by the droplets as the droplet diameters increased. The threshold energy was about 3 mJ at approximately 11 μm droplet diameter. The spot diameter was about 858.2 μm at the focal point. The irradiance was 0.103 GW/cm^2 at 3 mJ laser energy for the 11 μm droplet diameter.

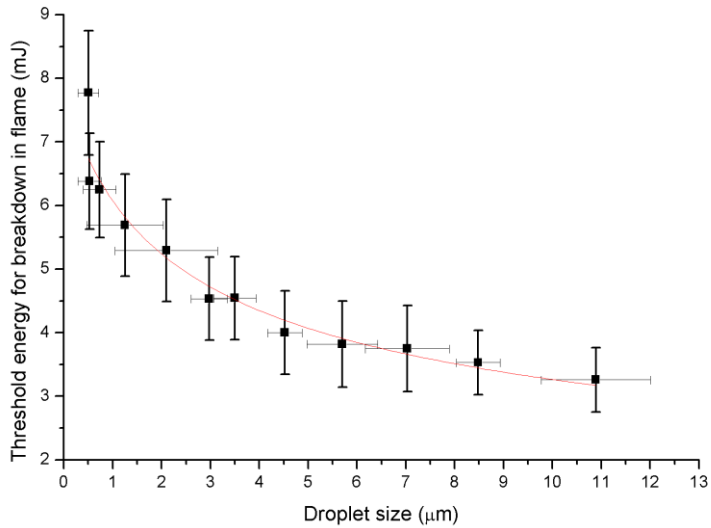


Fig. 4.2 Threshold energy for breakdown in the spray according to droplet size in the droplet stream

When the laser was focused on the air and gasoline droplet stream, a totally different type of plasma was generated for each medium. The shadowgraph method was used to visualize the plasma and shock wave shortly ($\sim 1\mu\text{s}$) after the laser pulse. Figure 4.3 shows plasma images at four different times (250 ns, 500 ns, 750 ns and 1000 ns) in the air and in the gasoline uniform droplet stream at 100 mJ laser energy shortly ($\sim 1\mu\text{s}$) after the laser pulse. The laser was irradiated from the right side to the left side in the images. The laser-induced plasma in the air and the gasoline droplet stream generated a shock wave that propagated along the radial and vertical direction. The shape of the plasma and shock waves generated in the air and the gasoline droplet stream were different, with longer radial length for the gasoline droplet stream

compared to the air.

Figure 4.4 (a) shows the displacement of the plasma and shock wave along the radial direction and the vertical direction in the air and in the gasoline droplet stream. The displacement along the radial direction is higher than along the vertical direction in both the air and the gasoline droplet stream. Breakdown begins at a location slightly before the focal point of the lens toward the incoming laser beam in the air [7] but occurs within the path of the laser beam in the gasoline droplet stream since the threshold energy for breakdown in the gasoline droplet is lower than in air as shown in Fig. 2(a) [56]. So the displacement along the radial direction in the gasoline droplet stream is higher than in the air. The displacement along the vertical direction in the air and in the gasoline droplet stream is almost similar.

Figure 4.4 (b) shows the velocity of the plasma and the shock wave along the radial direction and the vertical direction in the air and in the gasoline droplet stream. The velocity is obtained from the fitting curve of the displacement in Fig. 4.4 (a). The velocity along the radial direction in both the air and gasoline droplet stream is faster than along the vertical direction. The velocity of the plasma and the shockwave in the gasoline droplet stream along the radial direction is about 2 times faster than in the air at the early stage (< 10 ns). This high difference originates from the laser energy absorption and ignition of gasoline fuel. The gasoline droplets absorb laser energy along the path of the beam and the generated plasma propagates toward the incoming

laser beam. Hence, asymmetric plasma is generated and may affect the shape of the flame kernel at the early stage. These ignition characteristics are only found in the two phase fuel [46]. The velocity in both the air and the gasoline droplet stream become the same after about $1 \mu\text{s}$ because the plasma disappears within $1 \mu\text{s}$.

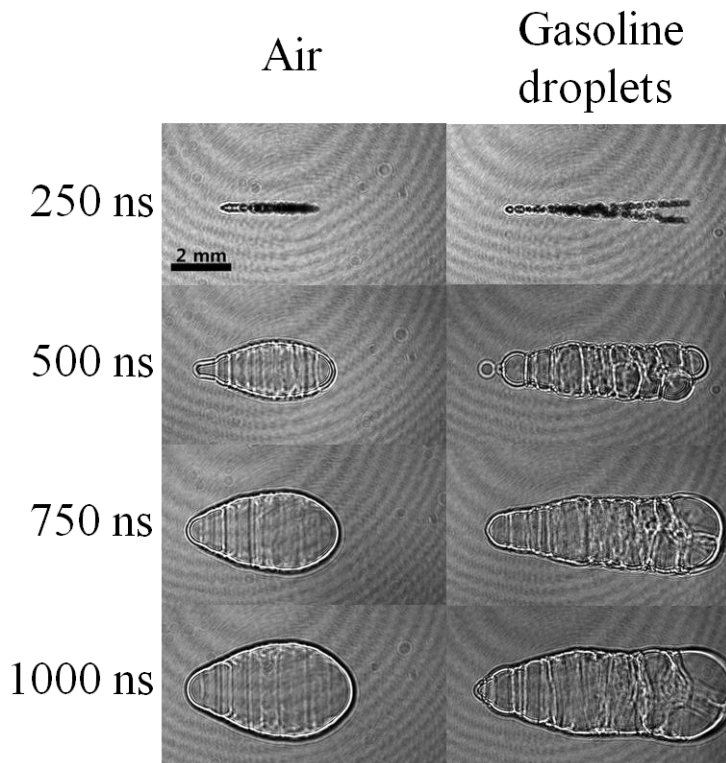
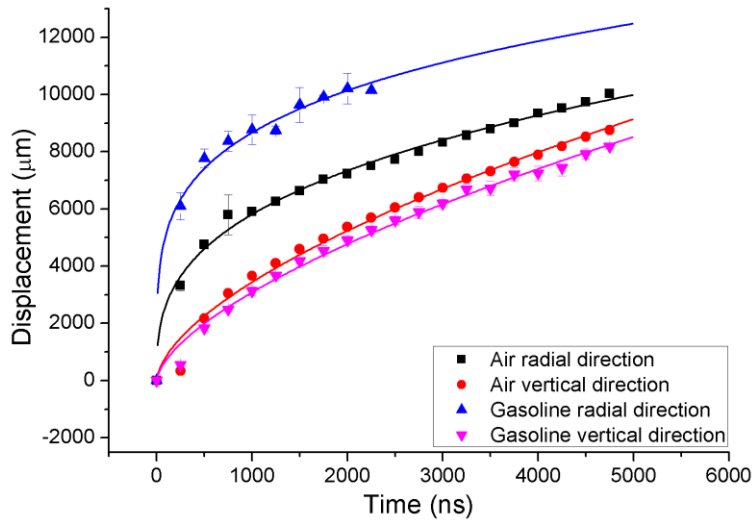
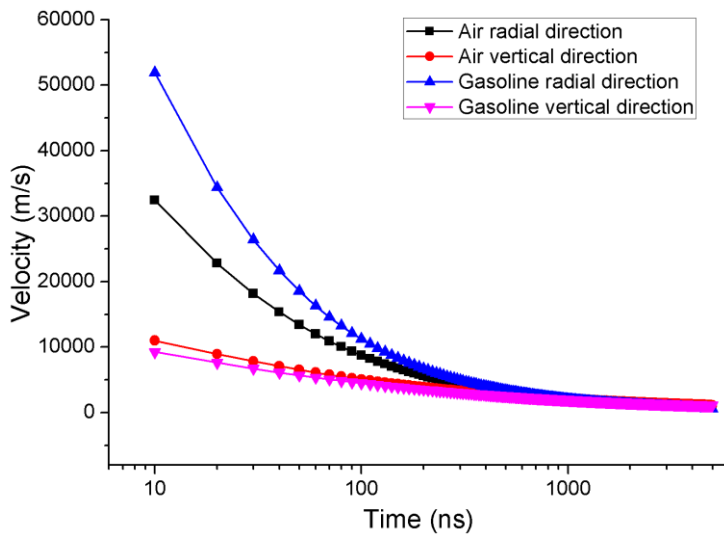


Fig. 4.3 Plasma images at four different times (250 ns, 500 ns, 750 ns and 1000 ns) in air and gasoline droplet stream



(a)



(b)

Fig. 4.4 Radial and vertical displacement of plasma (b) radial and vertical velocity of plasma in air and gasoline droplet stream

Figure 4.5 shows the sequences for the temporal development of laser-induced air breakdown and gasoline spray ignition. All images in the sequence are averages of the recordings from five individual breakdowns using in-house matlab code. The raw image was converted to an emission intensity contour for comparison of air and spray. The focal point in air and spray was at the (0,0) position and the laser was irradiated from the right side to the left. The breakdown was initiated at a location slightly before the focal point of the lens, in the region with the highest emission propagating toward the incoming laser beam. First, the air breakdown gradually adopted a bimodal appearance. This effect is explained by some references [7, 57]. The emission of air breakdown disappeared after about 50 μs . The second column in Fig. 4.5 shows average images of the spray ignition. The third row shows three lobes along the path of the laser beam before the focal point in the spray ignition. The first and second lobes resulted from local breakdowns initiated by fuel droplets. The third lobe resulted from a cluster of small breakdowns. This effect was also observed by Kawahara et al. [56] and is caused by droplets acting as micro-lenses. The emission intensity of lobes in the spray is higher than in the air, since the laser is absorbed by the fuel droplets. The three lobes became blurred and fibrous after 7.8 μs in spray. The transition from plasma to a flame kernel was observed at this time. The emission intensity was observed at about 100 μs . This observation is in agreement with an existing paper [51].

Figure 4.6 shows the mean intensity of high speed images for air breakdown and spray ignition. The emission intensity was averaged for 5 individual images. The emission intensity of air breakdown decreased rapidly within 10 μs . Afterwards, the intensity decreased slowly and approached the detection limit after about 30 μs , which is in agreement with the above mentioned study [51]. The intensity for spray ignition decays exponentially over time. The intensity of plasma light decreases rapidly and the transition from plasma to a flame kernel occurs. Chemiluminescence is generated in the flame kernel from combustion radicals. So, the emission intensity of the spray ignition lasts for 150 μs . This tendency is similar to published results [51], but the transition from plasma to flame kernel with gasoline droplets was observed for the first time in this study. The size of the gasoline fuel droplet easily decreases due to the high volatility of the fuel. So, the emission intensity is high in the initial flame kernel and is maintained for a long time due to the high ignitability of gasoline fuel.

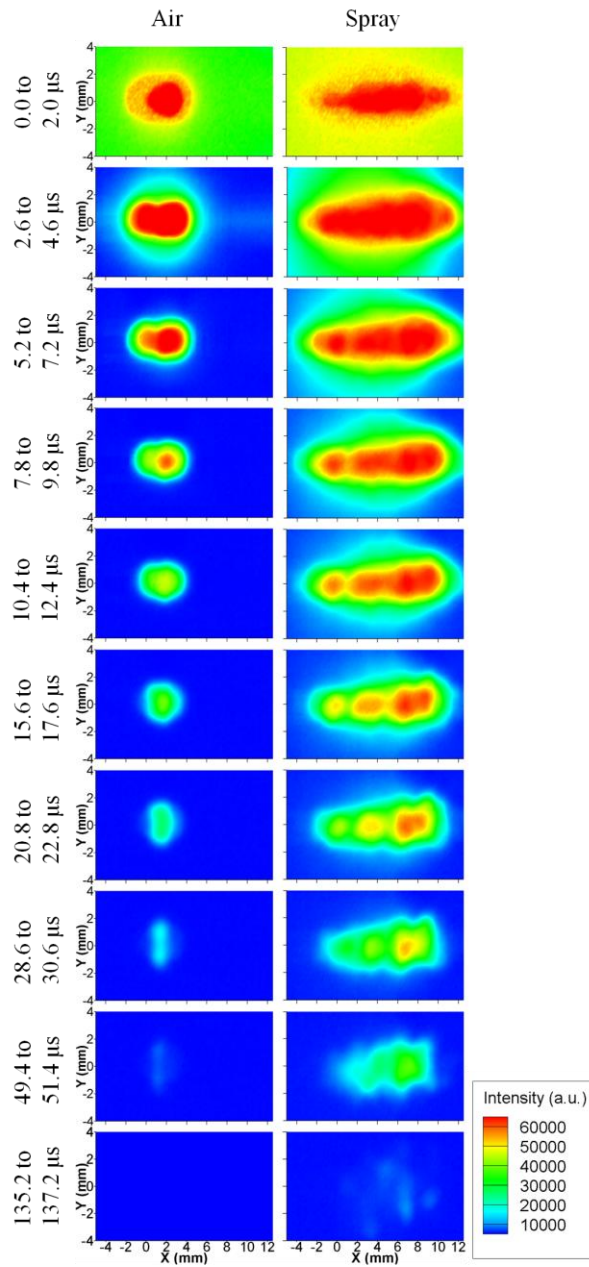


Fig. 4.5 Sequences of the temporal development of laser-induced air breakdown (left column) and gasoline spray ignitions (right columns)

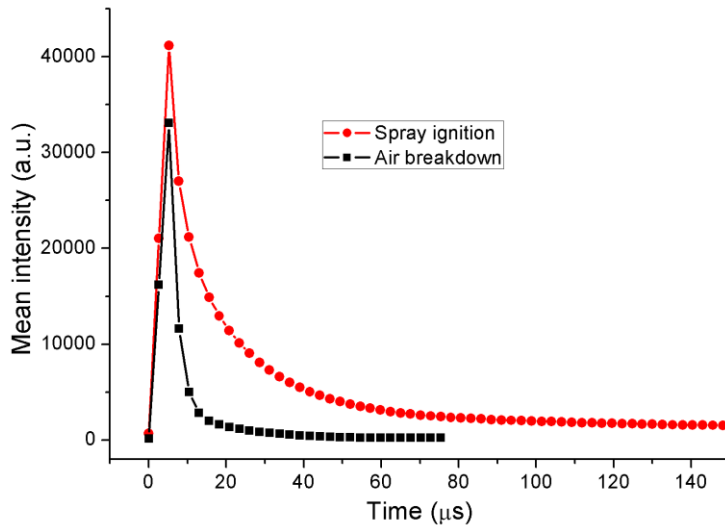
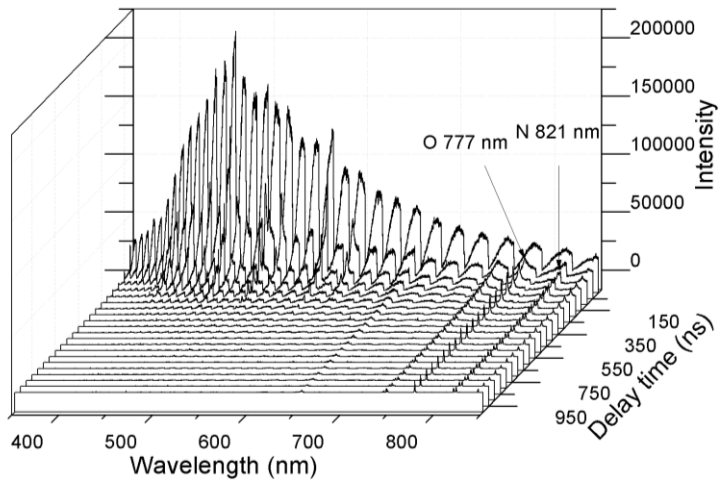
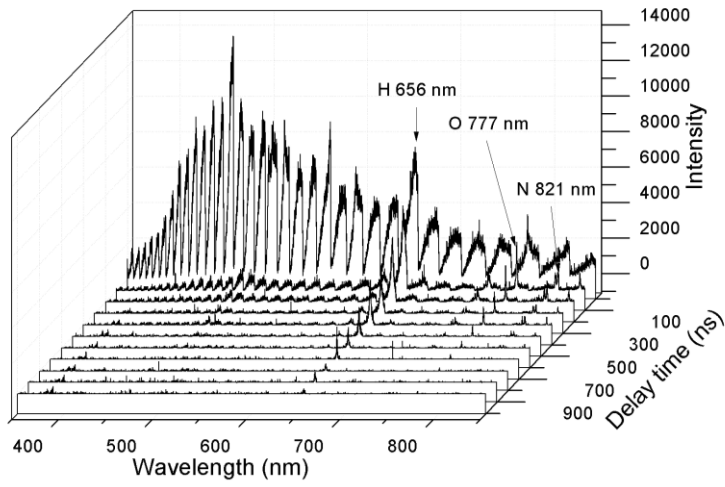


Fig. 4.6 The mean intensity of high speed images for air breakdown and spray ignition

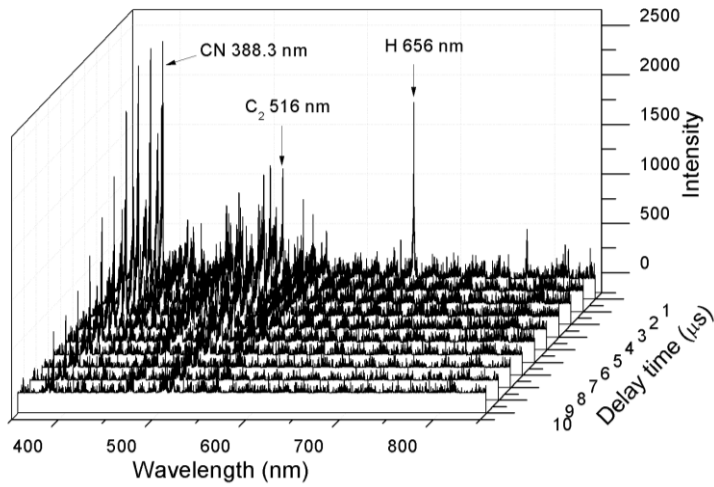


(a)

Fig. 4.7 Ensemble of the LIBS spectra according to the delay time in (a) air, (b) spray at early time ($\sim 1 \mu\text{s}$) and (c) spray after $1 \mu\text{s}$ (continue)



(b)



(c)

Fig. 4.7 Ensemble of the LIBS spectra according to the delay time in (a) air, (b) spray at early time ($\sim 1 \mu\text{s}$) and (c) spray after 1 μs

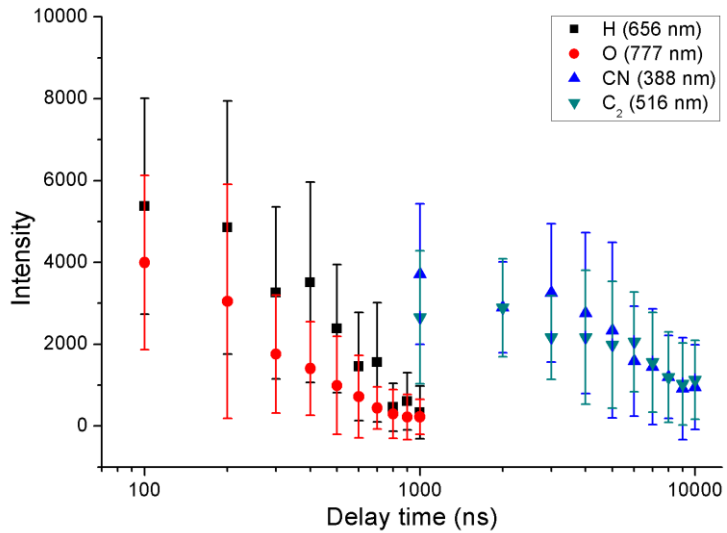


Fig. 4.8 The maximum intensities of the atomic signals (H and O) until 1 μ s delay time and the molecular signals (CN and C₂) until 10 μ s in the spray

In parallel with laser ignition, spectroscopic analysis of the breakdown in air and spray was conducted to measure the fuel concentration. Figures 4.7 (a), (b) and (c) show the ensemble of the LIBS spectra in air, in spray at an early stage ($\sim 1\mu$ s) and in spray after 1 μ s, respectively. An exposure time of 50 ns was used to capture the emissions from air breakdown in Fig 4.7 (a). For spray ignition, an exposure time of 100 ns was used for 1 μ s in Fig. 4.7 (b) and a 1 μ s exposure time was used from 1 to 10 μ s in Fig. 4.7 (c). The spectra show a strong continuum background until 30 ns for the air breakdown. O (777 nm) and N (821 nm) signals appeared at 200 ns after the laser pulse due to a decrease in the strong continuum background. The continuum

background in spray decreased more rapidly than in air as shown in Fig. 4.7 (b). So the H, O and N signals appeared very quickly (less than 100 ns) after the laser pulse. The H and O signals were from the gasoline fuel and air, respectively. These atomic signals decreased rapidly within 1 μs and molecular signals such as CN and C_2 appeared 1 μs after the laser pulse in Fig. 4.7 (c). These molecular signals originate from recombination between the ionized atoms during the plasma cooling process. This tendency has already been reported [58]. The CN and C_2 signals were used to determine the carbon contents in the unknown material with LIBS [59]. Figure 8 shows the the maximum intensities of the atomic signals (H and O) until 1 μs and for the molecular signals (CN and C_2) until 10 μs in the spray ignition. Atomic signals were obtained with 100 ns exposure while molecular signals were obtained with 1 μs exposure. Atomic signals rapidly decreased with increasing delay and molecular signals increased with increasing delay up to about 2 μs due to molecular recombination during plasma cooling. After 2 μs , the molecular signals decreased slowly, which is in agreement with an existing paper [58]. The time scale for LIBS measurement in spray was determined using these results.

The dispersion of fuel droplets in sprays is highly stochastic. Therefore, the LIBS signal intensity in spray changes randomly according to the droplet characteristics. Figure 4.9 shows the schematics of the length scale during LIBS measurement of the fuel droplet. The plasma volume was 0.0108 mm^3

and the gap between droplets was 19 μm in our study, which were obtained using the shadow graph method. Also, the size of the LIBS measurement position was 1.2 μm , which was determined using the collecting optics and several fuel droplets were included in the plasma volume at the measuring time. The LIBS signal depends on the presence of fuel droplets at the measurement position as shown in fig. 4.9. When the focused laser beam is irradiated onto the spray, the probability of a droplet at a specific position depends on the droplet size and the number density. If a droplet exists at the measurement position, the density at the measurement position is much higher than without a droplet. The density is related to the plasma intensity, which is proportional to the LIBS base intensity. So, the probability of droplet existence at the measurement position can be determined using the LIBS base signal. Figure 4.10 (a) shows the laser induced plasma spectra for the C_2 signal at a height of 10 mm in spray for different base intensities (low, middle and high). Figure 4.10 (b) shows the laser induced plasma spectra for H and O signals at a height of 10 mm in spray for different base intensities (low, middle and high). The base intensity was averaged from 320 nm to 350 nm. Differences were observed in the spectra even when the laser was irradiated at the same position. The base intensity increased if a fuel droplet was present at the measurement position. Also, the C_2 signal in the presence of a droplet (high base intensity) was about 5 times higher than in the absence of a droplet (low base intensity) as shown in Fig. 4.10 (a). The C_2 signal is usually used

for the measurement of soot [60]. However, the C_2 signal in this study came from the gasoline droplet since there was no soot at the measurement positions. When the laser was irradiated on the gasoline droplet, fragmentation of the droplet occurred, resulting in the C_2 signal [59]. On the other hand, the difference in H intensity in the presence or absence of a droplet was much lower than the difference in the C_2 signal intensity as shown in Fig. 4.10 (b). Also, the difference in O intensity in the presence or absence of a droplet is very low. This means that the H and O signals were barely related to the existence of a droplet.

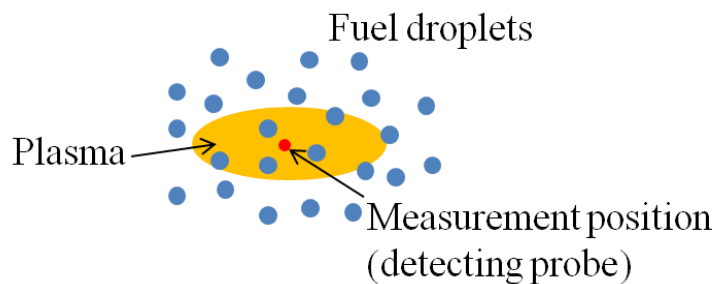
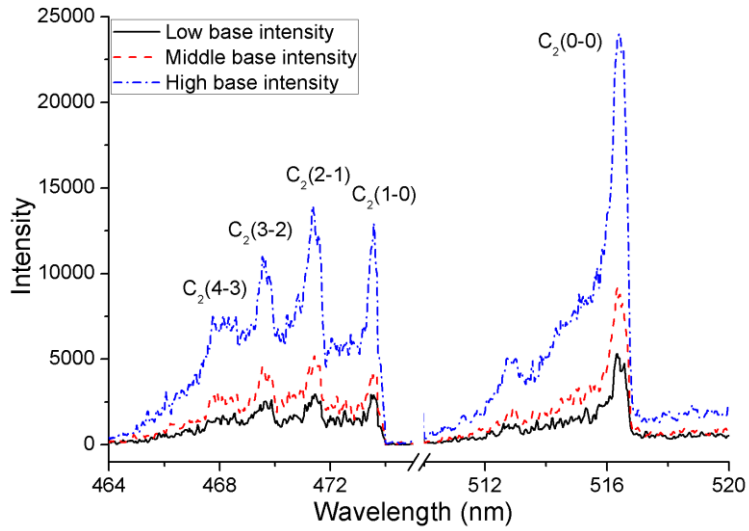
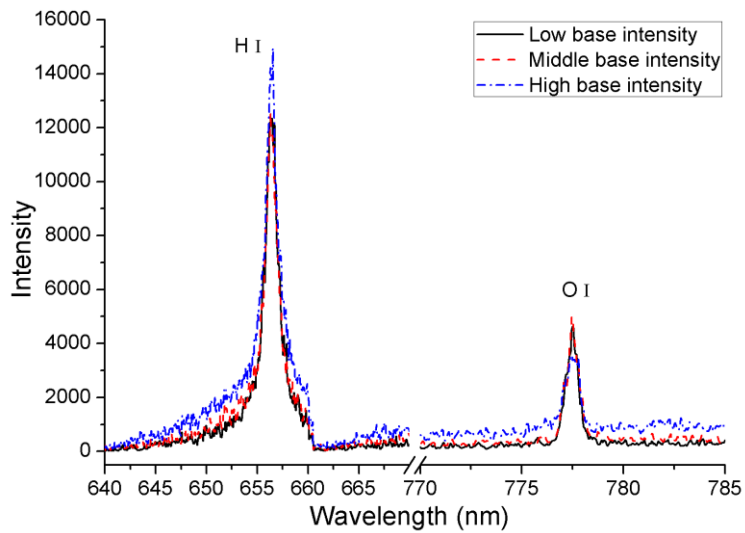


Fig. 4.9 schematics of LIBS measurement in fuel droplets

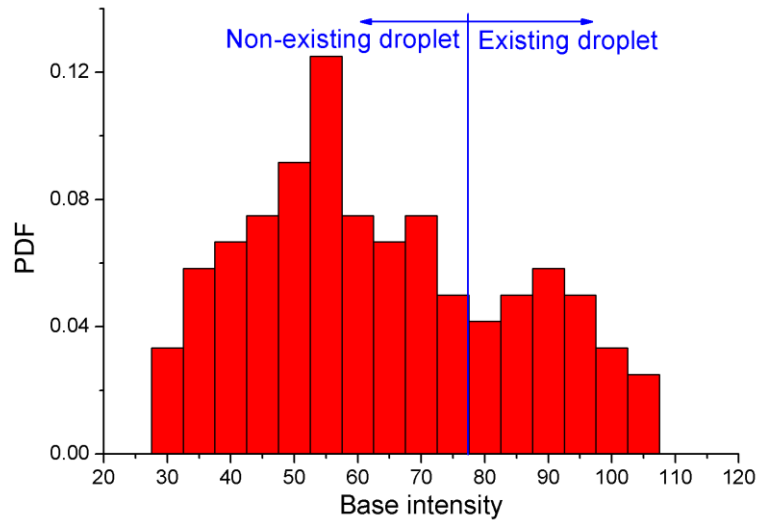


(a)

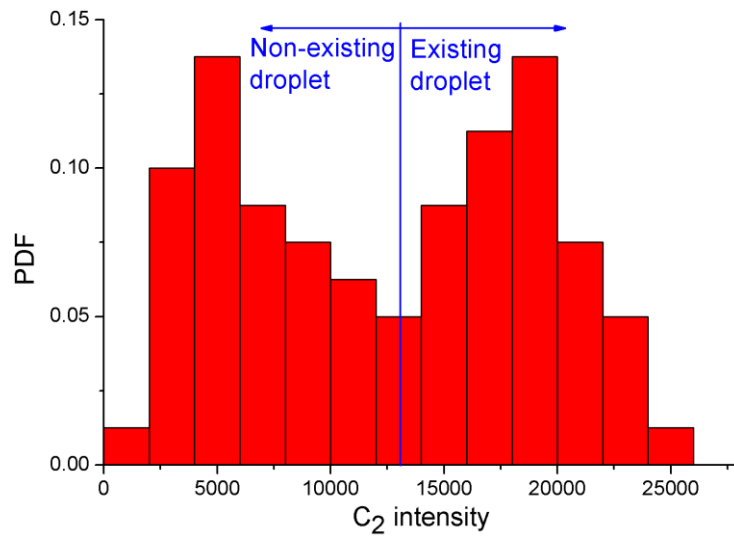


(b)

Fig. 4.10 (a) C₂ spectra, (b) H, O spectra at 10 mm height in spray for different base intensity schematics of LIBS measurement in fuel droplets

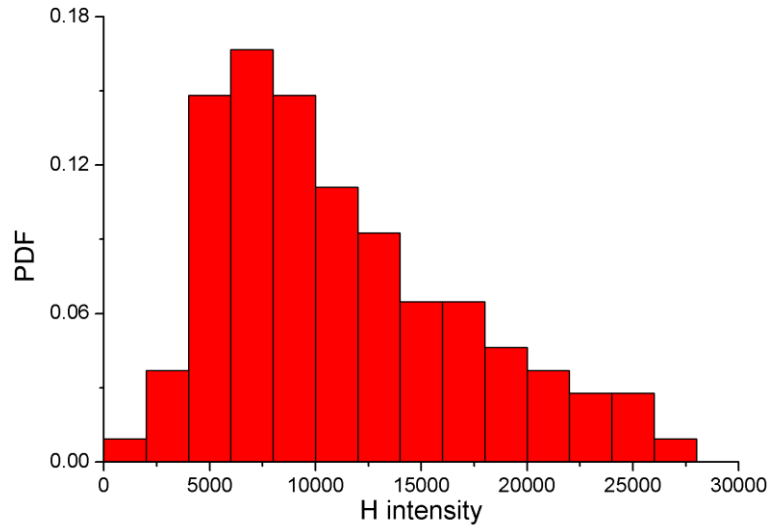


(a)

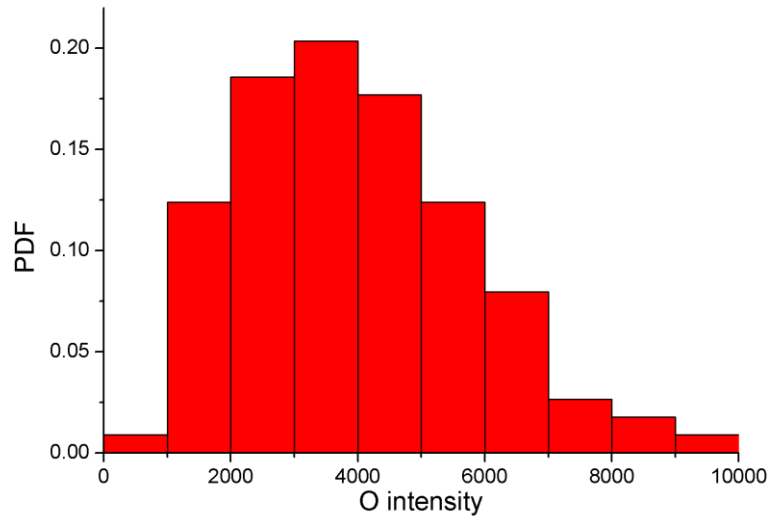


(b)

Fig. 4.11 Probability density function of (a) the base intensity, (b) C_2 intensity, (c) H intensity and (d) O intensity (continue)



(c)



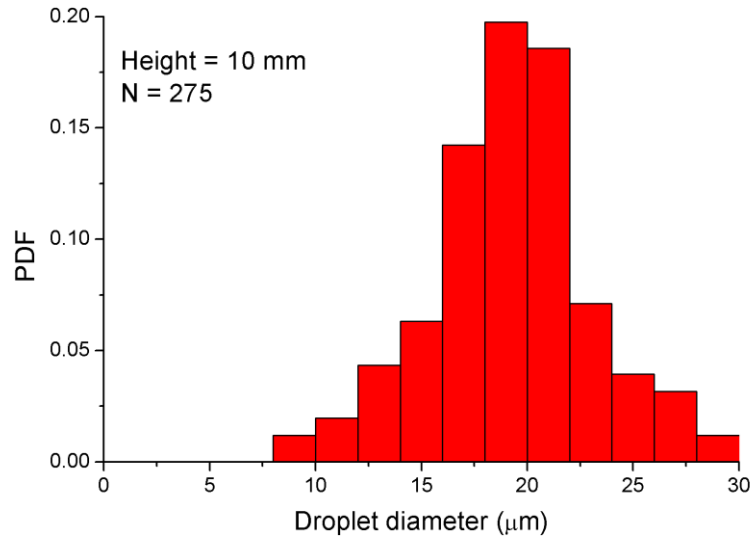
(d)

Fig. 4.11 Probability density function of (a) the base intensity, (b) C_2 intensity, (c) H intensity and (d) O intensity

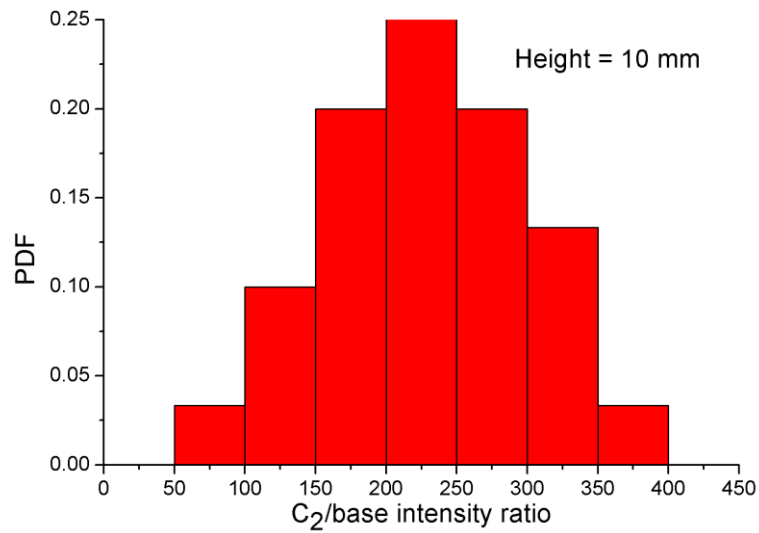
Figure 4.11 (a) and (b) show the probability density function (PDF) of the base intensity and the C_2 (516 nm) intensity at a height of 10 mm in spray, respectively. There are two peaks in Fig. 4.11 (a) and (b); the left peak was obtained in the absence of a droplet and the other was in the presence of a droplet. A fuel droplet may be present when the laser is focused on the spray. When a fuel droplet was present at the measurement position, the base and C_2 signal intensities increased. So, we know that the C_2 signal is strongly related with the existence of a droplet in spray. The C_2 signal originates from the liquid phase fuel. The high value of the second peak in the PDF of C_2 intensity indicates that the droplet is more likely to be present than absent. The second peak in the PDF of C_2 intensity is related to the number density and the C_2 signal increased with increasing droplet size. Therefore, we could obtain liquid phase fuel information such as concentration, droplet size and number density, which are very important in spray flame. On the other hand, the PDF for H (656 nm) and O (777 nm) signals had only one peak in Fig. 4.11 (c) and (d). H and O signals were barely affected by the existence of a droplet.

We found that the C_2 signal was related to the size of the droplet and the number density in spray. Therefore, the relation between the droplet characteristics (size and number density) and the LIBS signals was investigated using PDF analysis. Figures 4.12 (a) and (b) show the PDF of the droplet diameter and that of the C_2 /base intensity ratio from laser induced

plasma at a height of 10 mm, respectively. The C_2 /base ratio can provide the liquid phase fuel concentration regardless of droplet existence. Also, normalization to the base signal can reduce measurement errors such as fluctuation of laser energy. Figure 4.12 (c) and (d) show the probability density function of the droplet diameter and that of the C_2 /base intensity ratio from laser induced plasma at a height of 15 mm, respectively. Figure 4.12 (e) and (f) show the probability density function of the droplet diameter and that of the C_2 /base intensity ratio from laser induced plasma at a height of 20 mm, respectively. The number density of the droplets in plasma volume was 275, 267 and 209 at 10 mm, 15 mm and 20 mm, respectively. The droplet diameter decreased with increasing height in Fig. 4.12 (a), (c) and (e) and the C_2 /base ratio also decreased with increasing height in Fig. 4.12 (b), (d) and (f). The droplet diameter and the C_2 /base intensity ratio have a Gaussian distribution, indicating that the C_2 /base ratio is related to the droplet diameter. When the laser is focused on a droplet, the C_2 /base ratio is proportional to the droplet size. So, if we know the droplet size or number density, we can obtain information about the droplet size or number density by measuring the C_2 signal. When the laser induced plasma is generated, the droplet in the constant plasma volume evaporates completely due to the high laser energy.

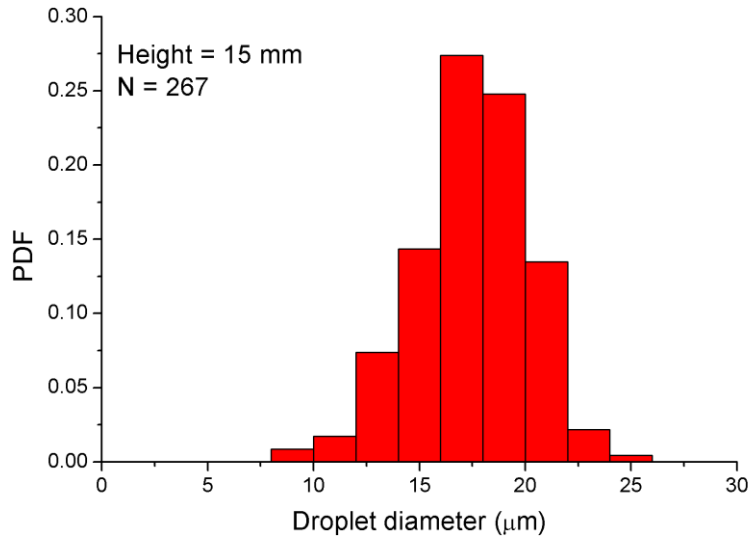


(a)

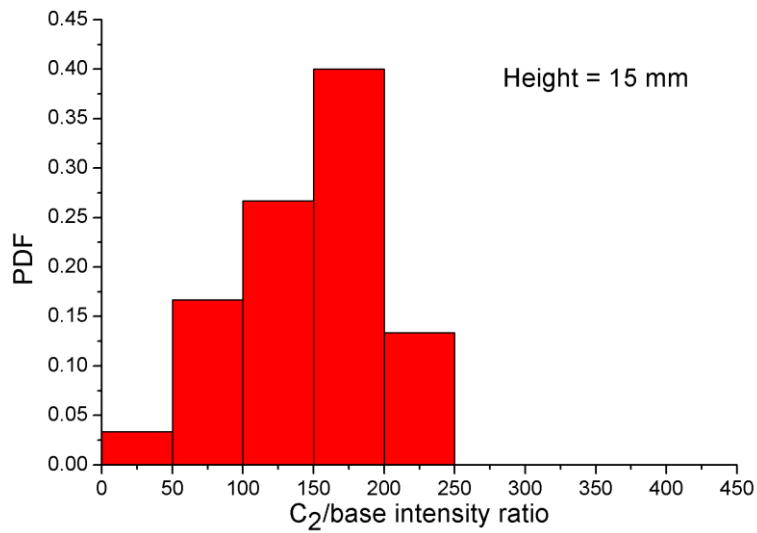


(b)

Fig. 4.12 (a) PDF of the droplet diameter for different height (a)10 mm, (c) 15 mm and (e) 20 mm, PDF of the C_2 /base intensity ratio for different heights (b) 10 mm, (d) 15 mm and (f) 20 mm (continue)

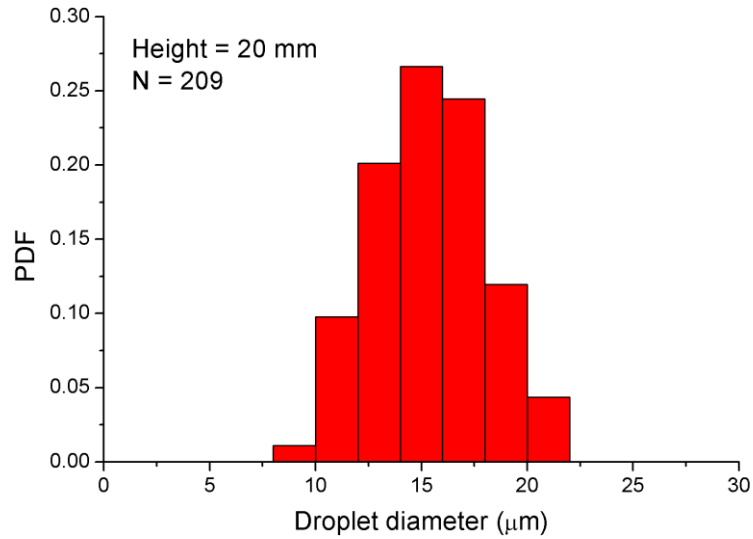


(c)

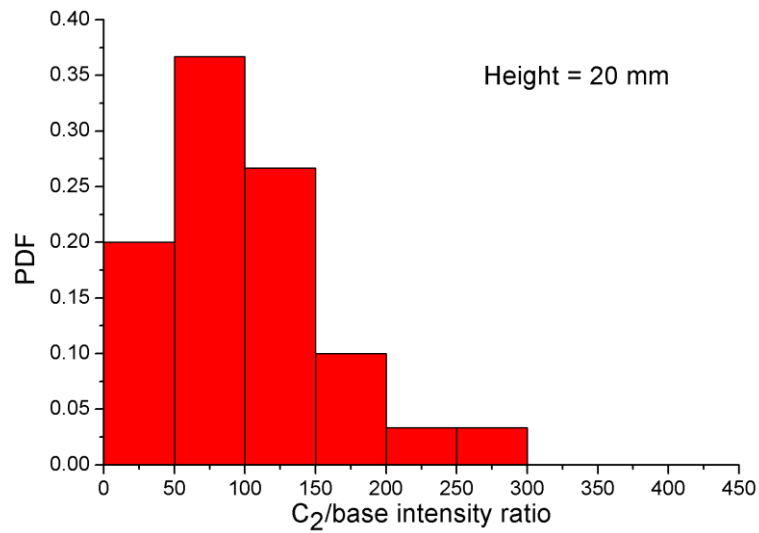


(d)

Fig. 4.12 (a) PDF of the droplet diameter for different height (a)10 mm, (c) 15 mm and (e) 20 mm, PDF of the C_2 /base intensity ratio for different heights (b) 10 mm, (d) 15 mm and (f) 20 mm (continue)



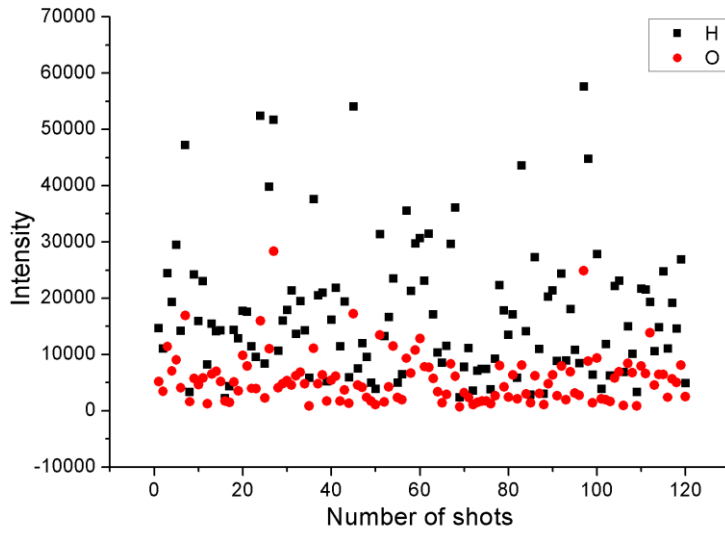
(e)



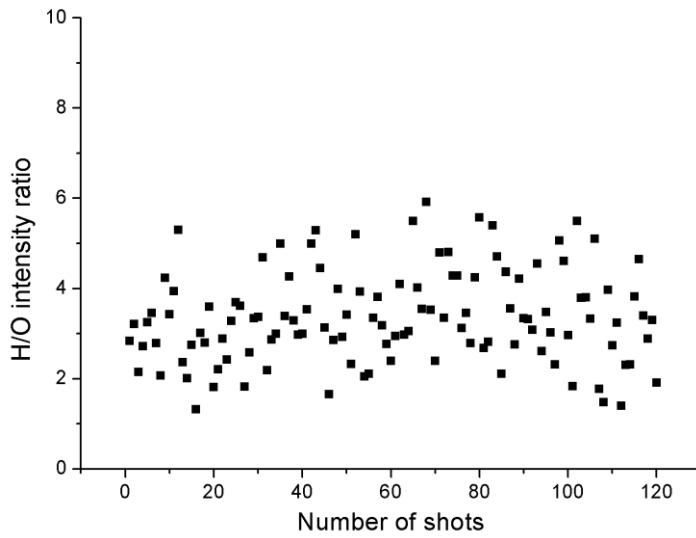
(f)

Fig. 4.12 (a) PDF of the droplet diameter for different height (a)10 mm, (c) 15 mm and (e) 20 mm, PDF of the C_2 /base intensity ratio for different heights (b) 10 mm, (d) 15 mm and (f) 20 mm

The shot-to-shot signal fluctuation of the LIBS signal in spray was evaluated for instantaneous fuel concentration measurement. Figure 4.13 (a), (b), (c) and (d) show the shot-to-shot signal fluctuations of atomic signals (H, O), H/O intensity ratio, C_2 and C_2 /base intensity ratio according to the number of shots, respectively. The LIBS signal is highly dependent on the laser energy. The uncertainty of the laser energy in our results was 3%. Also, in our previous research, the measurement uncertainty in the gas phase fuel was quite low (2% variation in reactants) [6]. Therefore, the fluctuation of the LIBS signal originated from the actual measurement value. As described above, the LIBS signal in spray is highly dependent on the existence of droplets at the measurement position. Thus, the high fluctuation of LIBS signal in Fig. 4.13 represents the droplet characteristics. Also, the fluctuation of H/O and C_2 /base ratios was lower than H, O and C_2 intensities. This is because the intensity ratios (H/O and C_2 /base) compensate for the uncertainty from the fluctuation of laser energy.

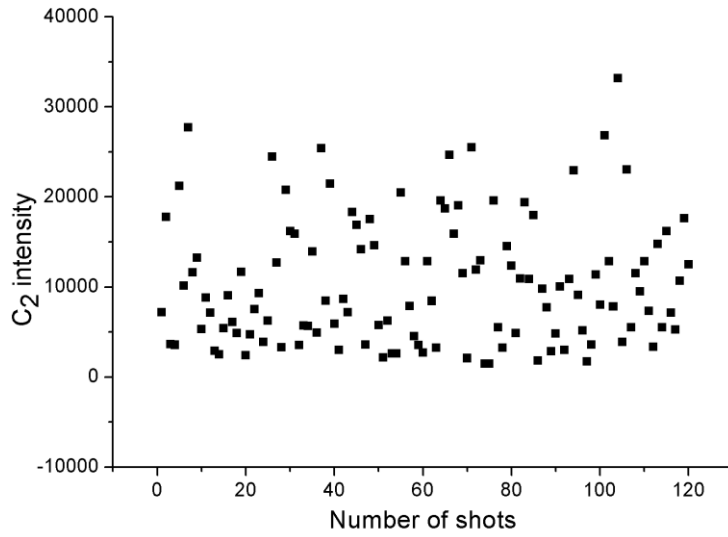


(a)

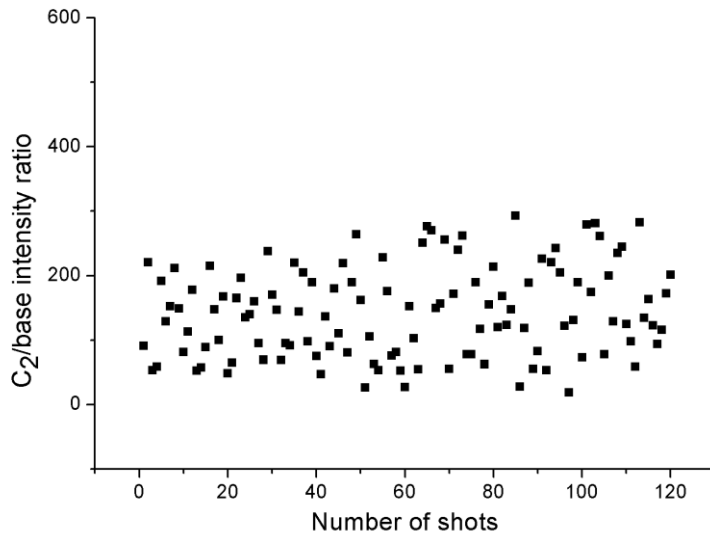


(b)

Fig. 4.13 Shot-to-shot fluctuation of (a) H and O intensities and (b) H/O intensity ratio, (c) C_2 intensity and (d) C_2 /base intensity ratio (continue)

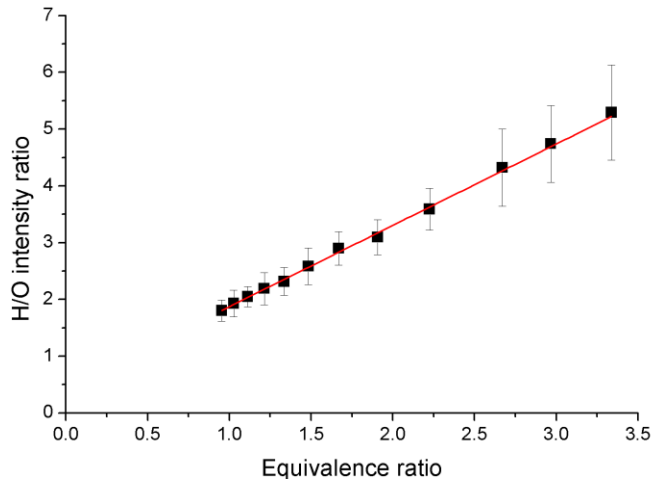


(c)

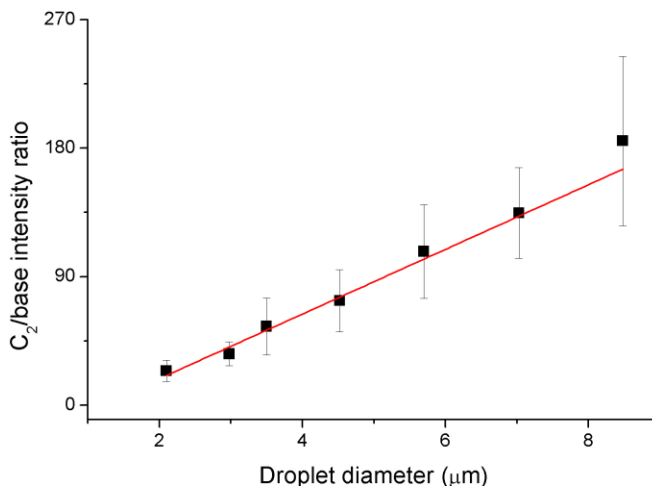


(d)

Fig. 4.13 Shot-to-shot fluctuation of (a) H and O intensities and (b) H/O intensity ratio, (c) C_2 intensity and (d) C_2 /base intensity ratio

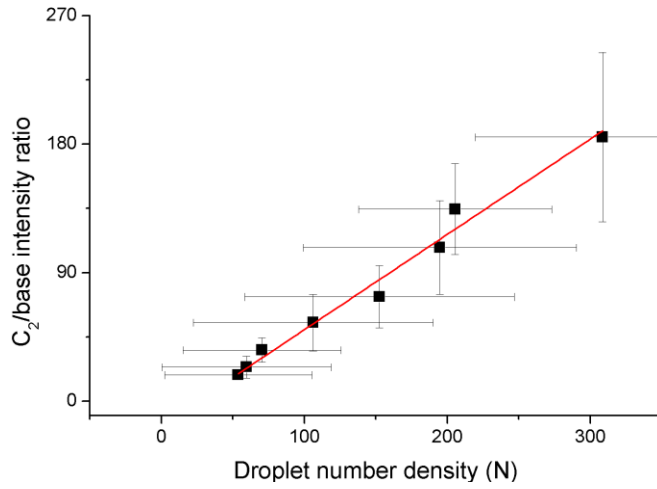


(a)

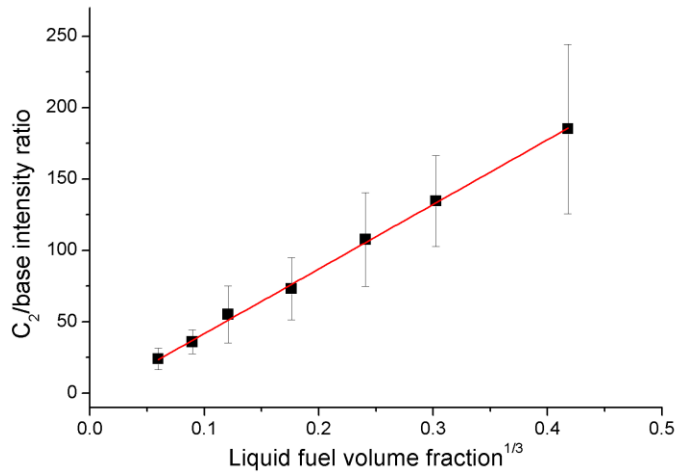


(b)

Fig. 4.14 Calibration curves (a) H/O ratio according to the equivalence ratio and (b) C₂/base intensity ratio according to the fuel droplet diameter (c) C₂/base intensity ratio according to the fuel droplet number density and (d) C₂/base intensity ratio according to the cube root of liquid fuel volume fraction (continue)



(c)



(d)

Fig. 4.14 Calibration curves (a) H/O ratio according to the equivalence ratio and (b) C₂/base intensity ratio according to the fuel droplet diameter (c) C₂/base intensity ratio according to the fuel droplet number density and (d) C₂/base intensity ratio according to the cube root of liquid fuel volume fraction

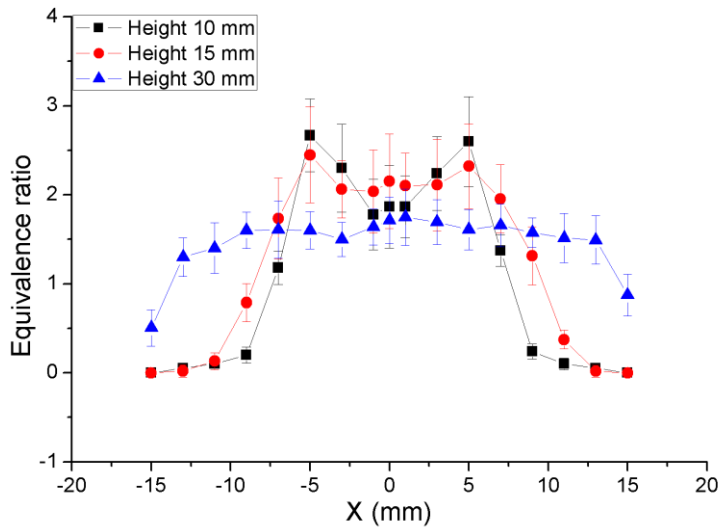
Quantitative analysis of the spray was conducted in a uniform droplet stream to obtain an equivalence ratio and liquid fuel concentration. Figure 4.14 (a) shows the H/O LIBS intensity ratio according to the equivalence ratio. The H/O intensity ratio was almost linear in accordance with the equivalence ratio. The H and O signals originated from the hydrocarbon fuel and air, respectively. Previous works have demonstrated that the H/O ratio is usually linear according to the equivalence ratio in gaseous fuel [5, 6, 26]. Though droplets exist in the flow, the H/O ratio remained linear according to the equivalence ratio in this study. Thus, we confirmed that the H/O intensity ratio could be used to obtain the equivalence ratio in the two-phase flow condition.

Figure 4.14 (b) and (c) show the C_2 /base intensity ratio according to the fuel droplet diameter and the C_2 /base LIBS intensity ratio according to the droplet number density in a uniform droplet stream, respectively. The C_2 /base ratio is almost linear according to the droplet diameter and the droplet number density. The fuel droplet volume was calculated from the droplet diameter obtained with the shadowgraph. Figure 4.14 (d) shows the C_2 /base intensity ratio according to the cube root of the liquid fuel volume fraction. The liquid fuel volume was obtained by multiplying the number density and the droplet volume. The liquid fuel volume was then divided by the constant plasma volume, which was 0.0108 mm³. Interestingly, the C_2 /base intensity ratio has a linear relation with the cube root of the liquid fuel volume fraction. In other words, the intensity (I) of the molecular band signal from laser induced

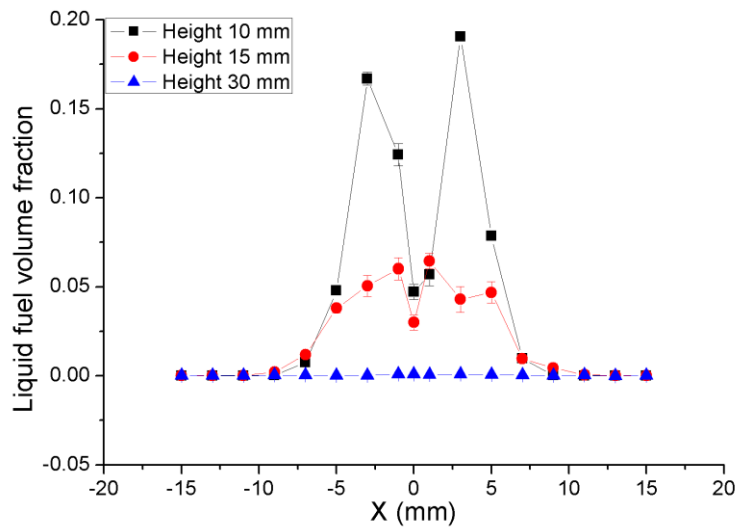
plasma is proportional to the cube root of the liquid fuel volume (V_{fuel}). This relation is defined as $I \propto (V_{\text{fuel}})^{1/3}$. This confirms that the equivalence ratio and the liquid fuel concentration can be obtained simultaneously from the laser induced plasma during ignition.

Figure 4.15 (a) and (b) show the equivalence ratio and liquid fuel volume fraction for three different heights along the radial direction for a spray. The calibration curves of the equivalence ratio and the liquid fuel volume fraction in Fig. 4.14 (a) and (d) were used to quantify the equivalence ratio and the fuel volume fraction, respectively. The equivalence ratio and the liquid fuel volume fraction were quite reasonable. The diffusion of the fuel along the radial direction is shown for different heights in Fig. 4.15 (a). The atomization and evaporation of the fuel droplet for different heights can be observed in Fig. 4.15 (b). The equivalence ratio and liquid fuel volume fraction are very important parameters in combustion. The equivalence ratio and droplet characteristics affect the ignition, extinction, stability behavior, combustion efficiency and pollutant emissions such as CO, soot, and NOx. These two parameters can be used to monitor fuel injection systems utilizing laser ignition. The proposed diagnostics technique using a single laser source for ignition and plasma emission spectroscopy is based on a simple yet powerful concept, designed as a feedback control system. Simultaneous laser ignition and spectroscopy is a scheme that enables rapid determination of the local

equivalence ratio and the condensed fuel concentration during a reaction. This is a desirable scheme since such real time information onboard an engine for instance can be constantly monitored and fed back to the control loop to improve the mixing process and minimize emissions of unwanted species and combustion instability, preventing a degradation of engine performance.



(a)



(b)

Fig. 4.15 (a) Equivalence ratios and (b) liquid fuel volume fraction along the radial direction for different heights (10 mm, 15 mm and 30 mm)

4.4 Conclusion

Simultaneous laser ignition and laser-induced plasma spectroscopy on a spray flame were employed to develop a feedback control system. The plasma characteristics were evaluated by visualization the spray. The plasma at the initial time ($\sim 1\mu\text{s}$) was visualized by shadow graphing. We found that the gasoline droplets absorbed the laser energy along the path of the beam and the generated plasma propagated toward the incoming laser beam. The transition from the plasma to the flame kernel in fuel spray was visualized by high speed imaging. The plasma emissions in the spray were replaced by a much weaker combustion chemiluminescence. Small breakdown along the laser beam path occurred in the spray due to a micro-lens effect from the fuel droplets. The intensity of the air breakdown decreased rapidly whereas the intensity of the spray breakdown decreased steadily, becoming invisible to the camera after $150\mu\text{s}$, which is 3 times slower than the air breakdown. For laser-induced breakdown spectroscopy, the probability density function of the LIBS signal was obtained to detect the fuel droplets in sprays, which are highly stochastic. We found that the C_2/base intensity ratio was highly related to the size and the number density of the fuel droplets. The H/O intensity ratio and C_2/base intensity ratio were used to obtain the equivalence ratio and the liquid fuel concentration in the spray, respectively. The shot-to-shot signal fluctuation in the spray is caused by the probability of droplet existence at the measurement position. The uncertainty of LIBS in the spray depends on the fluctuation of

laser energy (about 3%), which can be compensated using intensity ratios (H/O, C₂/base). The quantitative equivalence ratio and liquid fuel volume fraction were obtained from the laser irradiation, which also causes ignition in the spray. The present results suggest a fuel/air ratio feedback controller that uses a single laser source for both optical breakdown in spectroscopy and subsequent ignition of the two-phase spray. Therefore, a novel feedback control strategy for flame ignition and stabilization simultaneously with in-situ combustion flow diagnostics onboard was developed in the present study.

CHAPTER 5

DIAGNOSTIC OF TWO PHASE (SOLID PARTICLE-GAS) FLOW USING LIBS [61, 62]

5.1 Background and objective

The particulate matter (PM) emissions from aviation engines are getting increasing attention due to the suspected adverse impact on global climate change, local air quality, and human health [63, 64]. Aviation engines emit both nonvolatile (soot) PM as well as the volatile particulates. The particulate emissions evolve from being dominated by soot at the engine exit plane to a complex mixture of soot, sulfates and condensed organics as the exhaust stream cools and mixes with ambient air for very short time [65]. Also the engine exhaust is characterized by the high speed (~ 90 m/s) flow and the intense turbulent flow conditions. Thus the nature of aviation emissions makes it difficult to detect the particulates within a jet stream from a distanced location with an in-situ measurement technique.

Traditionally, PM from aviation is measured by the extractive methods [66]. The extractive sampling probes are inserted behind the engine exhaust, and PM is extracted at different distances from the engine. The extracted PM is analyzed by the aerosol analyzer such as CPC (Condensation Particle

Counter), SMPS (Scanning Mobility Particle Sizer) and DMA (Differential Mobility Analyzer). However these methods are not suitable for detection of the transitional evolution of PM. Another method for detecting PM is LII (Laser Induced Incandescence) [67, 68] which can detect remotely particle size and distribution using laser. The use of this method is limited to soot measurement only, and other chemical species such as sulfates or condensed organics cannot be detected.

The LIBS (laser induced breakdown spectroscopy) is based on the optical spectroscopy of laser induced plasma [69-72]. For aerosol analysis, many applications can be found in the fields of industrial exhausts [10, 11] or biological aerosols [12, 73]. An enhanced LIBS system is developed for simultaneous detection of particle size and the composition by the method of conditional analysis [74-76]. There are several reported studies along the line of detecting metallic aerosols. Zhang et al. [10] measured metallic aerosols such as Sb, As, Be using LIBS for developing continuous emission monitor (CEM) in an incinerator. Also Buckley et al. demonstrated the monitoring of continuous emissions using LIBS for toxic metals [11]. Fisher et al. analyzed the gating time for detecting toxic metals such as As, Be, Cd, Cr and Hg using LIBS [77]. Recently, Park et al. detected the ultrafine metallic aerosols (Al, Ca, Cd, Cr, Cu etc.) that have sub-micron sizes using LIBS [78].

On other note, the detection of carbon or carbon particulates receives important recognition in the field of combustion diagnostics and bio aerosol

detection. Vors and Salmon [79] showed measurements of glucose and NaHCO_3 using LIBS and confirmed similarity of the two detecting signals, where the limit of detection (LOD) of glucose and NaHCO_3 are found as $60 \mu\text{g}/\text{m}^3$ and $50 \mu\text{g}/\text{m}^3$, respectively. They choose carbon line (247.856 nm) for carbon detection and obtained the linear calibration curve for two different particle diameters of $3.7 \mu\text{m}$ and $4.6 \mu\text{m}$. Ferioli and Buckley [4, 5, 80] demonstrated that LIBS could measure the fuel equivalent ratio where they used ratio C/air signal and CN/air signal to measure the carbon quantity where the ratio showed linear relationship with fuel equivalence ratio.

When detecting carbonate particles, there is an ambiguity associated with distinguishing the origin of carbon peaks, whether they came from carbonate particulates or the gas. Recently, Asgill et al. [81] proposed a method to distinguish the origin between the gaseous and the particulate phases using a double-pulse and a single-pulse LIBS. In their work, the dual to single-pulse response ratio was shown to increase according to an increase in the percentage of gaseous carbons present. Furthermore, the detection using LIBS has shown useful in some challenging conditions such as in a supersonic flow and rocket engine combustion [29].

In our study, the feasibility of LIBS for detecting PM from a high speed jet engine exhaust is examined. The particulates detection using LIBS in high speed jet flow as oppose to gas particle measurement is reported in the present work for targeting carbon element. A lab-scale jet flow apparatus which

produces exhaust plume of aircraft engine is used in the experiment. Glucose is selected as a soot simulant of aviation emissions. By utilizing the LIBS signals, remote detection of carbon from the high speed exhaust flow is achieved.

5.2 Experimental condition

Figure 5.1 (a) shows experimental setup. An ultrasonic nebulizer was used to generate particles in the channel. 20 % glucose solution was fed at the rate of 2.07 mL/min to the vibrating ceramic plate of 1.65 MHz frequency. The glucose solution is made from de-ionized (DI) water and the glucose particles of 99.5 % purity. The vibrating ceramic plate can vaporize glucose solution up to 5.83 mL/min until the prepared solution is completely evaporated. Consequently the resulting feeding rate of glucose was 0.414 mL/min or 0.6375 g/min using 1.54 g/cm³ glucose density. Since the glucose has 40 wt. % of carbon per particle, pure carbon concentration rate is 0.255 g/min. The evaporated glucose solution was sent to the heated channel by air flow. The pure air stream was generated by the compressor which passed through a filter and valve, so that the air carrying glucose particle had 10 mL/min flow rate. The aqua glucose particles generated by vibrating ceramic were dried in the heating channel which had 150 C surface temperature. The dried glucose particles were sent to the test section with a jet flow. Then the air from

compressor was fed into the test section for controlling the glucose concentration and velocity by a valve. The pure air was delivered at the rate of 81 to 534 L/min. The nebulizer efficiency (ε) was defined by the ratio of output to the input quantity of glucose as

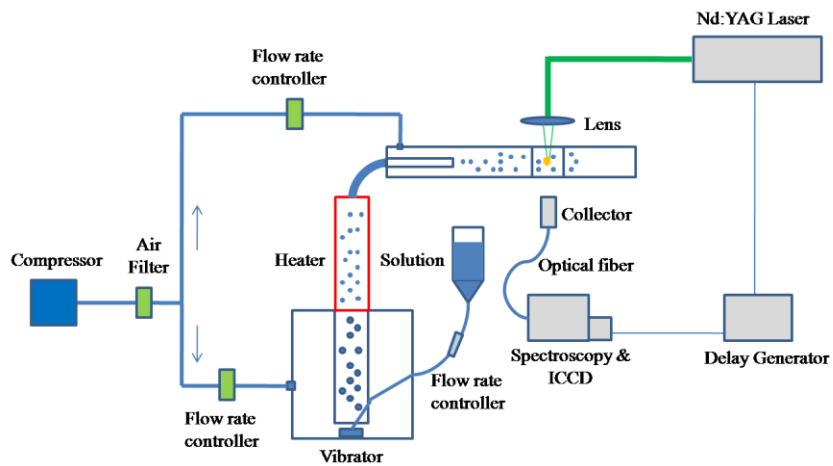
$$\varepsilon = \frac{q_{out}}{q_{in}} \quad (5.1)$$

where q_{out} and q_{in} are the output and the input mass flow rate of glucose, respectively. q_{in} was fixed by the current glucose feeding rate. To obtain q_{out} , the filter was used for catching the generated glucose, and the weight of glucose was measured by the analytical balance (Acculab ALC 210.4). So obtained efficiency(ε) was 0.13. The molecular formula of glucose is $C_6H_{12}O_6$.

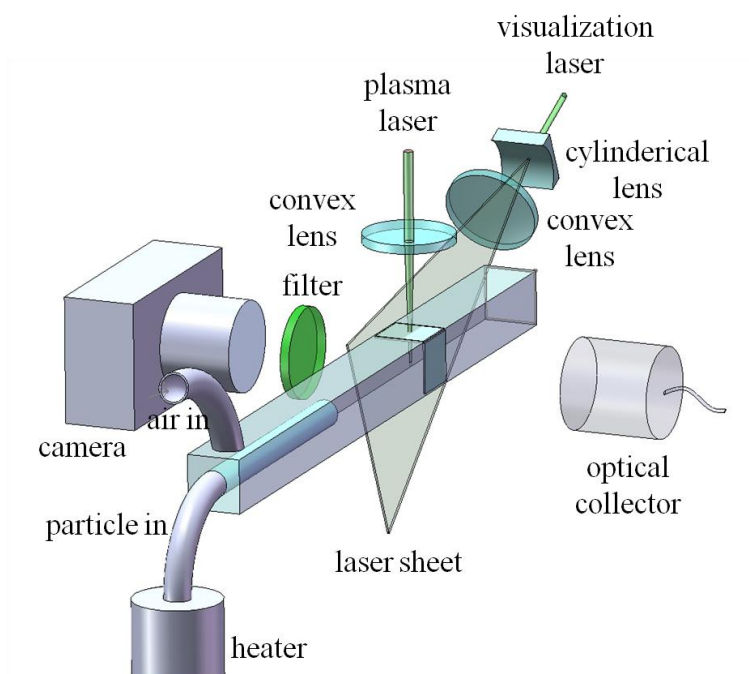
The concentration of generated carbon can be calculated by the concentration of glucose solution, solution feeding rate, and the efficiency of nebulizer¹¹ such that

$$C_A = C_S \varepsilon (F_S / F_G) \quad (5.2)$$

where C_A and C_S are aerosol and solution concentrations of glucose, respectively. F_S is the solution feeding rate to the nebulizer, and F_G is the flow rate of pure air. In summary, the effective carbon concentration ranged from 62.01 $\mu\text{g}/\text{m}^3$ to 409.29 $\mu\text{g}/\text{m}^3$, and every measurement presented here will correspond to the averaged quantity obtained by taking 100 shots. The measurement uncertainty for the glucose concentration in front of nozzle is 2% for the 95% confidence limit.



(a)



(b)

Fig. 5.1 (a) Experimental setup, (b) visualization setup

The gas flow duct had 30 mm x 30 mm in cross sectional area and 500 mm in length. The nozzle tip for injecting glucose particles was at the center of a duct located 50 mm from the detecting sensor. The nozzle length was 200 mm. The fused silica plate (30 mm x 30 mm x 3 mm) was used as an optical window. The gas velocity was measured by the pitot tube and the velocity was measured from 1 m/s to 10 m/s by varying the pure air flow rate. Effectively the concentration decreased with air rate increase. In order to test high speed jet flow, the set up required modification. The pure air nozzle was positioned parallel to a nozzle for the glucose particles. The mixing zone was established at 5 cm ahead of a detecting zone, and the turbulent flow of the jet assured good mix of air and glucose in the mixing zone. The resultant particle flow velocity was ranged from 10 m/s to 70 m/s, which is typical of exhaust plume velocity of aircraft engine. Table 5.1 summarizes the concentration of carbon in the glucose stream with corresponding flow velocity. The measurement uncertainty for the velocity is 16 % for the 95% confidence limit.

As for the LIBS analysis, we used 532 nm Nd:YAG laser (Surelite, Continuum Inc.) which has the maximum energy of 250 mJ and beam diameter of 5 mm. The laser repetition rate and pulse duration were 10 Hz and 6 ns, respectively. The beam was reflected to a mirror and focused by a 60 mm focal length lens into a gas flow in the duct. The tested laser energy was 200 mJ to induce the plasma. The plasma light was collected by a collector which was perpendicular to the laser shooting direction. The collected plasma

light was sent to the echelle spectrometer (Andor Mechelle 5000) which had 0.1 nm resolution and a ICCD (Andor iStar 1024x1024) for recording the signal. To detect the temporal plasma light with specific time delay, the laser and the spectrometer were synchronized by the delay generator (BNC 565). The selected delay time was 2 us after laser shooting to minimize the continuum disturbances.

The visualization was conducted for validation of LIBS signal. The setup is shown in Fig. 5.1 (b) For the visualization, we used 532 nm Nd:YAG laser (minilite, Continuum Inc.) which has the energy of 25 mJ/pulse and beam diameter of 3 mm. The laser is irradiated as a thin sheet into the channel through the cylindrical and convex lenses which have – 30 mm and 700 mm focal lengths, respectively. The plasma generating laser was a Nd:YAG laser (Surelite, Continuum Inc.) with 1064 nm (for LIBS) and 532 nm (for visualization) wavelength. This laser has the maximum energy of 450 mJ and beam diameter of 5 mm. The laser repetition rate and pulse duration were 10 Hz and 6 ns, respectively. The beam was focused by a 60 mm focal length lens into a gas flow in the duct. The tested laser energy was 200 mJ to induce the plasma. The plasma light was collected by a collector which was perpendicular to the laser shooting direction for LIBS analysis. The collected plasma light was sent to the echelle spectrometer (Andor Mechelle 5000) which had 0.1 nm resolution and a ICCD (Andor iStar 1024x1024) for recording the signal.

Table 5.1 Flow velocities for corresponding carbon concentrations

Low speed (m/s)	Concentration ($\mu\text{g}/\text{m}^3$)	High speed (m/s)	Concentration ($\mu\text{g}/\text{m}^3$)
1.5	409.29	9.9	133.46
3.0	204.64	31.3	107.70
3.7	165.93	47.8	87.70
4.6	133.46	65.1	64.62
5.7	107.70	70.0	62.01
7.0	87.70		
9.9	62.01		

There exists a difficulty associated with visualizing particles since the intense plasma light makes it inefficient to recognize the scattered light from particles. So the optical band pass filter which can pass $532 \text{ nm} \pm 3 \text{ nm}$ wavelength light was used for blocking the intense plasma light. After a band pass filter, the scattered light from particles and the plasma light having near 532 nm wavelength was captured by the camera (Nikon) through 60 mm micro lens. The plasma laser, visualization laser and LIBS spectroscopy were synchronized by a delay generator (BNC 565). The irradiation of visualization laser and detection of LIBS spectroscopy were started at the same time after irradiation of the plasma laser with $2 \mu\text{s}$ delay.

5.3 Data analysis

Table 5.2 Hitting rate of carbon particulates for different concentrations

Concentration ($\mu\text{g}/\text{m}^3$)	409.29	204.64	165.93	133.46	107.70	87.70	62.01
F (%)	85	69	55	56	31	40	22

When the focused laser beam is irradiated on the glucose particle stream, there exists hit or miss probability depending on the particle concentration. In order to increase the peak to base ratio, we used the conditional analysis in which single-shot particle “hits” are separated from single-shot particle “misses”[74-76] exclusively. The hitting rate F is defined by

$$F = \frac{n_{sp}}{n} \quad (5.3)$$

where n and n_{sp} are the number of laser shooting and the number of spectra assigned to the particles, respectively. The “hits” is defined by counting the case in which the peak to base ratio is larger than 5 in the present analysis. The baseline is an averaged intensity of entire spectra from 200 to 900 nm. Table 5.2 summarizes the hitting rate of particles for different concentrations. In the experiment, F is found as 22% at $23.8 \mu\text{g}/\text{m}^3$ and 85% at $157.4 \mu\text{g}/\text{m}^3$.

The actual concentration(x) is defined by

$$x = Fx_{sp} \quad (5.4)$$

Here x_{sp} means concentration acquired from just the hitting cases. Assuming Poisson sampling statistics, the sampling frequency F is defined as

$$F = 1 - e^{-\mu} \quad (5.5)$$

where μ is the average number of particles in the effective interaction volume V . The relationship between μ and V can be written as

$$\mu \cong VN_D \quad (5.6)$$

where ND is the number density of particles (particles/unit volume). The relationship between sampling frequency F and number density ND can be derived as

$$-\ln(1 - F) \cong VN_D \quad (5.7)$$

According the relationship (Eq. 5.4) between actual concentration x and x_{sp} deduced from the average of only hits, the parameter p chosen to characterize the LIBS measurements is defined by

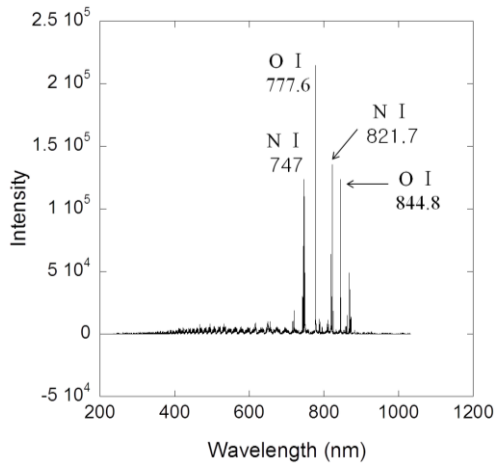
$$p = 100FI \quad (5.8)$$

where I is the average peak intensity for the hits only. The statistical analysis of LIBS signal can be achieved by using these parameters.

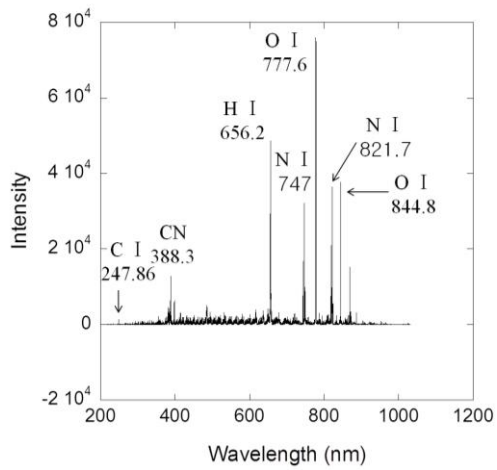
5.4 Results

5.4.1. LIBS spectra in particle stream

Figure 5.2 shows the spectra of air and glucose particles with 200 mJ laser energy and 2 μ s delay time. For air, the carbon spectra (C: 247.856 nm, CN: 388.3 nm) are very low due to small quantity of CO₂ present in air, thus carbon signal would come only from the glucose not present in air. Figure 5.2(b) shows the spectra of glucose particles which have 157.4 μ g/m³ mass concentration of dry glucose particles. The C peak (247.856 nm), CN band peak (388.3 nm), and H peak (656.2 nm) from glucose composition appeared when laser hits the glucose particle as shown in Fig. 5.2(b). When the glucose is dissociated by the high power laser light, the bonds among carbon, hydrogen, and oxygen atoms are separated and the recombination occurs between the separated atoms and the atoms in ambient air. The CN is a molecule which is recombined between the carbon from glucose and the nitrogen from air [5]. We can measure carbon quantity using not only C but also CN band peak which is more easily detected than the atomic carbon peak (247.856 nm) in the current study. Further, the intensity of O and N lines (Air) is relatively low in the glucose particles, and this is because the laser energy is divided into exciting the glucose particles as well as the air during the plasma generation.

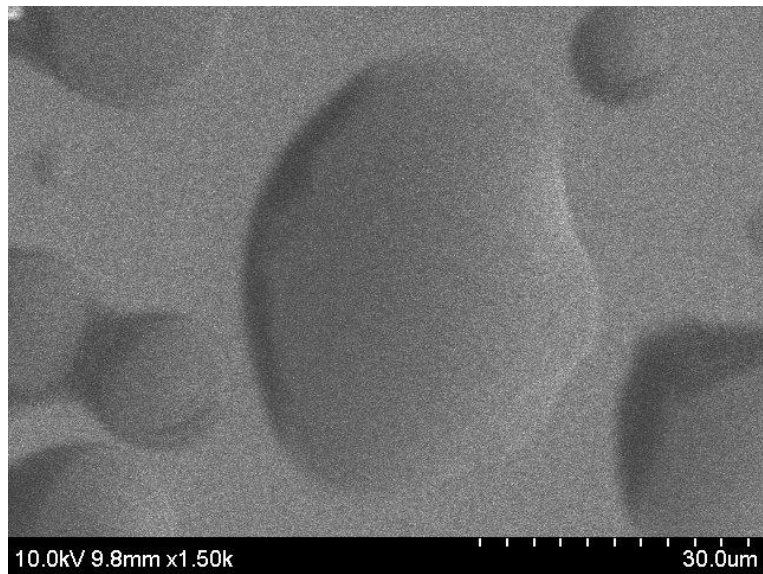


(a)

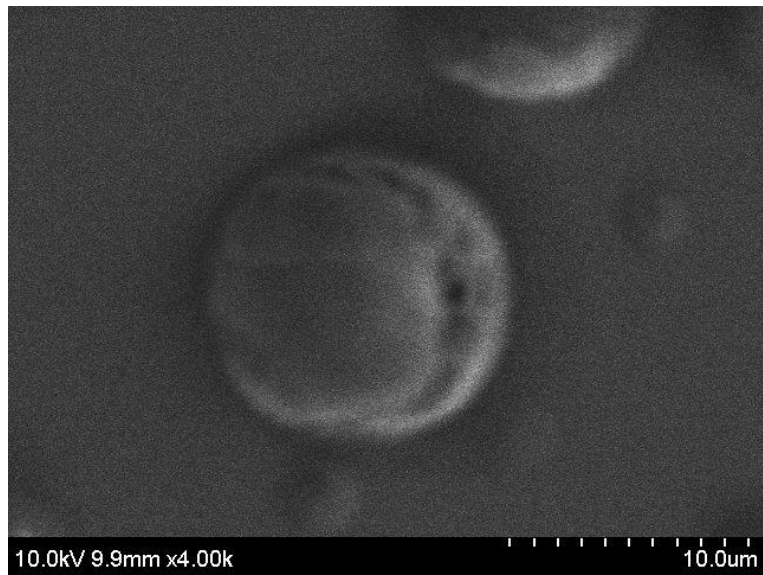


(b)

Fig. 5.2 Spectrum of (a) air and (b) glucose particle of $787.11 \mu\text{g}/\text{m}^3$ concentration. Spectrum of air has O I and N I peaks. Spectrum of glucose particle has C I, CN, H I, O I and N I peaks



(a)



(b)

Fig. 5.3 SEM (Scanning Electric Microscopy) image of glucose particle at
(a) 2 m/s and $409.29 \mu\text{g}/\text{m}^3$, (b) 70 m/s and $62.01 \mu\text{g}/\text{m}^3$

We extracted glucose particle through impacting method on the glass plate. The particle size is obtained from Scanning Electron Microscopy image of extracted glucose particle. The average particle size in low and high speed regime is 14.68 μm and 15.48 μm , respectively. Figure 5.3 shows the SEM images for different velocities (2 m/s and 70 m/s). The glucose particle at the high velocity is smaller than at the low velocity. Table 5.3 summarizes the particle size for different velocity and concentration. The particle size becomes smaller when the velocity becomes faster. But the two different velocity regimes have almost the same particle size. This is because the experiment setup in high velocity regime has shorter mixing distance than low velocity regime.

Table 5.3 Particle size for different velocity and concentration

Low speed (m/s)	Concent. ($\mu\text{g}/\text{m}^3$)	Particle size (μm)	High speed (m/s)	Concent. ($\mu\text{g}/\text{m}^3$)	Particle size (μm)
1.5	409.29	21.49	2.0	409.29	19.49
9.9	62.01	10.16	70.0	62.01	11.47

5.4.2. Visualization of particle and plasma

Figure 5.4 shows the images of particles and plasma obtained by visualization for different concentrations and velocities. The concentrations of particles are (a) 62.01 $\mu\text{g}/\text{m}^3$, 9.9 m/s, (b) 87.7 $\mu\text{g}/\text{m}^3$, 7.0 m/s, (c) 409.29

$\mu\text{g}/\text{m}^3$ in low speed regime, (d) $62.01 \mu\text{g}/\text{m}^3$, 70 m/s, (e) $87.7 \mu\text{g}/\text{m}^3$, 47.8 m/s, (d) $409.29 \mu\text{g}/\text{m}^3$, 2 m/s in high speed regime. The flow direction is from right to left in these images. The obtained plasmas have about 2 mm length and 1mm depth. Though the particle movements have changed randomly to the flow patterns, the plasmas are generated at the same position. Thus, the LIBS detect particles having a random motion at the same position with very small detecting area. Also, there are evaporated particles along the laser path because the particles along the laser path are evaporated by the non-focused laser beam due to its high enough energy. This may give rise to the error of detection in the particle LIBS.

Figure 5.5 shows the visualization images and CN band signal from a single shot LIBS detection. These images of particles and plasma are obtained from different concentrations (a) $62.01 \mu\text{g}/\text{m}^3$ (b) $64.62 \mu\text{g}/\text{m}^3$ (c) $204.64 \mu\text{g}/\text{m}^3$ (d) $409.29 \mu\text{g}/\text{m}^3$. The CN signals for these concentrations are obtained simultaneously in Fig. 5.5(e). It is shown that higher the concentration is, the higher CN intensity is noted. Thus one confirms that LIBS can detect the particle concentration in the plasma volume. The intensity being higher at $64.62 \text{ g}/\text{cm}^3$ than at $204.63 \text{ g}/\text{cm}^3$ can be explained as follows. The visualization image of $64.62 \text{ g}/\text{cm}^3$ in (b) contains more concentrated particle distribution at the plasma volume. The image of (c) $204.64 \text{ g}/\text{cm}^3$ has a wider particle distribution than (b). Thus we believe the presented intensity change

is reasonable.

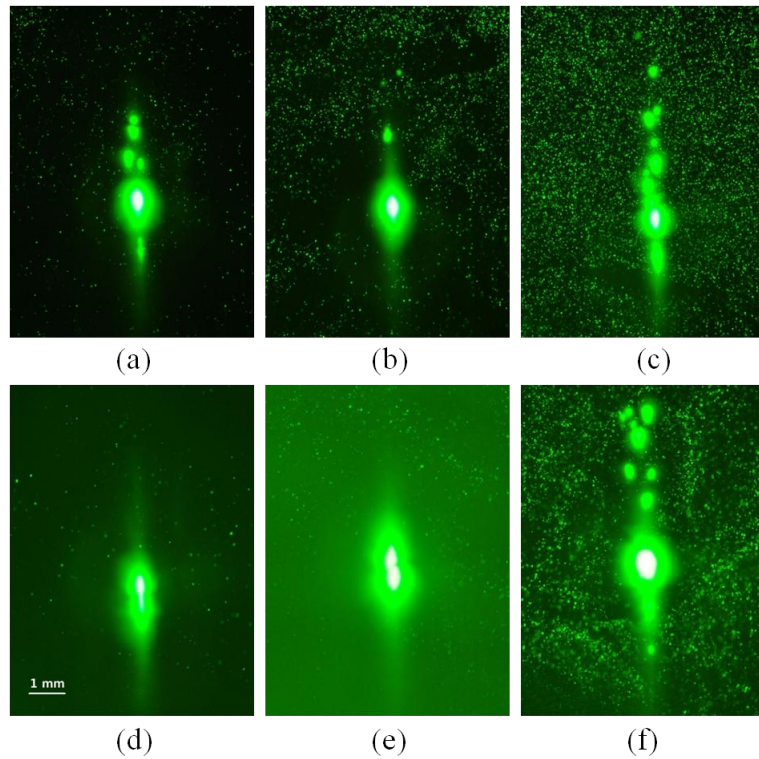


Fig. 5.4 Visualization images of plasma and particles for different concentration and velocity in low (a), (b), (c) and high (d) (e) (f) velocity flow conditions. Low velocity regime : (a) $62.01 \mu\text{g}/\text{m}^3$, 9.9 m/s , (b) $87.7 \mu\text{g}/\text{m}^3$, 7.0 m/s , (c) $409.29 \mu\text{g}/\text{m}^3$, 1.5 m/s and high velocity regime : (d) $62.01 \mu\text{g}/\text{m}^3$, 70 m/s , (e) $87.7 \mu\text{g}/\text{m}^3$, 47.8 m/s , (d) $409.29 \mu\text{g}/\text{m}^3$, 2 m/s

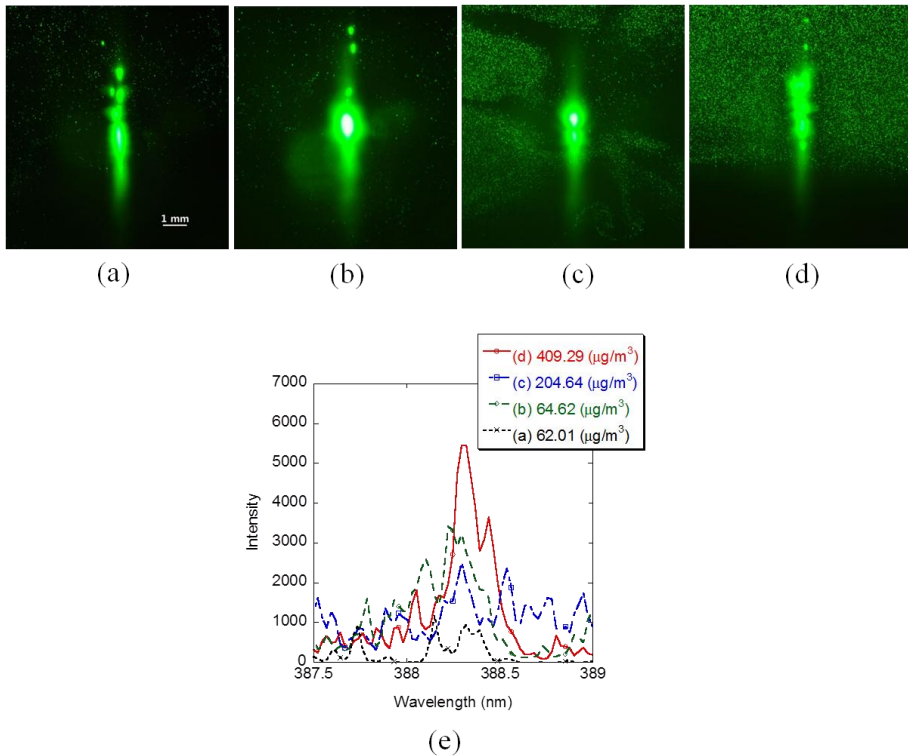


Fig. 5.5 Visualization images of plasma, particle and CN band signal from single LIBS detection for different concentrations obtained simultaneously. (a) 409.29 $\mu\text{g}/\text{m}^3$, (b) 204.64 $\mu\text{g}/\text{m}^3$, (c) 64.62 $\mu\text{g}/\text{m}^3$, (d) 62.01 $\mu\text{g}/\text{m}^3$ and (e) CN band signal from single LIBS detection for different concentrations

5.4.3. LIBS signal for delay time

Figure 5.6 (a) and (b) represent the averaged base line of spectra according to the delay time and magnification of lower intensity region of Fig. 5.6 (a), respectively. This base line is obtained by averaging the whole spectra from 200 nm to 900 nm. The base line decays exponentially with time. Figure 5.6

(c) shows the peak to base ratio of each signal line with delay time which shows the ratio between the spectrum intensity (Fig. 5.6 (a)) and the averaged base line (Fig. 5.6 (b)). The peak to base ratio of H, O and N has the maximum at 6 μ s delay time. This means that 6 μ s delay time is the optimum value for the obtained spectra. Otherwise, the peak to base ratio of CN band peak increases with the delay time which means that the optimal delay time of CN band is much longer than the signals of other atoms. Thus after 8 μ s delay time, the CN band peak is distinguished easily.

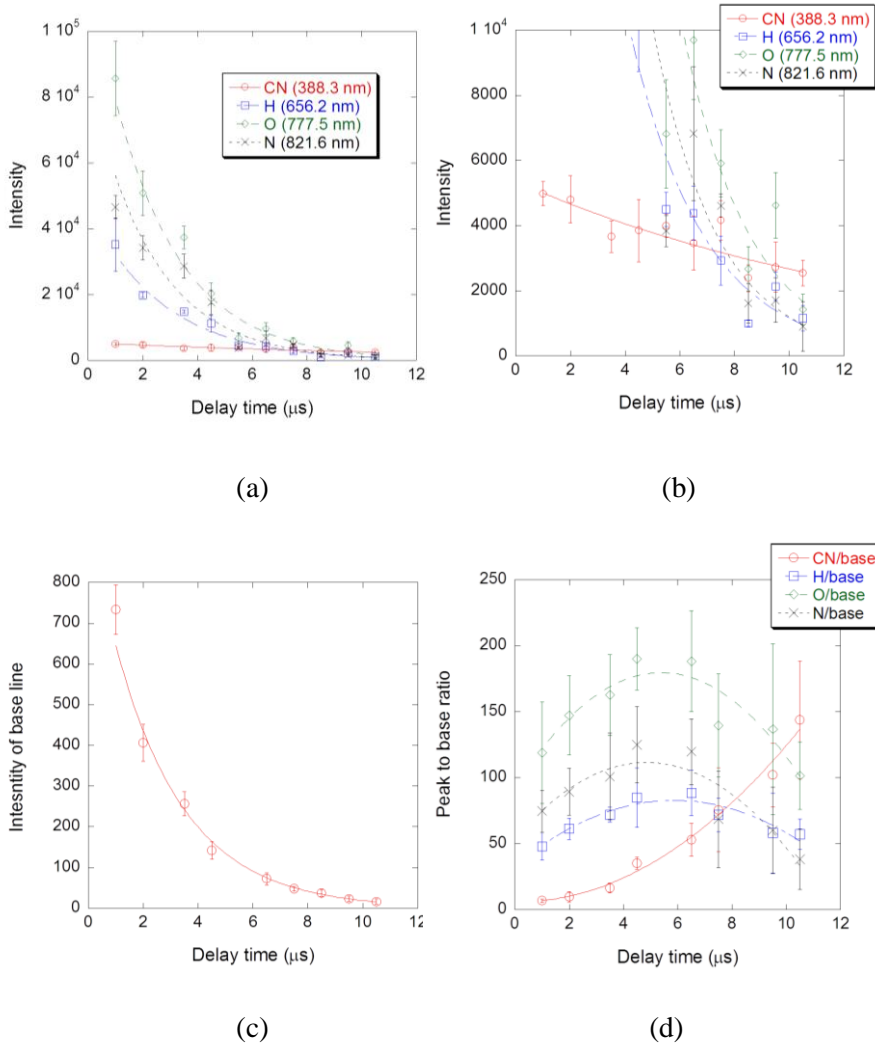


Fig. 5.6 Glucose signals (CN, H, O and N) averaged 100 shots according to the delay time (a) Intensity of glucose signals (CN, H, O and N) according to delay time, (b) Magnification of lower intensity region of Fig. 5.6 (a), (c) Intensity of base line according to delay time, (d) Peak to base ratio of the glucose signal according to delay time

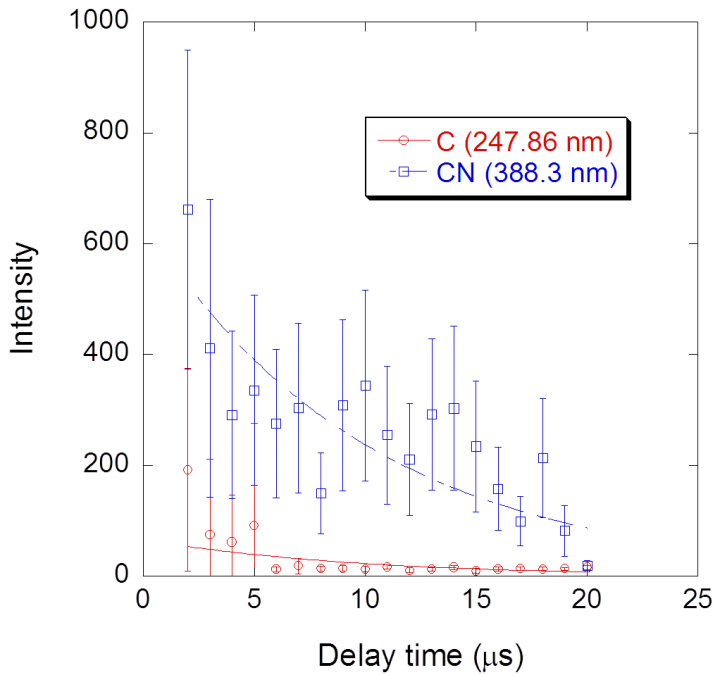
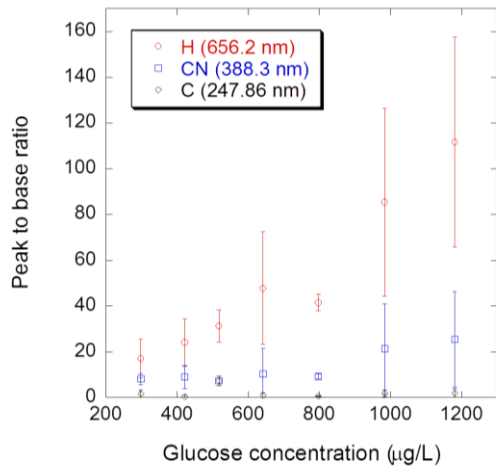


Fig. 5.7 C and CN peaks averaged 100 shots according to the delay time with 200 mJ laser energy and 1 μ s ICCD exposure time

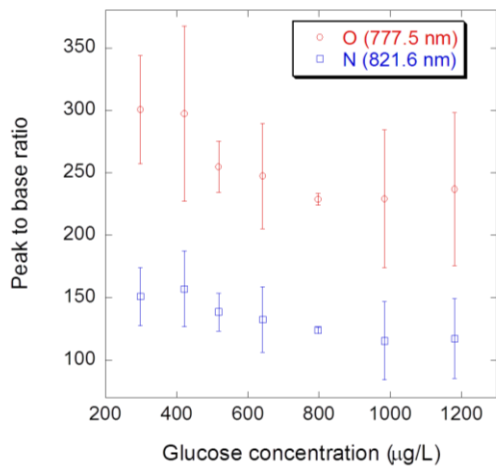
Figure 5.7 shows the intensity of C and CN according to the delay time with 1 μ s exposure time of ICCD. The intensity of C decays rapidly and reaches almost zero after 6 μ s delay time. However, the intensity of CN band peak decays slowly relative to C atomic peak while increasing delay time. This is because C and CN signals originate from electron transition and molecular vibration, respectively.

5.4.4. LIBS signal for carbon concentration

Figures 5.8 (a) and (b) represent peak to base (P/B) ratio of O, N and C, CN, H with the glucose concentration in the glucose stream, respectively. This spectrum is obtained with 2 μs delay time and 20 μs exposure time of ICCD. The glucose concentration is arranged from 298.14 $\mu\text{g}/\text{m}^3$ to 1967.77 $\mu\text{g}/\text{m}^3$ by adjusting the quantity of pure air. The measured peak-to-base (P/B) ratios of O and N shown in Fig. 5.5 (a) decreased with increasing glucose concentration slightly. Increase of the P/B ratio of CN in Fig. 5.8(b) is because N atom from Air becomes CN molecule. But this decreasing rate of P/B ratio of N is small. O also decreases with increasing glucose concentration. The bond energy of glucose and oxygen are 9546 kJ/mol and 498 kJ/mol, respectively. So the oxygen is more easily dissociated than the glucose, and also the electron of oxygen from the Air is more easily excited than the electron of oxygen from the glucose molecule. When the glucose concentration is low, the quantity of oxygen from Air is high in the laser induced plasma and vice versa. So P/B ratio of oxygen is higher in the low glucose concentration than in the high glucose concentration due to difference of electron excitation rate between oxygen from air and oxygen from glucose. When the glucose concentration increases, P/B ratios of CN and H increase linearly as in Fig. 5.8 (b). This increase is because the glucose particle has the C and H compositions.

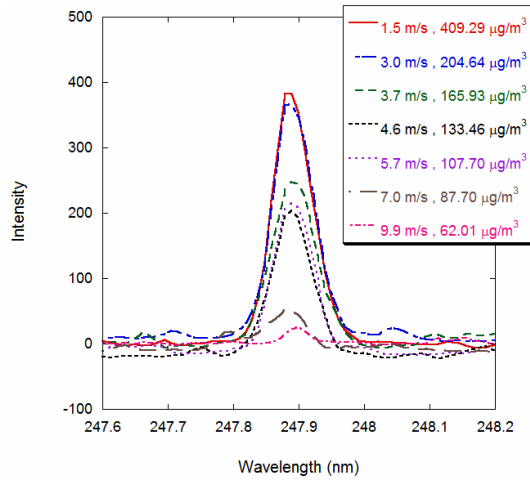


(a)

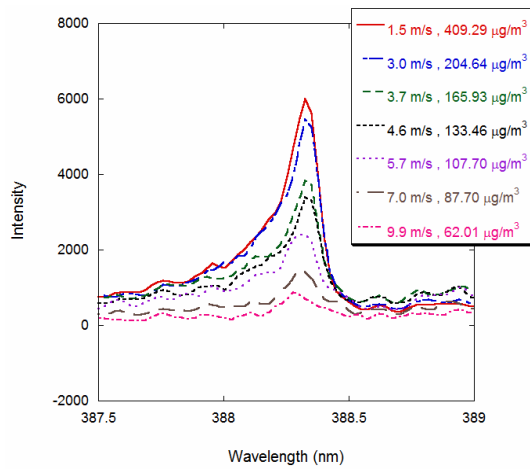


(b)

Fig. 5.8 Peak to base (P/B) ratio according to the glucose concentration, (a) Peak to base (P/B) ratio of O and N according to the glucose concentration, (b) Peak to base (P/B) ratio of C, CN and H according to the glucose concentration



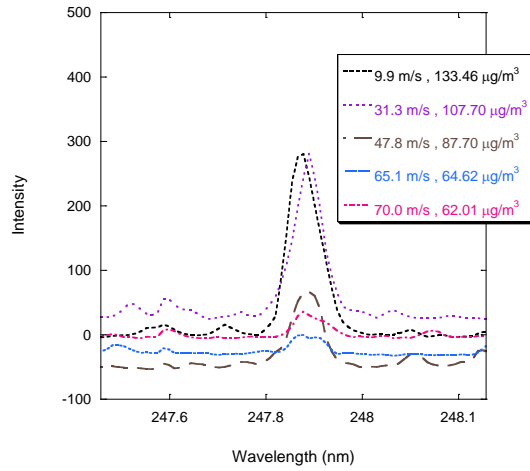
(a)



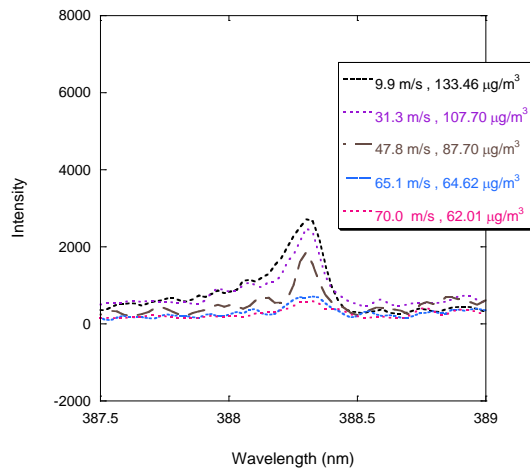
(b)

Fig. 5.9 Carbon and CN band peaks averaged 100 shots with varying low stream velocity (a) Carbon peak averaged 100 shots at 247.86 nm with varying low stream velocity, (b) CN band peak averaged 100 shots at 388.3 nm with varying low stream velocity

Figure 5.9 (a) and (b) illustrate the averaged carbon peak (247.86 nm) and CN band peak (388.3 nm) with varying free stream velocity in low speed regime, respectively. The averaged C and CN band peaks increase with increasing glucose concentration. In the figure, the CN band peak are higher than C peak, possibly due to increasing concentration of CN molecules during chemical reaction between C and N. Figure 5.10 illustrates the averaged C and CN band peaks with varying free stream velocity in the high speed regime. The typical aviation emissions velocity can reach near 70 m/s. The C and CN band peaks at this high velocity are shown in these figures. The peak intensities of C and CN band also increase with increasing glucose concentration. The intensity has almost the same value as in the low speed regime according to each concentration.



(a)



(b)

Fig. 5.10 Carbon and CN band peaks averaged 100 shots with varying high stream velocity (a) Carbon peak averaged 100 shots at 247.86 nm with varying high stream velocity, (b) CN band peak averaged 100 shots at 388.3 nm with varying high stream velocity

Figures 5.11 and 5.12 show calibration curves of carbon using C peak (247.8 nm) and CN band peak (388.3 nm), respectively, according to the carbon concentration for both high and low velocity. The velocities of carbon for both high and low conditions are summarized in Table 5.1. These calibration curves are linear for both conditions, but C peak has bigger fluctuation than CN peak as shown in Figs. 5.11 and 5.12. Though velocity difference of the two conditions is almost 7 times, the intensity of LIBS signal for both conditions is similar. This means that carbon concentration can be quantitatively determined in both speed conditions. By averaging the spectra data, one can generate a calibration curve of varying concentration in real situations such as the aircraft emission monitoring, and thus allowing quantitative analysis of carbon particles. Therefore, the suggested particulate detection scheme is suitable for characterizing organic particulates in the exhaust jet plume of 70 m/s.

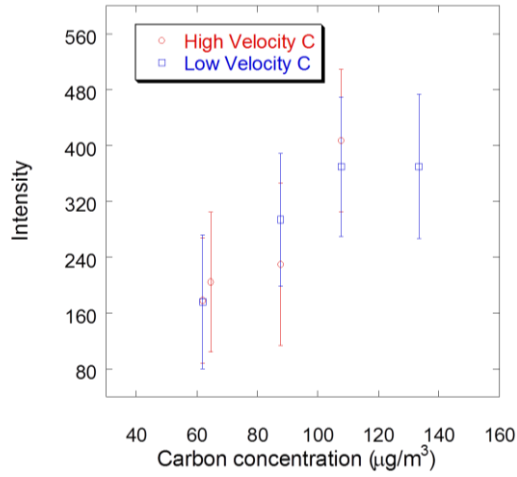


Fig. 5.11 Calibration curve showing response of 247.8 nm C emission to changing concentration of glucose aerosols for both high and low velocity cases

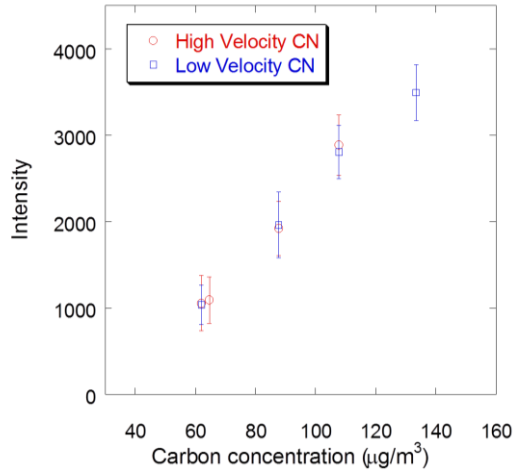


Fig. 5.12 Calibration curve showing linear response of 388.3 nm CN band emission to changing concentration of glucose aerosols for both high and low velocity cases

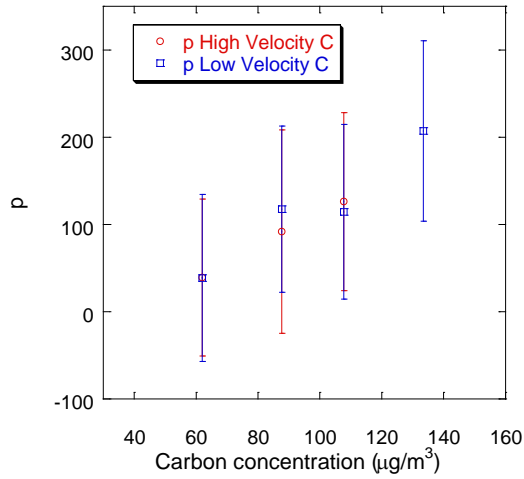


Fig. 5.13 Statistical calibration curve using $p(=FI)$ showing response of 247.8 nm C emission to changing concentration of glucose aerosols for both high and low velocity cases

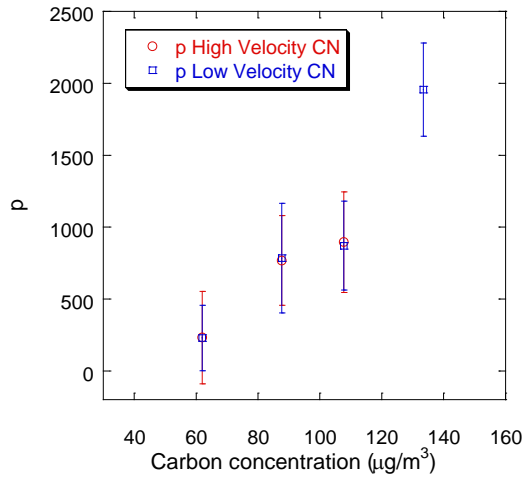


Fig. 5.14 Statistical calibration curve using $p(=FI)$ showing response of 388.3 nm CN emission to changing concentration of glucose aerosols for both high and low velocity cases

Figure 5.13 and 5.14 show statistical calibration curve of carbon using C peak (247.8 nm) and CN band peak (388.3 nm), respectively, according to the carbon concentration for both high and low velocity. These calibration curves also show linear tendency with the slope being less than those of Figs. 5.11 and 5.12.

5.4.5. Limit Of Detection (LOD)

The limit of detection (LOD) of carbon was evaluated using the standard method

$$LOD \cong \frac{3\sigma}{m} \quad (5.9)$$

where σ is the standard deviation of a blank measurement (performed in gas without particles) and m is the slope of the calibration line. Table 5.4 shows LOD for different velocity and spectrum line (C 247.86 nm, CN 388.3 nm). As shown, the LOD of CN signal is 5~6 times less than the LOD of C signal. And the cases at low velocity regime have lower LOD than at high velocity regime because the slope (m) of CN calibration curve is much higher than that of C calibration curve. Also the slope at high velocity regime is higher than the slope of lower velocity regime.

Table 5.4 Limit of detection for different velocity and spectrum line (C 247.86 nm, CN 388.3 nm)

	C (247.86 nm)		CN (388.3 nm)	
	High Velocity	Low Velocity	High Velocity	Low Velocity
LOD ($\mu\text{g}/\text{m}^3$)	150.366	240.43	36.669	42.012

5.5 Conclusion

We conducted carbon particulate detection via LIBS in the high speed free stream resembling the aircraft exhaust flow. C and CN band peaks were selected for evaluating the carbon quantity. The particles and plasma were visualized by an optical system while the LIBS system is used to measure the signal intensity. The particle size is obtained from Scanning Electron Microscopy image of extracted glucose particle. The average particle size in low and high speed regime is 14.68 μm and 15.48 μm , respectively. H, O, N peaks are shown to decay exponentially, where as CN band peak maintained its high intensity with time delay. The CN band peak had relatively longer plasma life time unlike other atomic signals. The calibration curves between the carbon concentration and the signals (C and CN band) were obtained for both high and low velocity conditions. The LOD of CN signal (36.669 $\mu\text{g}/\text{m}^3$ and 42.012 $\mu\text{g}/\text{m}^3$ for high velocity and low velocity regimes, respectively) is

5~6 times less than that of C ($150.366 \mu\text{g}/\text{m}^3$ and $240.43 \mu\text{g}/\text{m}^3$). Also the low velocity conditions have lower LOD than those at high velocity regime. Thus the present attempt in the organic PM detection in the high speed stream is a new attempt with many potential interests of further research.

CHAPTER 6

DIAGNOSTIC OF LIQUID PHASE SAMPLE USING LIUS : PART 1 REDUCED GRAPHENE OXIDE COATED THIN ALUMINUM FILM [19, 20]

6.1 Background and objective

There exists constant need for producing the highly sensitive real-time diagnostic tool in medical and industrial areas [82, 83]. The laser induced ultrasound (LIUS) generation is known as an attractive means to achieve high frequency ultrasound with a broad acoustic bandwidth. Such acoustic wave characteristic comes from the thermoelastic expansion of a laser irradiated thin sample, typically a metal such as Al, Cr, or Ti.[19, 84] The high optical reflectivity and low thermal expansion coefficient of a thin metal film gave rise to a generation of alternative optoacoustic transmitters [19, 85-88]. A composite film of polydimethylsiloxane (PDMS) with carbon black showed higher ultrasound pressure at 20 dB than the Cr film alone [19]. AuNP 2-D array with an overlying PDMS layer improved the frequency (5 dB over 70–100MHz) as compared with those of carbon black-PDMS composites [85, 86].

Baac et al. used a carbon nanotube-PDMS composite and achieved 18 times stronger signal than the comparison metal group with a broadband frequency [87]. Recently, an innovative light-absorber using the photonic crystal-metallic (PCM) structure was developed which can absorb 100% optical energy of a specific wavelength in a total-internal-reflection geometry [88]. This combined PCM and PDMS transmitter showed one order of magnitude higher ultrasound signal than the previous 2-D AuNP nano-structure film with PDMS.

Despite its acclaim as miracle material, graphene as a candidate for optoacoustic wave generation is yet to be confirmed. Because of its electronic, thermal, optical, and mechanical properties as being superior to those of conventional materials, many researchers have pursued research on graphene's basic properties or on its potential applications [20]. The fabrication of rGO demonstrated production of graphene at a low cost [89]. The light absorptivity of rGO increases when thickness of rGO increases [90], and rGO thin films have exceptionally high thermal conductance. We demonstrate the use of rGO layered on a thin aluminum film as an optoacoustic transmitter for generation of strong and high frequency ultrasound wave.

6.2 Experimental condition

Figure 6.1 shows the sketch of a side view of rGO coated Al, layered on a glass. The glass substrate was a commercial glass wafer (Pyrex 7740) with 500 μm thickness. GO was synthesized from graphite flakes by a modified Hummers method, dispersing in water [91]. The prepared GO solution was dropped on a piranha-cleaned glass substrate, followed by spin-coating procedure. The GO film was formed by spin-coating at 5000 rpm for 30 s. For reduction of the GO film, the GO-coated glass substrate was annealed at 400 C for 1 h. Then aluminum thin film was deposited on the rGO coated glass substrate using E-gun evaporator (ZZS550-2/D, Maestech Inc.) with 100 nm depth size.

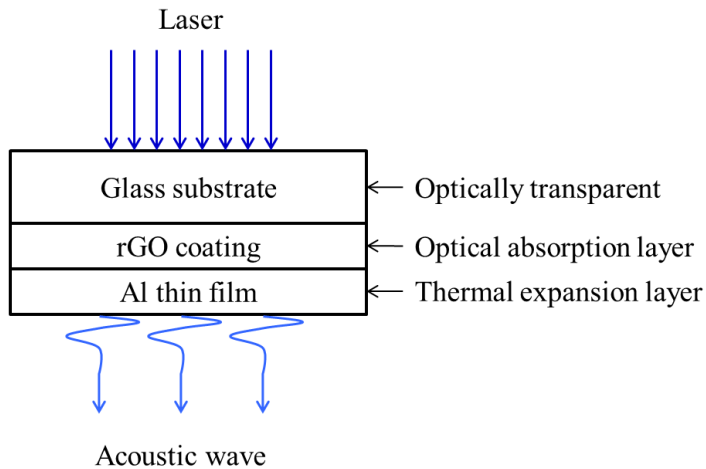


Fig. 6.1 Sketch of the side view of rGO (20, 100, 200 nm) coated aluminum film (100 nm) on a glass substrate (500 μm)

Figure 6.2 shows an experimental setup for thermoelastic wave generation of ultrasound test. The rGO-Al film on 30mm by 30mm glass substrate was mounted on a sample holder and placed into a water. The laser excitation source was a solid state laser (Surelite, Continuum, Inc.) which produces 5 ns laser pulse with energy of 250 mJ per pulse at 532 nm wavelength. Since the excited laser diverges along the beam path, the resulting beam diameter was increased from 6 mm to 10 mm at the sample position. The generated acoustic wave was evaluated using a hydrophone and the shadowgraphy for measuring pressure and acoustic wave visualization, respectively. The hydrophone was a membrane type (HMB-0500, Onda Inc.) for measuring the broadband frequency (0.5–45 MHz), and it was mounted away from the sample at 2.8 mm and 4.6 mm distances. The voltage signal was sent to the oscilloscope (Waverunner64xi, Lecroy Inc.) through the amplifier where the broadband frequency up to 600 MHz was measured at a high sampling rate (<10 GHz).

The visualization of acoustic wave was conducted using another Nd:YAG laser (Minilite, Continuum Inc.) at 532 nm wavelength, 5 ns pulse duration, and 25 mJ per pulse of energy. This visualization laser was synchronized with the probing laser for acoustic wave generation via the pulse generator (BNC 565). The visualization laser was diverged through a concave lens having a focal length of 30 mm. The diverging beam was collimated by a convex lens having a 500 mm focal length. Passing through the test section, the collimated beam was focused by a convex lens having 100mm focal length. Finally, the

laser beam is captured by a CCD camera (Nikon) for visualization. If a density change is detected in the acoustic field of water, the laser beam strayed from its direction as to allow shadowgraphic imaging.

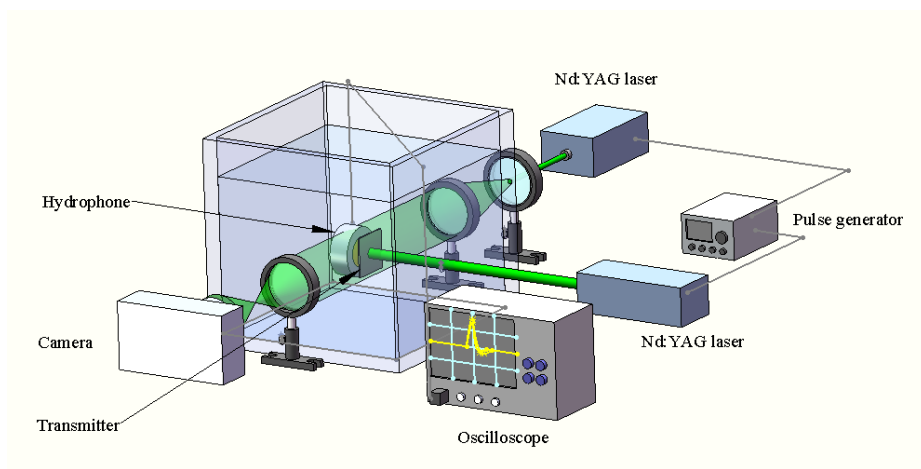


Fig. 6.2 Experimental setup

6.3 Results

Figure 6.3 shows the output pressure waveforms generated from four samples having different rGO thicknesses under the same laser fluence (56 mJ/cm^2). Each curve was obtained by averaging five waveforms. The pressure obtained with 100 nm rGO–Al film was about 64 times higher than the Al-only case. Since the light reflectance of Al film is about 90%, the optoacoustic wave generated from Al-only transmitter is seen weaker than others. The 100 nm rGO coated Al shows higher peak pressure than both 20 nm and 200 nm

rGO coated samples. The rGO has higher light absorption at an increasing thickness.¹² Due to high light absorption of rGO layer, efficiency of the energy transfer from photon to phonon of the rGO coated Al is exceptional.

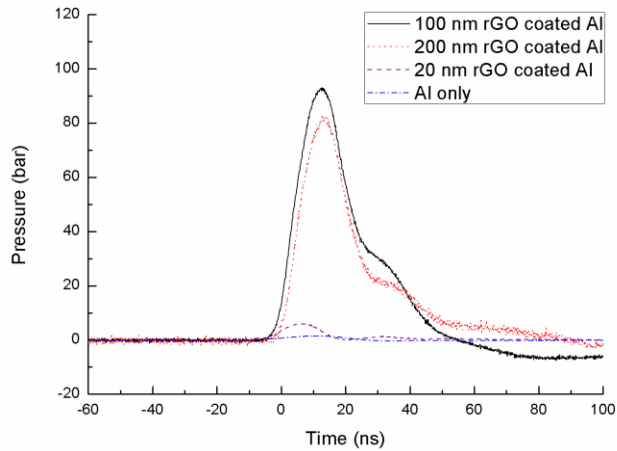


Fig. 6.3 Optoacoustic signals from each transmitter (Al-only, 20 nm rGO coated Al, 100 nm rGO coated Al, and 200 nm rGO coated Al) at 56 mJ/cm^2 positioned 2.85 mm from the hydrophone

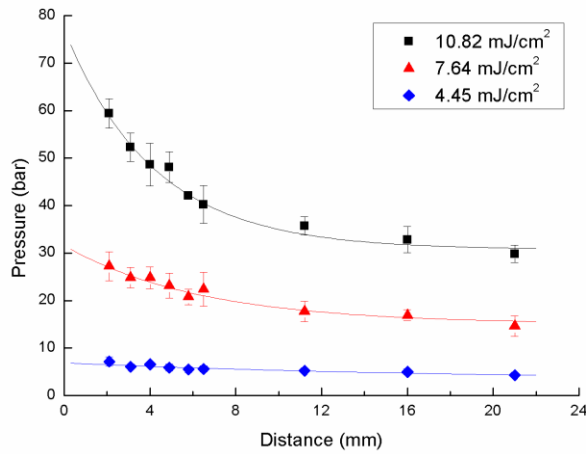


Fig. 6.4 Maximum pressure of optoacoustic wave from 100 nm rGO coated Al according to the distance between the transmitter and detector for varying laser fluences

Figure 6.4 shows maximum pressure of the optoacoustic wave generated from 100 nm rGO coated Al according to the distance between the sample (transmitter) and the hydrophone for three different laser fluences. The optoacoustic wave is attenuated exponentially along the distance. The maximum pressure becomes almost constant beyond 15mm from the transmitter and is estimated at 75 bar at 43.28 mJ/cm² near the transmitter surface.

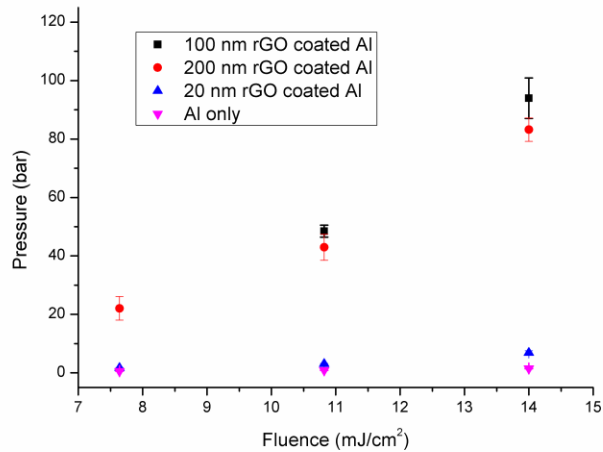


Fig. 6.5 Maximum pressure of optoacoustic wave from 20 nm, 100 nm, 200 nm rGO coated Al and Al only for varying fluences as measured 2.85 mm from the sample

Figure 6.5 shows maximum pressure generated from the three samples (20 nm, 100 nm, and 200 nm rGO coated Al, and Al only) according to laser fluences. The increase in peak pressure from Al-only film is barely distinguishable with increasing laser energy while the peak pressure from 100 nm rGO coated Al increases rapidly with increasing laser energy. Also, high pressure generation is shown repeatable for the same rGO sample at varying laser fluences. This confirms the origin of high pressure ultrasound being the thermoelastic response of a transmitter rather than the surface breakdown of the sample at high irradiance. Furthermore, the high pressure generation is explained in the context of the graphene properties combined with high

thermoelasticity of aluminum. Table 6.1 shows different coefficients of thermal expansion (CTE). Al has relatively low positive CTE (i.e., tension) while either graphene or graphite has negative CTE (i.e., compression). When the laser beam is irradiated on the rGO, the heat energy diffusion to Al occurs with high thermal diffusivity of rGO likely higher than the measured value of graphene at 5300 W/mK [92]. Here, the negative CTE allows rGO to contract while the imparted temperature gradient allows the aluminum to expand. This combined material response or an “impulsive bending” motion of the composite transmitter is believed to generate the strong pressure wave observed here. This observation also suggests that rGO-PDMS transmitter may well provide even higher optoacoustic wave which can be tested in the future.

Table 6.1 Coefficient of thermal expansion for different materials

Materials	Coefficient of thermal expansion [10^{-6} K^{-1}] at room temperature
PDMS[19]	310
Water	69
Aluminum	23.1
Graphen[93, 94]	-8
CNT[95]	-0.3

Figure 6.6 shows visualization images of optoacoustic waves at three laser fluences (17.8 mJ/cm^2 , 30.56 mJ/cm^2 , and 43.28 mJ/cm^2) taken at $4 \mu\text{s}$ after the laser shot directed from the left. For each transmitter (Al only, 20nm rGO coated Al, 100 nm rGO coated Al, and 100 nm rGO only) at a given laser fluence, the width of optoacoustic wave is about 10mm which is the same as the beam diameter. If a measured pressure of acoustic wave is high, then the visualized wave thickness is expanded. Particularly for higher fluence images (f, h and i), the successive coalescence of semi-circular waves into a planar strong acoustic wave is observed. Any trace of surface chemical reaction is not observed from the rGO samples even after observing such a pressure. An interesting observation is that for 100nm rGO only transmitter in Fig. 4.6, the transmitting source of such optoacoustic wave is the water, which is heated by a rapidly conducting graphene alone.

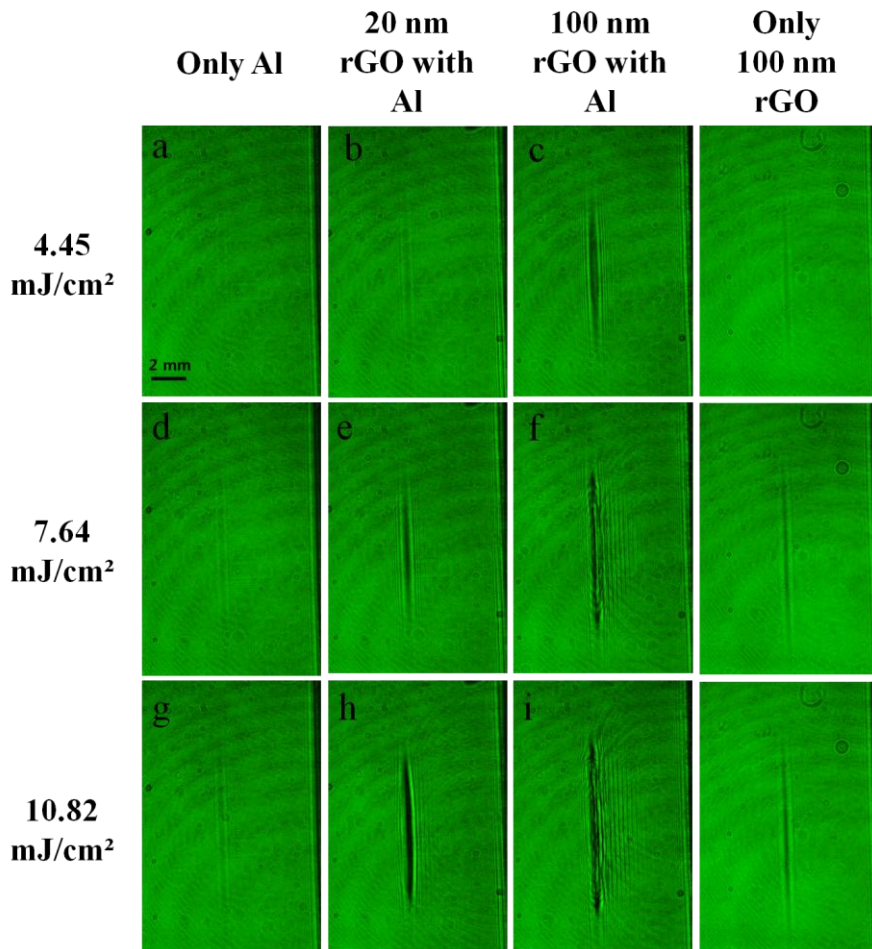


Fig. 6.6 Visualization images of propagating optoacoustic (left running) wave from 4 different transmitters (Al-only, 20 nm rGO coated Al, 100 nm rGO coated Al, 100 nm rGO only) positioned on the right for 3 laser fluences (17.5 mJ/cm^2 , 30.56 mJ/cm^2 and 43.28 mJ/cm^2) taken at $4 \mu\text{s}$ after the laser shot directed from the left

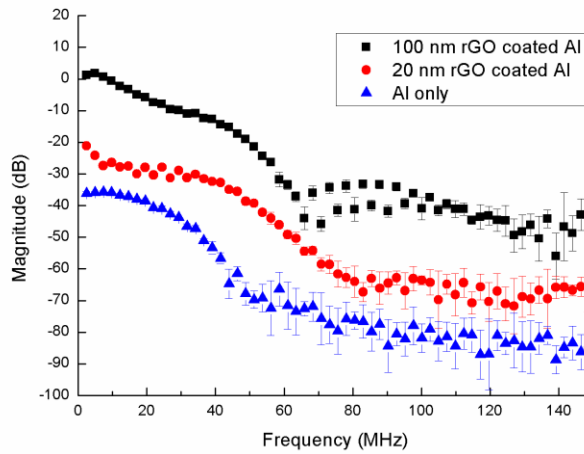


Fig. 6.7 Frequency spectra for the optoacoustic waves from 20 nm, 100 nm rGO coated Al and Al only) for 56 mJ/cm^2 measured at 2.85 mm away from the sample

Figure 6.7 shows the frequency domain spectra of the tested transmitters of Fig. 6.3. It shows that the magnitude of the frequency spectrum of 100 nm rGO coated Al has about 40 dB increase in comparison to the Al-only sample. This efficient generation of a high frequency signal from graphene– aluminum film is due to an exceptional energy dissipation by nanometer-thick layers of rGO which also prevented beam reflection at the aluminum film allowing the optimal thermoelastic response of the proposed transmitter.

6.4 Conclusion

We demonstrate that rGO coated aluminum thin film is an excellent optoacoustic transmitter for generating strong and high frequency ultrasound waves. The pressure signal is measured by a hydrophone, and the acoustic wave images are obtained by the shadowgraphy. The optoacoustic transmitter based on the rGO layer and aluminum film on a glass substrate generate the pressure wave that is approximately 64 times stronger than that obtained when aluminum-alone film is used. The generated optoacoustic wave is attenuated exponentially along the distance, and the coalescence of spherical waves at high laser fluences results in high pressure generation. Results show that the magnitude of the frequency spectrum of rGO coated Al has approximately 40 dB increase from the Al-alone film. The present study suggests a method of generating the high pressure LIUS signal with high frequency at low laser fluences and may help to build all-in-one optical transducer for medical diagnostics.

CHAPTER 7

DIAGNOSTIC OF LIQUID PHASE SAMPLE USING LIUS : PART 2 REDUCED GRAPHENE OXIDE COATED POLYDIMETHYLSILOXANE (PDMS) FILM [96]

7.1 Background and objective

The ultrasound imaging or sonography is used in both veterinary medicine and human medicine to diagnose and treat disease [83]. The ultrasound generation is typically based on the electrical means via the piezoelectric transducers [97] with the maximum frequency limited below 80 MHz. The laser induced ultrasound (LIUS) generation is known to offer an attractive alternative to attain high frequency ultrasound with a broad acoustic bandwidth. The characteristics of LIUS wave depend strongly on the material properties of transmitters. Though a thin metal film is an obvious choice for ultrasound generation, the high optical reflectance, and low coefficient of thermal expansion (CTE) are however responsible for weak signals at the high frequency regime [19]. In the past, polydimethylsiloxane (PDMS) material was found to be effective for ultrasound generation due to its high CTE (310

$\times 10^{-6} \text{ K}^{-1}$). A composite film of PDMS with carbon black showed improved ultrasound pressure than the Cr film alone [19]. Also, Baac et al. used carbon nanotube (CNT)- PDMS composite and achieved 18 times stronger signal than the comparison metal group with a broadband frequency [87]. Recently, Colchester et al. demonstrated that the carbon nanotube-PDMS composite coated on optical fiber can be used for LIUS generation [98].

Graphene is a “miracle material” for its superior electronic, thermal, optical, and mechanical properties as compared to those of conventional materials [20]. The rGO (reduced graphene oxide) coating, which has similar properties as graphene and low fabrication price [89], was used for generation of strong optoacoustic wave with the metal film such as aluminum [99]. The rGO-metal, however, had limitations for generation of strong optoacoustic wave due to the low CTE of metal. In the present investigation, a transmitter based on rGO-PDMS as opposed to rGO-metal is developed to overcome the known drawbacks thus discussed. The exceptionally high thermal conductance of rGO film helps to increase the response time of PDMS. We demonstrate that rGO-PDMS film is a viable choice of optoacoustic probe, generating a strong pressure and the high frequency ultrasound wave, previously unattainable via the earlier layered systems.

7.2 Experimental condition

Figure 7.1 shows sketch of the side view of rGO coated PDMS, layered on a glass. A glass substrate which was a typical glass wafer (Pyrex 7740) with 500 μm thickness was piranha-cleaned. Plasma surface treatment (MyPL, APPLASMA Co.) was conducted on the glass substrate to help the coating of GO solution. Commercial GO solution (UHC GO- 175, UniNanoTech Co.) was dropped on the surface of the glass substrate, followed by a spin-coating procedure. The spin-coating of the GO solution proceeded at 5000 rpm for 30 s. Then the GO-coated glass substrate was annealed at 200 $^{\circ}\text{C}$ for 2 h in a vacuum chamber, for the reduction of the GO film.⁹ PDMS was mixed with carbon black (45nm particle size, Raven 14, Columbian Chemicals, Inc.) with a ratio of 5.5:1. The mixed PDMS-carbon black was deposited on rGO coated glass substrate using the spin coating procedure at 5500 rpm for 120 s. The coated sample was cured at 100 $^{\circ}\text{C}$ for an hour. The thickness of the PDMS film was 11 μm as measured with a 3D measuring laser microscope (Olympus, LEXT OLS4100). Also, aluminum thin film was deposited on the rGO coated glass substrate using E-gun evaporator (ZZS550-2/D, Maestech, Inc.) with 100 nm thickness size.

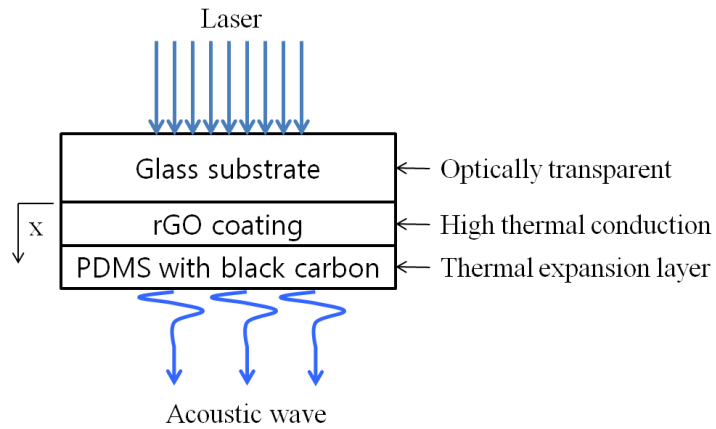


Fig. 7.1 Sketch of the side view of rGO coated PDMS film on a glass substrate (500 μm)

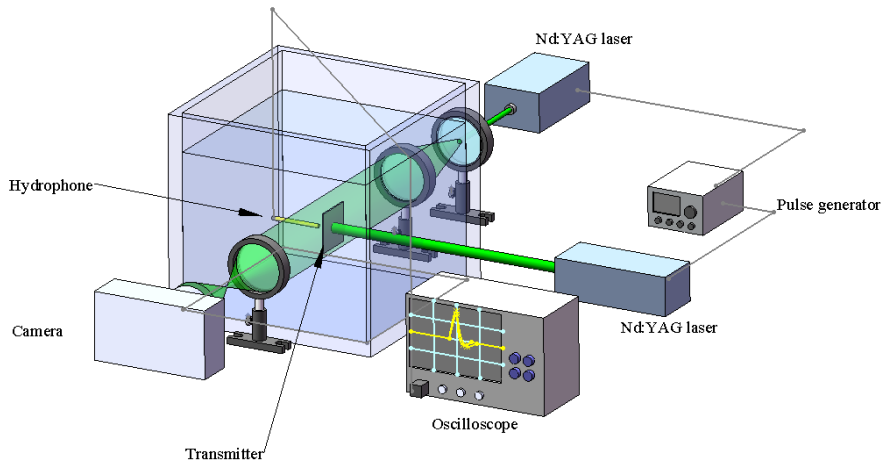


Fig. 7.2 Experimental setup

The experimental setup for laser-induced ultrasound wave generation is shown in Fig. 7.2. A glass wafer with a rGO-PDMS film is mounted on a sample holder and placed in the water. The Nd:YAG laser (Surelite, Continuum, Inc.) is used for generation of LIUS wave, which produces 5 ns laser pulse with 250 mJ of energy per pulse at 532 nm wavelength. The irradiation area of the excitation laser is 0.785 cm^2 . The pressure of generated ultrasound wave is measured with a hydrophone, and the acoustic wave is visualized using a shadowgraph technique.¹⁰ The hydrophone is a needle type (HNR-1000, Onda, Inc.) for measuring the broadband frequency (0.25–10 MHz), and it is positioned at 3mm from the sample. The voltage signal is sent to the oscilloscope (Wavesurfer64MXs-B, Lecroy, Inc.), where the broadband frequency up to 600MHz is measured at high sampling rate of 10 GS/s. The visualization of acoustic wave is conducted using a shadowgraph method that uses a separate Nd:YAG laser (Minilite, Continuum, Inc.) at 532nm wavelength, 5 ns pulse duration, and 25 mJ per pulse of energy. This laser is synchronized with the probing laser for acoustic wave generation via the pulse generator (Stanford Research Systems, DG 645), and then the CCD camera (Nikon) is used to capture the resulting beamed image.

7.3 Results

Figure 7.3 shows the output pressures from four test samples having

different coatings at laser fluence of 35.66 mJ/cm^2 . Each curve was obtained by averaging three waveforms. CTE, thermal conductivity, light absorptance, and film thickness of materials are presented in Table 7.1. The pressure from Cr layer is 1.5 times higher than the Al result due to high light absorptance [100, 101]. The pressure obtained with 100nm rGO–PDMS film is about 76 times higher than the Al-only case. Since the light absorptance of Al film is about 9%, the optoacoustic wave generated from Al-only transmitter is seen weaker. Also, the pressure obtained with 100nm rGO–PDMS film is about 5 times higher than PDMS only and 2.2 times higher than the 100 nm rGO coated Al.

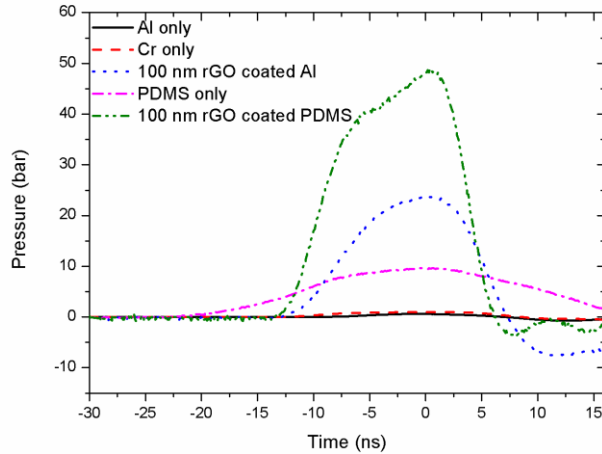


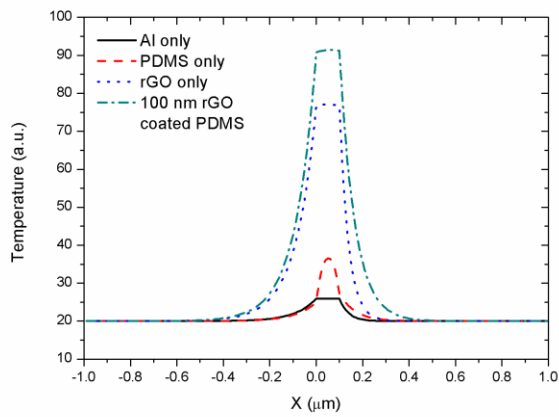
Fig. 7.3 Optoacoustic signals from each transmitter (Al-only, Cr-only, 100 nm rGO coated Al, PDMS only and 100 nm rGO coated PDMS) at 35.66 mJ/cm^2 positioned 3 mm from the hydrophone

Table 7.1 Coefficient of thermal expansion, thermal conductivity, absorptance, and thickness of film for different materials.

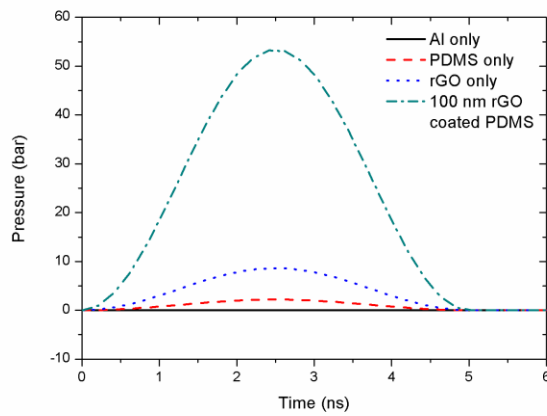
Materials	Coefficient	Thermal conductivity (k, W/mK)	Absorptance	Thickness of film (μm)
	of thermal expansion [10^{-6}K^{-1}] at room temperature		at 532 nm wavelength (%)	
PDMS	310 [3]	0.15	96	11
Water	69	0.58
Aluminum	23.1	237	9	0.1
Chromium	4.9	93.9	58	0.1
Graphene	-8 [16 17]	5300 [19] (in-plane)	2.3 [22]	...
rGO	...	0.14-2.87 [20]	...	0.1
CNT	-0.3 [18]	6600 [21]	7 [23]	...
rGO-Al	88	0.2
rGO-PDMS	95	11.1

This high pressure generation is related to a high CTE of PDMS and thermal properties of graphene, as shown in Table 7.1. The cross-plane thermal conductivity of graphene is approximately two orders of magnitude lower than its in-plane thermal conductivity [102]. Furthermore, the response time of transmitter with respect to laser irradiation is related to generation of high frequency ultrasound wave. The response time of 100 nm rGO–PDMS film is much faster than the PDMS film since PDMS has a very low thermal conductivity. The rGO-PDMS film has effectively compensated the slow response time of PDMS.

The 1-dimensional analysis of acoustic wave generation is conducted [21, 103]. Figures 7.4(a) and 7.4(b) show the calculated temperature along the cross-plane (x), and the calculated pressure with respect to time for different layered systems, respectively. The maximum values of temperature and pressure are obtained for the rGO-PDMS layered system, which are consistent with the experimental findings from Fig. 7. 3.



(a)



(b)

Fig. 7.4 1-dimensional analysis of optoacoustic wave generation (a) the time constant of heat propagation in the laser irradiated layers (b) the time related the acoustic wave propagation and attenuation by the laser pulse for different films (Al-only, PDMS only, rGO, and 100 nm rGO coated PDMS) at

$$35.66 \text{ mJ/cm}^2$$

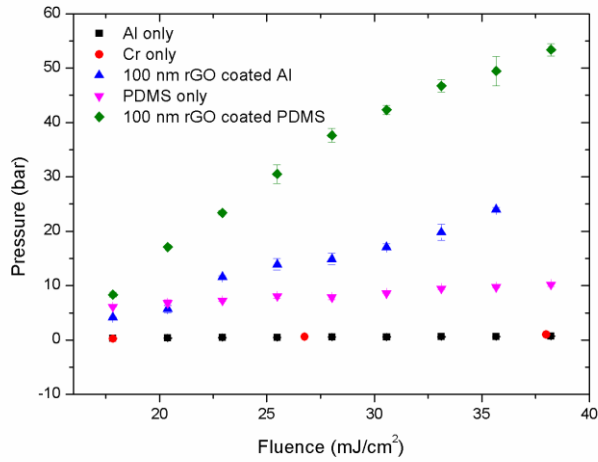


Fig. 7.5 Maximum pressure of optoacoustic wave from Al only, Cr only, 100 nm rGO coated Al, PDMS only, 100 nm rGO coated PDMS for varying fluences as measured 3 mm from the sample

Figure 7.5 shows the maximum pressure generated from the four samples (Al only, Cr only, 100 nm rGO coated Al, PDMS only, and 100 nm rGO coated PDMS) according to laser fluences. The increase in peak pressure from Al-only film and Cr-only film is barely distinguishable with increasing laser energy, while the peak pressure from 100 nm rGO coated Al increases rapidly with increasing laser energy. This result is well matched with the study reported previously [99]. Also, the slope of peak pressure according to the laser energy fluence for 100 nm rGO coated PDMS is the steepest in all coatings. This is because the CTE of PDMS is much higher (13 times) than Al. When the laser beam is irradiated on rGO, heat is dissipated to PDMS with

rGO. Here, the negative CTE allows rGO to contract, while the imparted temperature gradient allows the PDMS to expand. The expansion of PDMS is much bigger than Al due to high CTE. This rGO-PDMS combination response or an “impulsive bending” motion of the composite transmitter is believed to generate such strong pressure wave observed herein.

Figure 7.6 shows visualization images of optoacoustic waves at three laser fluences (25.37 mJ/cm^2 , 30.57 mJ/cm^2 , and 35.66 mJ/cm^2) taken at $3 \mu\text{s}$ after the laser shot directed from the left. If a measured pressure of the acoustic wave is high, then the intensity difference between the visualized wave and background image grows. The pressure of optoacoustic wave from rGO-PDMS film is higher than Al and PDMS cases, which corresponds to pressure profiles of Fig. 7.5. The irregular and rough surface structure of the rGO coat caused multiple signal transmission of spherical as opposed to planar waves originated from the surface, to merge with the slower planar (main) wave as depicted from Fig.7.6.

Figure 7.7 shows the frequency domain spectra of the tested transmitters of Fig. 7.3. It shows that the magnitude of the frequency spectrum of 100 nm rGO coated PDMS has about 40 dB increase in comparison to the Al-only sample. The magnitude of the frequency spectrum of PDMS film is similar to that of 100 nm rGO coated Al at the low frequency domain, but it decreases at the high frequency domain due to the slow response time of PDMS. On the

other hand, the 100 nm rGO coated PDMS keeps high magnitude at the high frequency domain up to 200 MHz due to the fast response time of rGO coating. This efficient generation of a high frequency signal from graphene–PDMS film is due to an exceptional energy dissipation by nanometer-thick layers of rGO and high thermal expansion characteristic of PDMS material that allowed for the optimal thermoelastic response of the proposed transmitter. The obtained high time resolution is suitable for real time imaging, and the high spatial resolution may further improve the microscopic medical imaging.

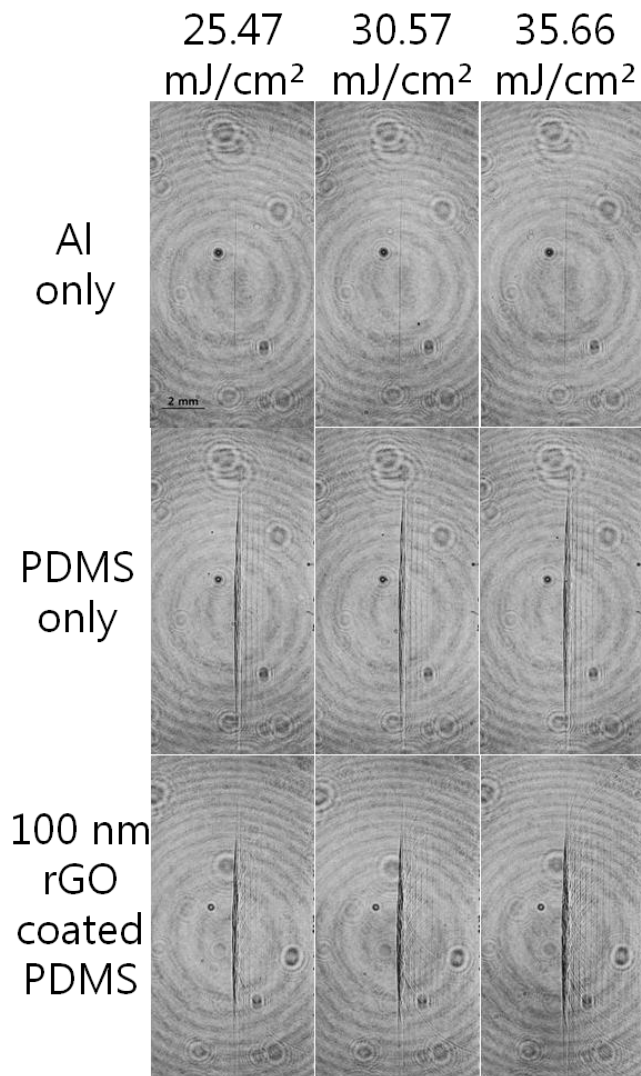


Fig. 7.6 Visualization images of propagating optoacoustic (left running) wave from 3 different transmitters (Al only, PDMS only and 100 nm rGO coated PDMS) positioned for 3 laser fluences (25.37 mJ/cm² , 30.57 mJ/cm² and 35.66 mJ/cm²) taken at 3 μ s after the laser shot directed from the left

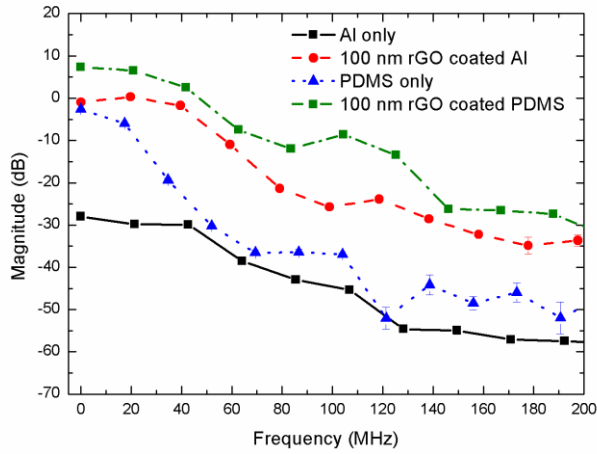


Fig. 7.7 Frequency spectra for the optoacoustic waves from Al only, 100 nm rGO coated Al, PDMS only and 100 nm rGO coated PDMS for 35.66 mJ/cm^2 measured at 3 mm away from the sample

7.4 Conclusion

We demonstrate that rGO coated PDMS film is an excellent optoacoustic transmitter for generating strong and high frequency ultrasound waves. The pressure signal is measured by a hydrophone, and the acoustic wave images are obtained by the shadowgraph technique. The optoacoustic transmitter based on rGO-PDMS film on a glass substrate generated a pressure signal that was 76 times the Al-alone, 5 times the PDMS-alone, and 2.2 times the rGO-Al cases. The magnitude of frequency spectrum of rGO-PDMS is approximately 40 dB higher than Al-alone, 25 db higher than PDMS-alone, and 10 dB higher

than rGO-Al film, at the broadband frequency range. The promising laser-induced ultrasound wave generation suggested by the present study provides a viable alternative to conventional electrical ultrasound transducers for medical imaging.

CHAPTER 8

CONCLUSION

In this study, we used LIBS and LIUS to diagnose various thermo-fluid applications. We investigated the LIBS characteristics in various phase conditions including a single phase (gas) and two phases (liquid gas, solid gas) for thermo-fluid application. For single-phase (gas) analysis, we presented a novel effort to generate two-dimensional maps of the chemical information of propane flames using LIBS point measurements at various positions. The LIBS base signal provides the density field of a flame via the relationship between the density and the laser plasma intensity. Additional flame information that is unavailable via other means, such as density, atomic and molecular concentrations, and fuel/air equivalence ratios, is provided by the two-dimensional LIBS mapping technique that was presented in this work. For a two-phase spray flame analysis, simultaneous laser ignition and laser-induced plasma spectroscopy on a spray flame were conducted in order to develop a feedback control system. The quantitative equivalence ratios and liquid fuel volume fractions were obtained from the laser irradiation, which also caused ignition in the spray. The present results suggest the use of a fuel/air ratio feedback controller that uses a single laser source for both optical breakdown for spectroscopy and subsequent ignition of the two-phase spray.

For a two-phase aerosol analysis, we conducted carbon particulate detection via LIBS in a high-speed free stream that resembled aircraft exhaust flow. The particles and plasma were visualized by an optical system while the LIBS system was used to measure the signal intensity. The calibration curves between the carbon concentration and the LIBS signals were obtained for both high- and low-velocity conditions. The LOD of the LIBS signal was obtained for the solid-phase particulates. The present attempt at organic PM detection in a high-speed stream is a new attempt with much potential for future research, and as such, we confirmed that LIBS can be used to diagnose thermo-fluid phenomena in various phase conditions. In addition, we demonstrated that rGO-coated aluminum thin film and rGO-coated PDMS are excellent optoacoustic transmitters for generating strong, high-frequency ultrasound waves. The optoacoustic transmitter based on rGO-Al and rGO-PDMS films on a glass substrate generated pressure signals that were 64 and 76 times the Al alone, respectively. The promising laser-induced ultrasound wave generation suggested by the present study provides a viable alternative to conventional electrical ultrasound transducers for medical imaging. This work suggests that LIBS and LIUS have clear potential as practical diagnostic tools in thermo-fluid applications.

REFERENCES

- [1] A. C. Eckbreth, *Laser diagnostics for combustion temperature and species* vol. 3: CRC Press, 1996.
- [2] D. Bäuerle, *Laser processing and chemistry* vol. 3: Springer Berlin, 2000.
- [3] L. J. Radziemski and D. A. Cremers, "Laser-induced plasmas and applications," 1989.
- [4] F. Ferioli, P. V. Puzinauskas, and S. G. Buckley, "Laser-induced breakdown spectroscopy for on-line engine equivalence ratio measurements," *Applied spectroscopy*, vol. 57, pp. 1183-1189, 2003.
- [5] F. Ferioli and S. Buckley, "Measurements of hydrocarbons using laser-induced breakdown spectroscopy," *Combustion and Flame*, vol. 144, pp. 435-447, 2006.
- [6] H. Do and C. Carter, "Hydrocarbon fuel concentration measurement in reacting flows using short-gated emission spectra of laser induced plasma," *Combustion and Flame*, vol. 160, pp. 601-609, 2013.
- [7] N. Glumac and G. Elliott, "The effect of ambient pressure on laser-induced plasmas in air," *Optics and lasers in engineering*, vol. 45, pp. 27-35, 2007.
- [8] P. Stavropoulos, A. Michalakou, G. Skevis, and S. Couris, "Laser-induced breakdown spectroscopy as an analytical tool for equivalence ratio measurement in methane-air premixed flames," *Spectrochimica Acta Part B: Atomic Spectroscopy*, vol. 60, pp. 1092-1097, 2005.
- [9] S. R. Turns, *An introduction to combustion* vol. 287: McGraw-Hill New York, 1996.
- [10] H. Zhang, F.-Y. Yueh, and J. P. Singh, "Laser-induced breakdown spectrometry as a multimetal continuous-emission monitor," *Applied Optics*, vol. 38, pp. 1459-1466, 1999.
- [11] S. G. Buckley, H. A. Johnsen, K. R. Hencken, and D. W. Hahn, "Implementation of laser-induced breakdown spectroscopy as a continuous emissions monitor for toxic metals," *Waste Management*, vol. 20, pp. 455-462, 2000.
- [12] P. Dixon and D. Hahn, "Feasibility of detection and identification of individual bioaerosols using laser-induced breakdown spectroscopy," *Analytical chemistry*, vol. 77, pp. 631-638, 2005.
- [13] J. Kiefer, J. W. Tröger, Z. Li, T. Seeger, M. Alden, and A. Leipertz, "Laser-induced breakdown flame thermometry," *Combustion and Flame*, vol. 159, pp. 3576-3582, 2012.

- [14] H. Do, C. D. Carter, Q. Liu, T. M. Ombrello, S. Hammack, T. Lee, *et al.*, "Simultaneous gas density and fuel concentration measurements in a supersonic combustor using laser induced breakdown," *Proceedings of the Combustion Institute*, vol. 35, pp. 215-2162, 2015.
- [15] Y. Zhang, G. Xiong, S. Li, Z. Dong, S. G. Buckley, and S. D. Tse, "Novel low-intensity phase-selective laser-induced breakdown spectroscopy of TiO₂ nanoparticle aerosols during flame synthesis," *Combustion and Flame*, vol. 160, pp. 725-733, 2013.
- [16] Y. Yuan, S. Li, and Q. Yao, "Dynamic behavior of sodium release from pulverized coal combustion by phase-selective laser-induced breakdown spectroscopy," *Proceedings of the Combustion Institute*, vol. 35, pp. 2339-2346, 2015.
- [17] X. Wang, Y. Pang, G. Ku, X. Xie, G. Stoica, and L. V. Wang, "Noninvasive laser-induced photoacoustic tomography for structural and functional in vivo imaging of the brain," *Nature biotechnology*, vol. 21, pp. 803-806, 2003.
- [18] M. W. Sigrist and F. K. Kneubühl, "Laser-generated stress waves in liquids," *The Journal of the Acoustical Society of America*, vol. 64, pp. 1652-1663, 1978.
- [19] T. Buma, M. Spisar, and M. O'donnell, "High-frequency ultrasound array element using thermoelastic expansion in an elastomeric film," *Applied Physics Letters*, vol. 79, pp. 548-550, 2001.
- [20] A. K. Geim and K. S. Novoselov, "The rise of graphene," *Nature materials*, vol. 6, pp. 183-191, 2007.
- [21] G. Wetsel Jr, "Photothermal generation of thermoelastic waves in composite media," *IEEE transactions on ultrasonics, ferroelectrics, and frequency control*, pp. 450-461, 1986.
- [22] F. A. McDonald, "Practical quantitative theory of photoacoustic pulse generation," *Applied Physics Letters*, vol. 54, pp. 1504-1506, 1989.
- [23] S. H. Lee, H. T. Hahn, and J. J. Yoh, "Towards a two-dimensional laser induced breakdown spectroscopy mapping of liquefied petroleum gas and electrolytic oxy-hydrogen flames," *Spectrochimica Acta Part B: Atomic Spectroscopy*, vol. 88, pp. 63-68, 2013.
- [24] F. Ferioli, S. Buckley, and P. Puzinauskas, "Real-time measurement of equivalence ratio using laser-induced breakdown spectroscopy," *International Journal of Engine Research*, vol. 7, pp. 447-457, 2006.
- [25] P. Stavropoulos, A. Michalakou, G. Skevis, and S. Couris, "Quantitative local equivalence ratio determination in laminar premixed methane-air flames by laser induced breakdown spectroscopy

- (LIBS)," *Chemical Physics Letters*, vol. 404, pp. 309-314, 2005.
- [26] K. E. Eseller, F. Y. Yueh, and J. P. Singh, "Laser-induced breakdown spectroscopy measurement in methane and biodiesel flames using an ungated detector," *Applied optics*, vol. 47, pp. G144-G148, 2008.
- [27] M. S. Mansour, H. Imam, K. A. Elsayed, and W. Abbass, "Local equivalence ratio measurements in turbulent partially premixed flames using laser-induced breakdown spectroscopy," *Spectrochimica Acta Part B: Atomic Spectroscopy*, vol. 64, pp. 1079-1084, 2009.
- [28] J. Kiefer, J. Tröger, Z. Li, and M. Aldén, "Laser-induced plasma in methane and dimethyl ether for flame ignition and combustion diagnostics," *Applied Physics B*, vol. 103, pp. 229-236, 2011.
- [29] V. N. Rai, J. P. Singh, C. Winstead, F.-Y. Yueh, and R. L. Cook, "Laser-induced breakdown spectroscopy of hydrocarbon flame and rocket engine simulator plume," *AIAA journal*, vol. 41, pp. 2192-2199, 2003.
- [30] M. Kotzagianni and S. Couris, "Femtosecond laser induced breakdown for combustion diagnostics," *Applied Physics Letters*, vol. 100, p. 264104, 2012.
- [31] M. M. Tripathi, K. K. Srinivasan, S. R. Krishnan, F.-Y. Yueh, and J. P. Singh, "A comparison of multivariate LIBS and chemiluminescence-based local equivalence ratio measurements in premixed atmospheric methane-air flames," *Fuel*, vol. 106, pp. 318-326, 2013.
- [32] A. Michalakou, P. Stavropoulos, and S. Couris, "Laser-induced breakdown spectroscopy in reactive flows of hydrocarbon-air mixtures," *Applied Physics Letters*, vol. 92, p. 081501, 2008.
- [33] R. Schefer, W. Houf, B. Bourne, and J. Colton, "Spatial and radiative properties of an open-flame hydrogen plume," *International Journal of Hydrogen Energy*, vol. 31, pp. 1332-1340, 2006.
- [34] R. W. Schefer, W. D. Kulatilaka, B. D. Patterson, and T. B. Settersten, "Visible emission of hydrogen flames," *Combustion and Flame*, vol. 156, pp. 1234-1241, 2009.
- [35] A. R. Choudhuri and S. R. Gollahalli, "Laser induced fluorescence measurements of radical concentrations in hydrogen-hydrocarbon hybrid gas fuel flames," *International journal of hydrogen energy*, vol. 25, pp. 1119-1127, 2000.
- [36] A. R. Choudhuri and S. Gollahalli, "Combustion characteristics of hydrogen-hydrocarbon hybrid fuels," *International journal of hydrogen energy*, vol. 25, pp. 451-462, 2000.
- [37] S. Yadav Milind, S. Sawant, A. Anavkar Jayesh, and V. Chavan Hemant, "Investigations on generation methods for oxy-hydroge

- n gas, its blending with conventional fuels and effect on the performance of internal combustion engine."
- [38] K. E. Eseller, F.-Y. Yueh, and J. P. Singh, "Non-intrusive, on-line, simultaneous multi-species impurity monitoring in hydrogen using LIBS," *Applied Physics B*, vol. 102, pp. 963-969, 2011.
 - [39] T.-W. Lee and N. Hegde, "Laser-induced breakdown spectroscopy for in situ diagnostics of combustion parameters including temperature," *Combustion and Flame*, vol. 142, pp. 314-316, 2005.
 - [40] C. Letty, A. Pastore, E. Mastorakos, R. Balachandran, and S. Couris, "Comparison of electrical and laser spark emission spectroscopy for fuel concentration measurements," *Experimental Thermal and Fluid Science*, vol. 34, pp. 338-345, 2010.
 - [41] C. G. Morgan, "Laser-induced breakdown of gases," *Reports on Progress in Physics*, vol. 38, p. 621, 1975.
 - [42] T. Spiglanin, A. McIlroy, E. Fournier, R. Cohen, and J. Syage, "Time-resolved imaging of flame kernels: laser spark ignition of H₂/O₂/Ar mixtures," *Combustion and Flame*, vol. 102, pp. 310-328, 1995.
 - [43] T. X. Phuoc and F. P. White, "Laser-induced spark ignition of CH₄/air mixtures," *Combustion and flame*, vol. 119, pp. 203-216, 1999.
 - [44] Ş. Yalçın, D. Crosley, G. Smith, and G. W. Faris, "Influence of ambient conditions on the laser air spark," *Applied Physics B: Lasers and Optics*, vol. 68, pp. 121-130, 1999.
 - [45] D. Bradley, C. G. W. Sheppard, I. M. Suardjaja, and R. Woolley, "Fundamentals of high-energy spark ignition with lasers," *Combustion and Flame*, vol. 138, pp. 55-77, 2004.
 - [46] J. L. Beduneau, N. Kawahara, T. Nakayama, E. Tomita, and Y. Ikeda, "Laser-induced radical generation and evolution to a self-sustaining flame," *Combustion and Flame*, vol. 156, pp. 642-656, 2009.
 - [47] T. X. Phuoc, "Laser-induced spark ignition fundamental and applications," *Optics and Lasers in Engineering*, vol. 44, pp. 351-397, 2006.
 - [48] M. Lawes, Y. Lee, A. Mokhtar, and R. Woolley, "Laser ignition of iso-octane air aerosols," *Combustion Science and Technology*, vol. 180, pp. 296-313, 2007.
 - [49] V. Groß, H. Kubach, U. Spicher, R. Schießl, and U. Maas, "Influence of Laser-Induced Ignition on Spray-Guided Combustion-Experimental Results and Numerical Simulation of Ignition Processes," SAE Technical Paper2009.
 - [50] K. G. Moesl, K. G. Vollmer, T. Sattelmayer, J. Eckstein, and H. Kopecek, "Experimental study on laser-induced ignition of swirl

- stabilized kerosene flames," *Journal of Engineering for Gas Turbines and Power*, vol. 131, p. 021501, 2009.
- [51] G. C. Gebel, T. Mosbach, W. Meier, and M. Aigner, "Optical and spectroscopic diagnostics of laser-induced air breakdown and kerosene spray ignition," *Combustion and Flame*, 2014.
- [52] C. Schulz and V. Sick, "Tracer-LIF diagnostics: quantitative measurement of fuel concentration, temperature and fuel/air ratio in practical combustion systems," *Progress in Energy and Combustion Science*, vol. 31, pp. 75-121, 2005.
- [53] L. Zimmer and S. Tachibana, "Laser induced plasma spectroscopy for local equivalence ratio measurements in an oscillating combustion environment," *Proceedings of the Combustion Institute*, vol. 31, pp. 737-745, 2007.
- [54] M. K. Roy, N. Kawahara, E. Tomita, and T. Fujitani, "Jet-guided combustion characteristics and local fuel concentration measurements in a hydrogen direct-injection spark-ignition engine," *Proceedings of the Combustion Institute*, vol. 34, pp. 2977-2984, 2013.
- [55] T. X. Phuoc, "Laser-induced spark for simultaneous ignition and fuel-to-air ratio measurements," *Optics and Lasers in Engineering*, vol. 44, pp. 520-534, 2006.
- [56] N. Kawahara, K. Tsuboi, and E. Tomita, "Laser-induced plasma generation and evolution in a transient spray," *Optics express*, vol. 22, pp. A44-A52, 2014.
- [57] Y.-L. Chen, J. Lewis, and C. Parigger, "Spatial and temporal profiles of pulsed laser-induced air plasma emissions," *Journal of Quantitative Spectroscopy and Radiative Transfer*, vol. 67, pp. 91-103, 2000.
- [58] M. Dong, X. Mao, J. J. Gonzalez, J. Lu, and R. E. Russo, "Time-resolved LIBS of atomic and molecular carbon from coal in air, argon and helium," *Journal of Analytical Atomic Spectrometry*, vol. 27, pp. 2066-2075, 2012.
- [59] P. Lucena, A. Dona, L. Tobarria, and J. Laserna, "New challenges and insights in the detection and spectral identification of organic explosives by laser induced breakdown spectroscopy," *Spectrochimica Acta Part B: Atomic Spectroscopy*, vol. 66, pp. 12-20, 2011.
- [60] P.-E. Bengtsson and M. Aldén, "Optical investigation of laser-produced C₂ in premixed sooty ethylene flames," *Combustion and Flame*, vol. 80, pp. 322-328, 1990.
- [61] S. H. Lee and J. J. Yoh, "Detection of Carbon Particulates from a High-Speed Stream Reaching 70 Meters/Second," *Applied Spectroscopy*, vol. 66, pp. 107-113, 2012.

- [62] S. H. Lee and J. J. Yoh, "Spectroscopic detection of carbon particulates from a high speed jet stream with extended plasma visualization," *Spectrochimica Acta Part B: Atomic Spectroscopy*, vol. 74-75, pp. 144-150, 2012.
- [63] D. S. Lee, D. W. Fahey, P. M. Forster, P. J. Newton, R. C. Wit, L. L. Lim, *et al.*, "Aviation and global climate change in the 21st century," *Atmospheric Environment*, vol. 43, pp. 3520-3537, 2009.
- [64] J. W. Childers, C. L. Witherspoon, L. B. Smith, and J. D. Pleil, "Real-time and integrated measurement of potential human exposure to particle-bound polycyclic aromatic hydrocarbons (PAHs) from aircraft exhaust," *Environmental Health Perspectives*, vol. 108, p. 853, 2000.
- [65] D. Westerdahl, S. A. Fruin, P. L. Fine, and C. Sioutas, "The Los Angeles International Airport as a source of ultrafine particles and other pollutants to nearby communities," *Atmospheric Environment*, vol. 42, pp. 3143-3155, 2008.
- [66] M.-D. Cheng and E. Corporan, "A study of extractive and remote-sensing sampling and measurement of emissions from military aircraft engines," *Atmospheric Environment*, vol. 44, pp. 4867-4878, 2010.
- [67] J. Delhay, P. Desgroux, E. Therssen, H. Bladh, P.-E. Bengtsson, H. Hönen, *et al.*, "Soot volume fraction measurements in aero-engine exhausts using extinction-calibrated backward laser-induced incandescence," *Applied Physics B*, vol. 95, pp. 825-838, 2009.
- [68] J. D. Black and M. P. Johnson, "In-situ laser-induced incandescence of soot in an aero-engine exhaust: Comparison with certification style measurements," *Aerospace Science and Technology*, vol. 14, pp. 329-337, 2010.
- [69] K. Song, Y.-I. Lee, and J. Sneddon, "Recent developments in instrumentation for laser induced breakdown spectroscopy," *Applied Spectroscopy Reviews*, vol. 37, pp. 89-117, 2002.
- [70] J. L. Gottfried, F. C. De Lucia Jr, C. A. Munson, and A. W. Miziolek, "Laser-induced breakdown spectroscopy for detection of explosives residues: a review of recent advances, challenges, and future prospects," *Analytical and bioanalytical chemistry*, vol. 395, pp. 283-300, 2009.
- [71] J. D. Winefordner, I. B. Gornushkin, T. Correll, E. Gibb, B. W. Smith, and N. Omenetto, "Comparing several atomic spectrometric methods to the super stars: special emphasis on laser induced breakdown spectrometry, LIBS, a future super star," *Journal of analytical atomic spectrometry*, vol. 19, pp. 1061-1083, 2004.
- [72] M. Z. Martin, M.-D. Cheng, and R. C. Martin, "Aerosol Measur

- ement by Laser-Induced Plasma Technique: A Review," *Aerosol Science and Technology*, vol. 31, pp. 409-421, 1999.
- [73] J. D. Hybl, G. A. Lithgow, and S. G. Buckley, "Laser-induced breakdown spectroscopy detection and classification of biological aerosols," *Applied spectroscopy*, vol. 57, pp. 1207-1215, 2003.
- [74] D. Hahn, W. Flower, and K. Hencken, "Discrete particle detection and metal emissions monitoring using laser-induced breakdown spectroscopy," *Applied spectroscopy*, vol. 51, pp. 1836-1844, 1997.
- [75] D. Hahn, "Laser-induced breakdown spectroscopy for sizing and elemental analysis of discrete aerosol particles," *Applied physics letters*, vol. 72, pp. 2960-2962, 1998.
- [76] D. W. Hahn and M. M. Lunden, "Detection and Analysis of Aerosol Particles by Laser-Induced Breakdown Spectroscopy," *Aerosol Science and Technology*, vol. 33, pp. 30-48, 2000.
- [77] B. T. Fisher, H. A. Johnsen, S. G. Buckley, and D. W. Hahn, "Temporal gating for the optimization of laser-induced breakdown spectroscopy detection and analysis of toxic metals," *Applied Spectroscopy*, vol. 55, pp. 1312-1319, 2001.
- [78] K. Park, G. Cho, and J.-h. Kwak, "Development of an Aerosol Focusing-Laser Induced Breakdown Spectroscopy (Aerosol Focusing-LIBS) for Determination of Fine and Ultrafine Metal Aerosols," *Aerosol Science and Technology*, vol. 43, pp. 375-386, 2009.
- [79] E. Vors and L. Salmon, "Laser-induced breakdown spectroscopy (LIBS) for carbon single shot analysis of micrometer-sized particles," *Analytical and bioanalytical chemistry*, vol. 385, pp. 281-286, 2006.
- [80] P. V. Puzinauskas, S. G. Buckley, and F. Ferioli, "Real-time measurement of equivalence ratio using laser-induced breakdown spectroscopy," *International Journal of Engine Research*, vol. 7, pp. 447-457, 2006.
- [81] M. E. Asgill, M. S. Brown, K. Frische, W. M. Roquemore, and D. W. Hahn, "Double-pulse and single-pulse laser-induced breakdown spectroscopy for distinguishing between gaseous and particulate phase analytes," *Applied optics*, vol. 49, pp. C110-C119, 2010.
- [82] G. Lockwood, D. Turnbull, D. Christopher, and F. Foster, "Beyond 30 MHz [applications of high-frequency ultrasound imaging]," *Engineering in Medicine and Biology Magazine, IEEE*, vol. 15, pp. 60-71, 1996.
- [83] P. Wells, "Ultrasound imaging," *Physics in medicine and biology*, vol. 51, p. R83, 2006.
- [84] R. Von Gutfeld and H. Budd, "Laser-generated MHz elastic wave

- es from metallic-liquid interfaces," *Applied Physics Letters*, vol. 34, pp. 617-619, 1979.
- [85] Y. Hou, J.-S. Kim, S. Ashkenazi, M. O'Donnell, and L. J. Guo, "Optical generation of high frequency ultrasound using two-dimensional gold nanostructure," *Applied physics letters*, vol. 89, p. 093901, 2006.
- [86] Y. Hou, J.-S. Kim, S. Ashkenazi, S.-W. Huang, L. J. Guo, and M. O'Donnell, "Broadband all-optical ultrasound transducers," *Applied Physics Letters*, vol. 91, p. 073507, 2007.
- [87] H. W. Baac, J. G. Ok, H. J. Park, T. Ling, S.-L. Chen, A. J. Hart, *et al.*, "Carbon nanotube composite optoacoustic transmitters for strong and high frequency ultrasound generation," *Applied physics letters*, vol. 97, p. 234104, 2010.
- [88] Y. Guo, H. W. Baac, S.-L. Chen, T. B. Norris, and L. J. Guo, "Broad-band high-efficiency optoacoustic generation using a novel photonic crystal-metallic structure," in *SPIE BiOS*, 2011, pp. 78992C-78992C-8.
- [89] D. R. Dreyer, S. Park, C. W. Bielawski, and R. S. Ruoff, "The chemistry of graphene oxide," *Chemical Society Reviews*, vol. 39, pp. 228-240, 2010.
- [90] D. WookáLee, J. YoungáKim, and H. SukáShin, "Highly controllable transparent and conducting thin films using layer-by-layer assembly of oppositely charged reduced graphene oxides," *Journal of Materials Chemistry*, vol. 21, pp. 3438-3442, 2011.
- [91] I. Jung, M. Vaupel, M. Pelton, R. Piner, D. A. Dikin, S. Stankovich, *et al.*, "Characterization of thermally reduced graphene oxide by imaging ellipsometry," *The Journal of Physical Chemistry C*, vol. 112, pp. 8499-8506, 2008.
- [92] A. A. Balandin, S. Ghosh, W. Bao, I. Calizo, D. Teweldebrhan, F. Miao, *et al.*, "Superior thermal conductivity of single-layer graphene," *Nano letters*, vol. 8, pp. 902-907, 2008.
- [93] D. Yoon, Y.-W. Son, and H. Cheong, "Negative thermal expansion coefficient of graphene measured by Raman spectroscopy," *Nano letters*, vol. 11, pp. 3227-3231, 2011.
- [94] N. Mounet and N. Marzari, "First-principles determination of the structural, vibrational and thermodynamic properties of diamond, graphite, and derivatives," *Physical Review B*, vol. 71, p. 205214, 2005.
- [95] H. Jiang, B. Liu, Y. Huang, and K. Hwang, "Thermal expansion of single wall carbon nanotubes," *Journal of engineering materials and technology*, vol. 126, pp. 265-270, 2004.
- [96] S. H. Lee, Y. Lee, and J. J. Yoh, "Reduced graphene oxide coated polydimethylsiloxane film as an optoacoustic transmitter for

- high pressure and high frequency ultrasound generation," *Applied Physics Letters*, vol. 106, p. 081911, 2015.
- [97] X. Li, W. Wu, Y. Chung, W. Y. Shih, W.-H. Shih, Q. Zhou, *et al.*, "80-MHz intravascular ultrasound transducer using PMN-PT free-standing film," *Ultrasonics, Ferroelectrics and Frequency Control, IEEE Transactions on*, vol. 58, pp. 2281-2288, 2011.
- [98] R. J. Colchester, C. A. Mosse, D. S. Bhachu, J. C. Bear, C. J. Carmalt, I. P. Parkin, *et al.*, "Laser-generated ultrasound with optical fibres using functionalised carbon nanotube composite coatings," *Applied Physics Letters*, vol. 104, p. 173502, 2014.
- [99] S. H. Lee, M.-a. Park, J. J. Yoh, H. Song, E. Y. Jang, Y. H. Kim, *et al.*, "Reduced graphene oxide coated thin aluminum film as an optoacoustic transmitter for high pressure and high frequency ultrasound generation," *Applied Physics Letters*, vol. 101, p. 241909, 2012.
- [100] O. Wright, "Laser picosecond acoustics in double-layer transparent films," *Optics letters*, vol. 20, pp. 632-634, 1995.
- [101] D. Hurley, O. Wright, O. Matsuda, V. Gusev, and O. Kolosov, "Laser picosecond acoustics in isotropic and anisotropic materials," *Ultrasonics*, vol. 38, pp. 470-474, 2000.
- [102] Y. Xu, Z. Li, and W. Duan, "Thermal and thermoelectric properties of graphene," *Small*, vol. 10, pp. 2182-2199, 2014.
- [103] S. Davies, C. Edwards, G. Taylor, and S. B. Palmer, "Laser-generated ultrasound: its properties, mechanisms and multifarious applications," *Journal of Physics D: Applied Physics*, vol. 26, p. 329, 1993.

초 록

본 연구에서는 레이저 유도 플라즈마 분광분석법 (LIBS : Laser-Induced Breakdown Spectroscopy) 을 활용하여 기체뿐만 아니라 액체-기체, 고체-기체 등의 이상상태에서의 열 유체 현상을 측정하는 연구가 수행되었다. 우선 기체상태의 측정을 위해서 프로판(*propane*) 연료를 사용하여서 확산 화염을 만들고 미연소 및 연소 상태에서의 레이저 유도 플라즈마의 특성을 분석하였다. 그리고 LIBS 를 활용하여 화염의 2차원적인 당량비, 밀도, 연료량을 측정하였다. 액체-기체 이상 상태의 분석을 위하여 가솔린(*gasoline*) 연료로 분무화염을 만들었다. 레이저 유도 플라즈마의 높은 온도를 통하여 분무화염을 점화시키고 동시에 LIBS 를 활용하여 점화특성에 영향을 미치는 당량비와 액적의 특성을 측정하였다. 그래서 레이저 유도 플라즈마를 활용하여 점화 및 진단을 동시에 할 수 있는 피드백(*feed-back*) 시스템을 개발하였다. 기체-고체 이상상태를 분석하기 위하여 초음파 분무기와 제습장치를 이용하여서 미세입자를 발생시키고 유동시스템에 주입시켰다. LIBS 를 활용하여 미세입자의 농도를 측정하였고 비행기의 배출가스의 속도와 유사한 70 m/s 빠른 속도의 유동에서도 LIBS로 미세입자를 측정 할 수 있음을 확인하였다.

또한 열유체 진단의 기초연구로서 레이저 유도 초음파 (LIUS : Laser-Induced UltraSound) 를 활용하여 더 높은 압력과 주파수를 갖는 초음파를 발생시키는 연구가 수행되었다. 더 높은 압력 및 넓은 주파수 대역폭을 갖는 초음파를 발생시키기 위해서 높은 열전도도를 갖는 그래핀(*graphene*)과 높은 열팽창계수를 갖는 알루미늄(*Aluminium*), PDMS(*polydimethylsiloxane*) 박막들이 사용되었다. 그래서

환원된 그래핀 산화물(rGO : reduced Graphene Oxide)과 알루미늄 복합 재료를 사용하여 기존의 금속박막보다 64배 더 큰 압력의 초음파를 발생시켰고 rGO와 PDMS 복합재료를 사용하여 금속박막보다 76배 더 높은 압력의 초음파를 발생시켰다. 이러한 높은 압력과 넓은 대역폭의 초음파는 더 높은 정밀도의 열유체 측정에 사용될 수 있을 것이다.

본 연구를 통하여 이상상태를 포함한 다양한 상태에서의 열유체 현상들을 LIBS 를 활용하여 손쉽고 정밀하게 측정할 수 있음을 확인하였다. 또한 높은 압력과 넓은 대역폭을 갖는 LIUS 를 발생시켜 초음파를 이용한 열유체 진단의 기초연구가 수행되었다. 이러한 연구 결과를 바탕으로 바이오 및 의료분야, 연소 및 추진체 분야, 오염물질 탐지 분야등의 다양한 분야에서 더욱 효율적이고 정밀한 열유체 진단이 가능하게 될 것이다

주요어: 레이저 유도 플라즈마 분광분석법, 플라즈마, 레이저 유도 초음파 분석법, 열유체, 연소, 그래핀

학 번: 2010-30195